論文 / 著書情報
Article / Book Information

題目(和文)	
Title(English)	A study of improvement on the charge/discharge rate of lithium ion battery focusing on electron conduction of tungsten trioxide electrodes
著者(和文)	李 蔚
Author(English)	Wei Li
出典(和文)	学位:博士（工学）, 学位授与機関:東京工業大学, 報告番号:甲第9856号, 授与年月日:2015年3月26日, 学位の種別:課程博士, 審査員:岩井　洋,片岡　好則,名取　研二,筒井　一生,若林　整,角嶋　邦之,Tang Zhenan,Hei Wong
Citation(English)	Degree:, Conferring organization: Tokyo Institute of Technology, Report number:甲第9856号, Conferred date:2015/3/26, Degree Type:Course doctor, Examiner:,,,,,,,
学位種別(和文)	博士論文
Type(English)	Doctoral Thesis

Abstract

Rechargeable lithium ion batteries (LIBs) have been considered to be the most advanced means of energy storage in the near future. The charge/discharge time is becoming increasingly important in evaluating the performance of batteries for their use in electric vehicles and other applications. Although a large amount of research on Li ion transportation has been carried out with the aim of improving the properties of lithium ion batteries, there has been little detailed research on electron conduction to our knowledge. However, electrons and lithium ions both play important roles in determining the charge/discharge speed.

Hence, we have been focusing on improving the charge/discharge performance of lithium ion batteries by increasing the electron conductivity of the electrodes. In this work, tungsten trioxide (WO_3) powder thin films fabricated from nanoparticles was chosen for the electrodes owing to its high reversibility. Moreover, it has been reported that small ions can intercalate into crystalline WO_3 with high reversibility. Besides, the porosity of a WO_3 thin film promotes lithium ion intercalation, resulting in LIBs with high power density.

Resistivity measurements of WO_3 thin film were carried out after annealing in N_2 or 5% O_2+95% N_2 ambient. Annealing in N_2 ambient decreased the resistivity owing to the increased number of oxygen vacancies in the WO_3 thin film. Compared with low-temperature annealing in N_2, high-temperature (from 600 ^oC to 750 ^oC) annealing in N_2 had a greater effect on decreasing the resistivity of *m*-WO_3 thin films. The obtained resistivities were well fitted by assuming two types of electron conduction mechanism: band conduction and nearest-neighbor hopping (NNH) conduction. It is proposed for the

first time that two conduction mechanisms simultaneously exist in the electron conduction of *m*-WO_3 thin films and after high-temperature annealing in N_2, the NNH conduction mechanism becomes dominant owing to the increased number of oxygen vacancies.

Since the electron conductivity can be improved by annealing in N_2 owing to the generation of oxygen vacancies in crystalline WO_3, the performance of LIBs with N_2-annealed WO_3 electrodes was investigated by consideration of the charge-discharge properties, cyclic voltammetry curves, frequency response, and the charge capacity at different charge rates. It was observed that the charge/discharge speed and reversibility were improved as the N_2 annealing temperature increased. Furthermore, the XRD patterns and Raman spectra revealed that annealing at 300 ^oC in N_2 ambient did not change the monoclinic crystalline structure, whereas annealing at 700 ^oC in N_2 ambient changed the monoclinic structure into a cubiclike structure. These results clearly demonstrated that increasing the electron conductivity of WO_3 electrodes can markedly improve the charge/discharge speed and reversibility. Moreover, oxygen vacancies may cause the crystalline structure to change into the cubiclike structure, which may promote Li ion intercalation. Therefore, to enhance the charge/discharge performance of LIBs, electron conduction should be a focus of research. Additionally, crystalline WO_3 was demonstrated to be a promising material for electrodes since oxygen vacancy generation can be induced by a simple annealing treatment, improving the electron conduction and Li ion transportation.

Contents

Chapter 1 Introduction

1.1 Worldwide Energy Requirements

1.2 Need for Energy Storage Equipment

1.3 Introduction to Batteries

1.3.1 Types of Batteries and Their Characteristics

1.3.2 Principle of Secondary Batteries

1.3.3 Performances of Secondary Batteries

1.3.4 Importance of High-Speed Charge/Discharge

1.3.5 Relationship between Internal Resistance and Charge/Discharge Speed

1.4 Purpose of This Work

Reference List

1.1 Worldwide Energy Requirements

As the world is developing increasingly rapidly, the demand for energy is increasing greatly. Energy is a fundamental requirement in our lives; we need energy for transportation, industry, electronic products, and so forth. In particular, as many new electronic products are continuously being created and developed, high energy demand in the near future has been forecast [1].

The world's energy consumption has been predicted to increase from 524 quadrillion Btu (British thermal units) in 2010 to 630 quadrillion Btu in 2020 and 820 quadrillion Btu in 2040, a 30-year increase of 56 percent, as shown in Fig. 1.1 [2]. (1 quadrillion Btu=2.931 $*$ 10^{11} KWh)

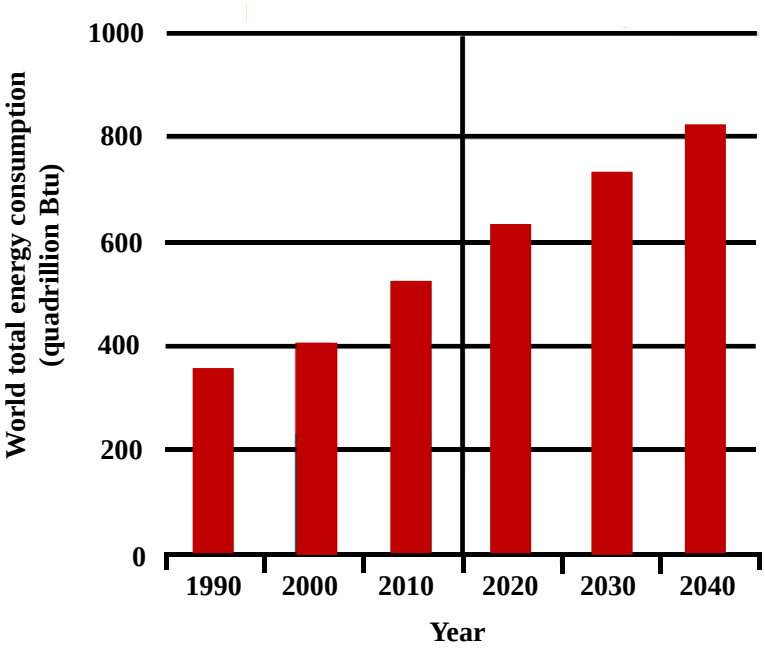

Fig. 1.1. World total energy consumption, 1990–2040 (quadrillion Btu)

1.2 Need for Energy Storage Equipment

As energy consumption is increasing, energy storage equipment is also needed urgently. One of the reasons for the increased need for energy storage equipment is that the worldwide use of electronic products is increasing. For example, the global numbers of smartphone users surpassed 1 billion in 2012 and reached 1.75 billion in 2014 [3]. It is expected that mobile phone adoption will continue rapidly up to 2017, as shown in Fig. 1.2 [4]. Another example is the realization of electronic vehicles. Electronic vehicles that completely depend on electric power are becoming increasingly popular owing to their zero emissions and are expected to develop rapidly in the near future. Table 1.1 shows the targets set by the Japanese government for the use of next–generation vehicles. A key requirement of electronic vehicles is electric power storage equipment.

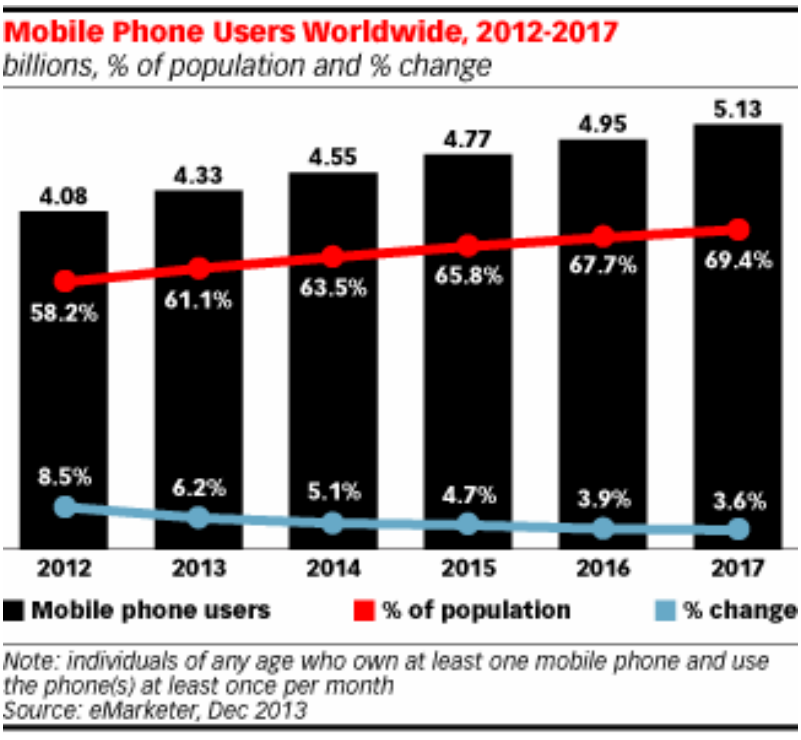

Fig. 1.2. Mobile phone users worldwide, 2012–2017.

Table 1.1. Targets set by Japanese government for next–generation vehicles.

		2020 year	2030 year
Conventional Vehicle		50-80%	30-50%
Next Generation Vehicle		20-50%	50-70%
	Hybrid Vehicle	20-30%	30-40%
	Electric Vehicle	15-20%	20-30%
	Fuel Cell Vehicle	-1%	-3%
	Clean Diesel	-5%	5-10%

Another reason why energy storage equipment is urgently needed is the imbalance between energy consumption and energy resources in the world as shown in Fig. 1.3 [5] and Fig. 1.4 [6]. It is clearly shown that although the Middle East has the largest amount of petroleum, the largest amounts of petroleum are consumed in Asia and North America.

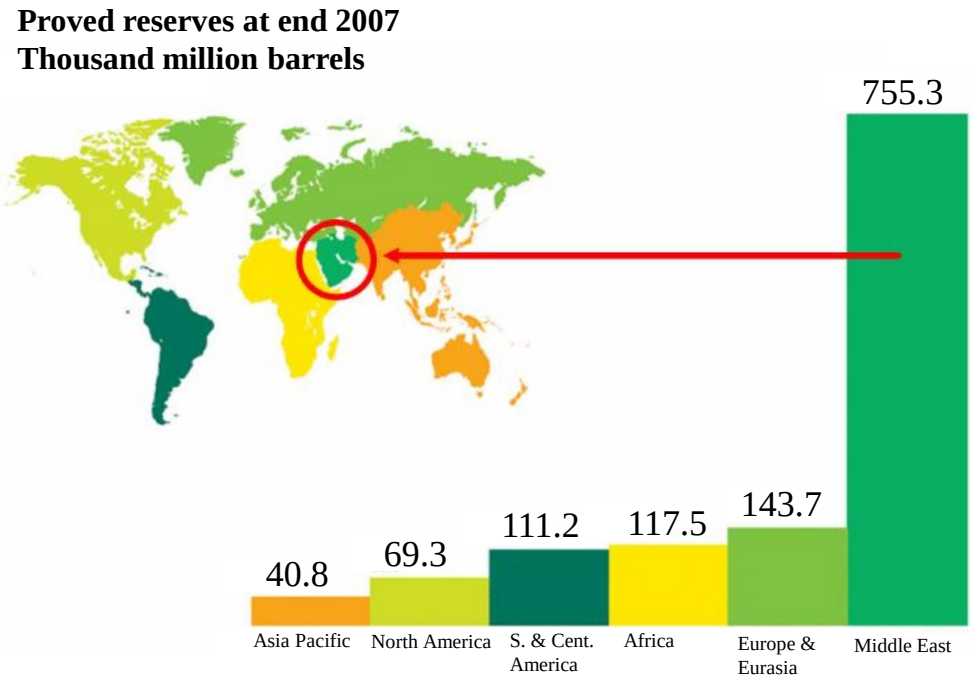

Fig. 1.3. Proven reserves at end of 2007.

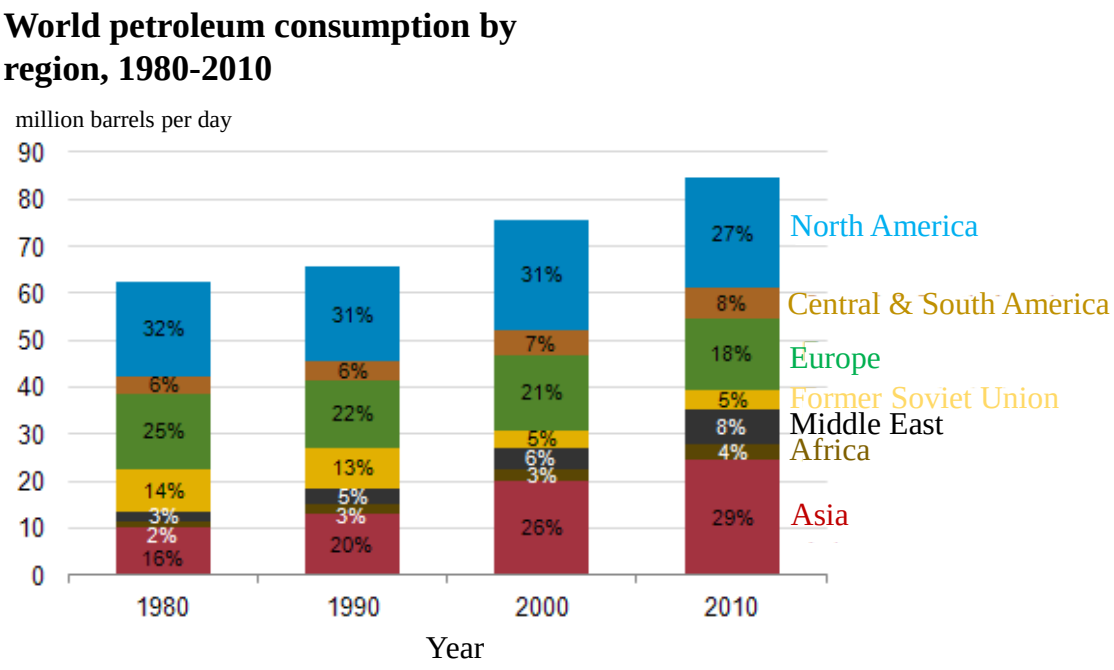

Fig. 1.4. World petroleum consumption by region, 1980–2010.

1.3 Introduction to Batteries

In a highly information-oriented society with a huge energy demand, batteries are playing increasingly important roles in various aspects and are a part of our everyday lives. Batteries are used in portable phones, remote controls, flashlights, and to help cars start easily. Their portability makes batteries so important. The convenience brought about by batteries has led to the invention of more appliances and equipment that make use of them, which has also made the world more convenient and develop at a faster pace.

There are now automobiles running on electrical energy stored in batteries. These electric vehicles obtain all their power from batteries and do not use gasoline. It has been predicted that in the near future, the production of lithium ion batteries (LIBs) will be greatly increased owing to the development of hybrid vehicles and electric vehicles, as shown in Figs. 1.5 (a) [7] and (b), which are from a report of an information technology research laboratory.

(a)

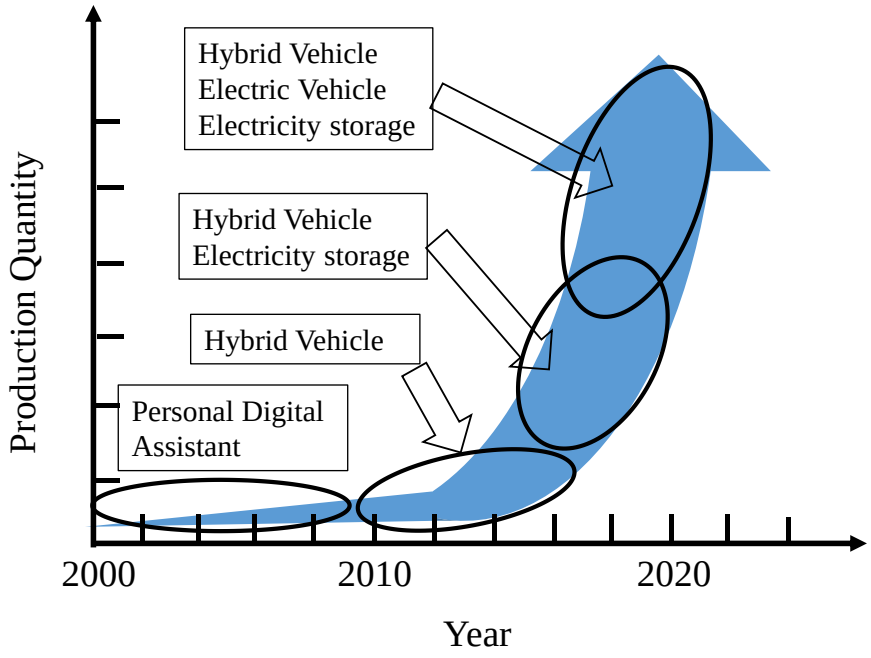

(b)

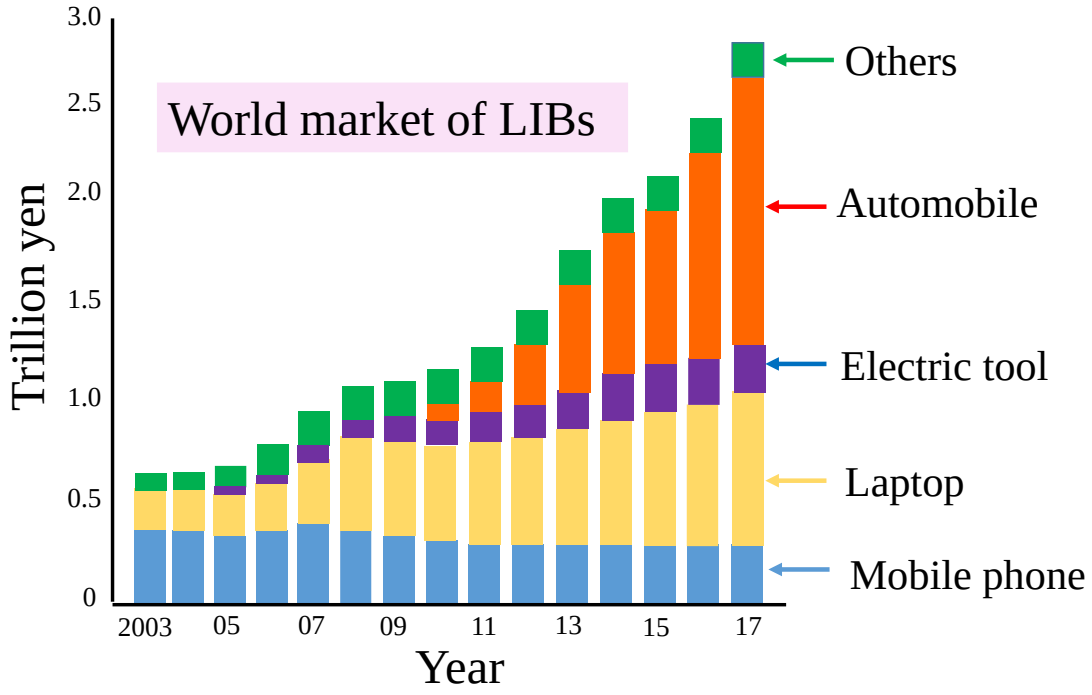

Fig. 1.5. (a) Predicted production of LIBs and (b) predicted world market for LIBs.

1.3.1 Types of batteries and their characteristics

Batteries are devices that convert the energy of a chemical reaction into electric energy. On the basis of their different working principles, batteries can be classified into three main types, single-discharge batteries, secondary batteries, and fuel cells. Here, these three types of batteries are introduced.

(1) Single-discharge batteries

Single-discharge batteries include a finite quantity of reactants for the reaction. When the reactants have been used, a single-discharge battery cannot be used again. The most typical type of single-discharge is the Daniell cell, which is an electrochemical cell invented in 1836 by John Frederic Daniell [7]. In a Daniell cell, copper and zinc electrodes are immersed in solutions of copper(II) sulfate and zinc sulfate, respectively, as shown in

Fig. 1.6. At the anode, zinc is oxidized: $Zn \rightarrow Zn^{2+} + 2e^-$. At the cathode, copper is reduced: $Cu^{2+} + 2e^- \rightarrow Cu$. The total reaction is $Zn + Cu^{2+} \rightarrow Zn^{2+} + Cu$.

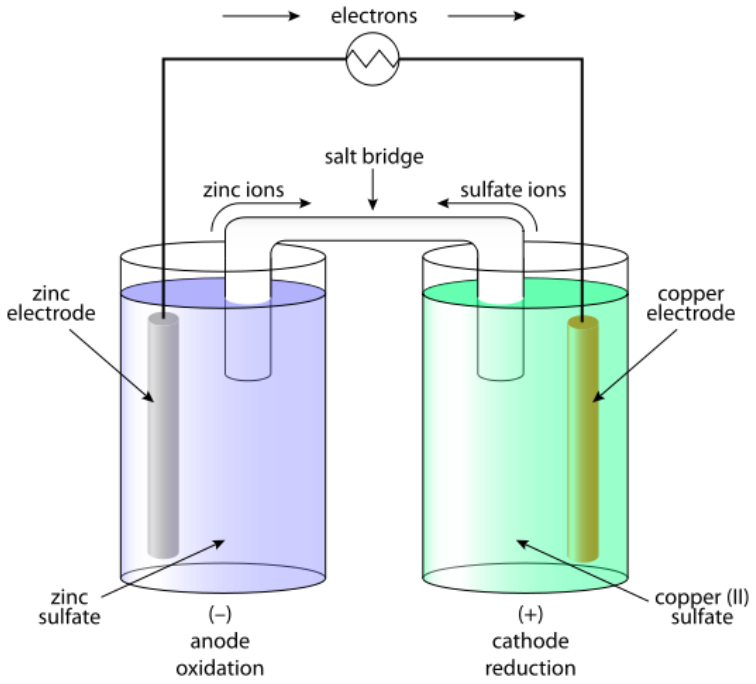

Fig. 1.6. Two half-cell form of the Daniell cell [8].

(2) Secondary batteries

Secondary batteries can be recharged by applying an electric current when the discharge is completed. Applying an electric current in the opposite direction can regenerate the original reactants from the reaction products; thus, electric energy can be stored in a secondary battery in the form of chemical energy. There are many applications of secondary batteries, as shown in Fig. 1.7, such as electric vehicles, space exploration, deep sea exploration, medical equipment, wearable products, and so forth. The principle of secondary batteries will be given in detail later.

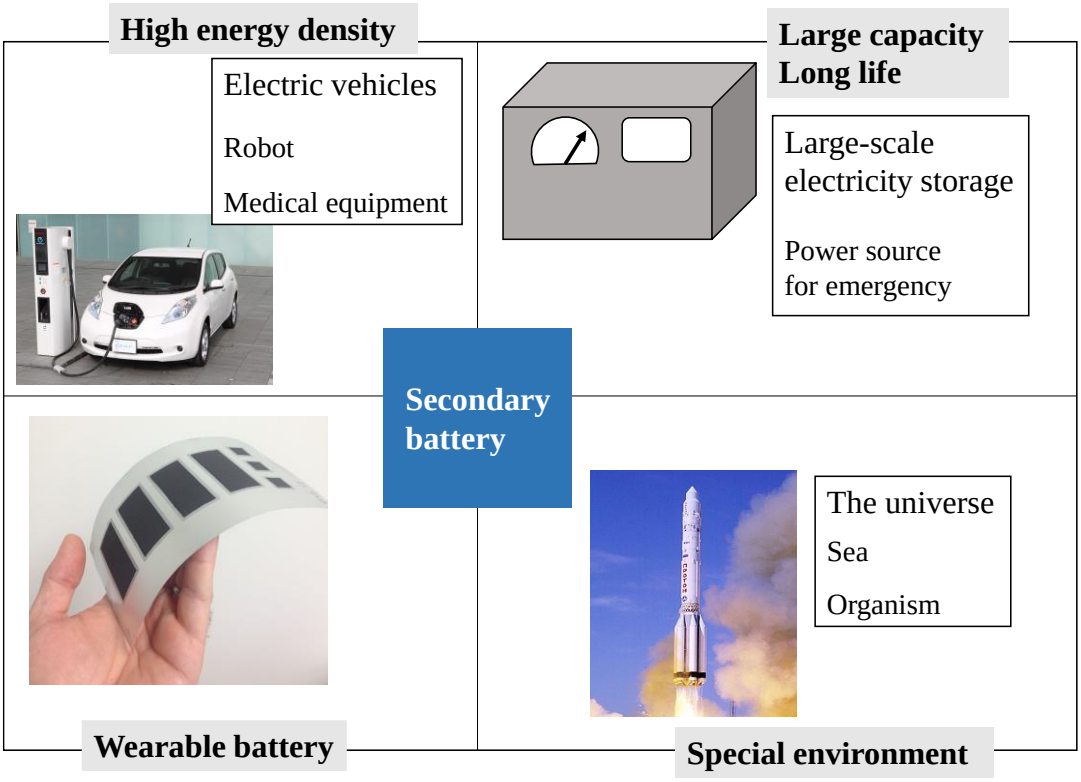

Fig. 1.7. Current and future applications of secondary batteries [7].

(3) Fuel cells

In a fuel cell, reactants are added to the cell continuously and reaction products are removed continuously. Hence, fuel cells can generate electric energy continuously as long as the supply of external reactants is maintained. In addition to electricity, fuel cells produce water, heat, and, depending on the fuel source, very small amounts of nitrogen dioxide and other emissions [9].

Although there are many types of fuel cells, they all consist of an anode, a cathode, and an electrolyte that allows charges to move between the two sides of the fuel cell as shown in Fig. 1.8. Electrons are drawn from the anode to the cathode through an external circuit, producing direct current electricity [9].

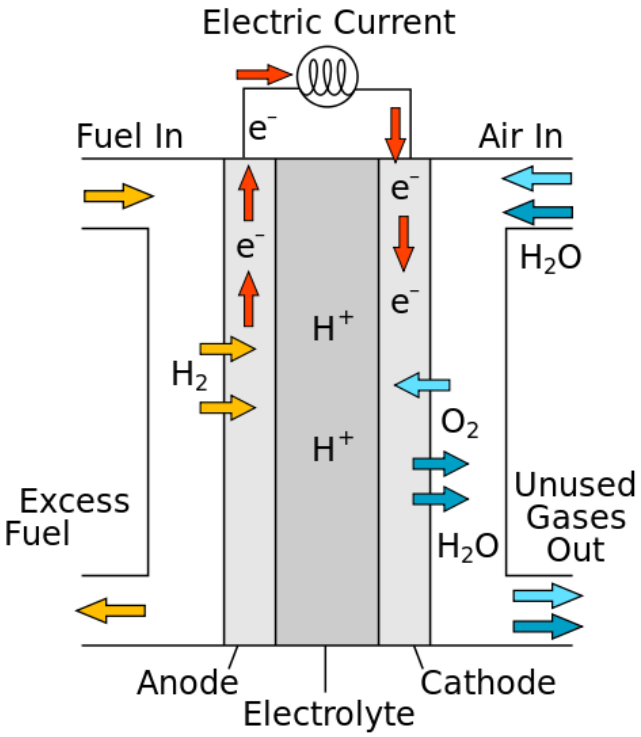

Fig. 1.8. Scheme of a proton-conducting fuel cell [9].

1.3.2 Principle of Secondary Batteries

Among the various types of batteries, secondary batteries are the most suitable for high-drain applications since they are more cost-efficient over the long term.

The principle of secondary batteries is shown in Fig. 1.9. During charging, the positive active material is oxidized, producing electrons, and the negative material is reduced, consuming electrons. These electrons constitute the current flow in the external circuit [10].

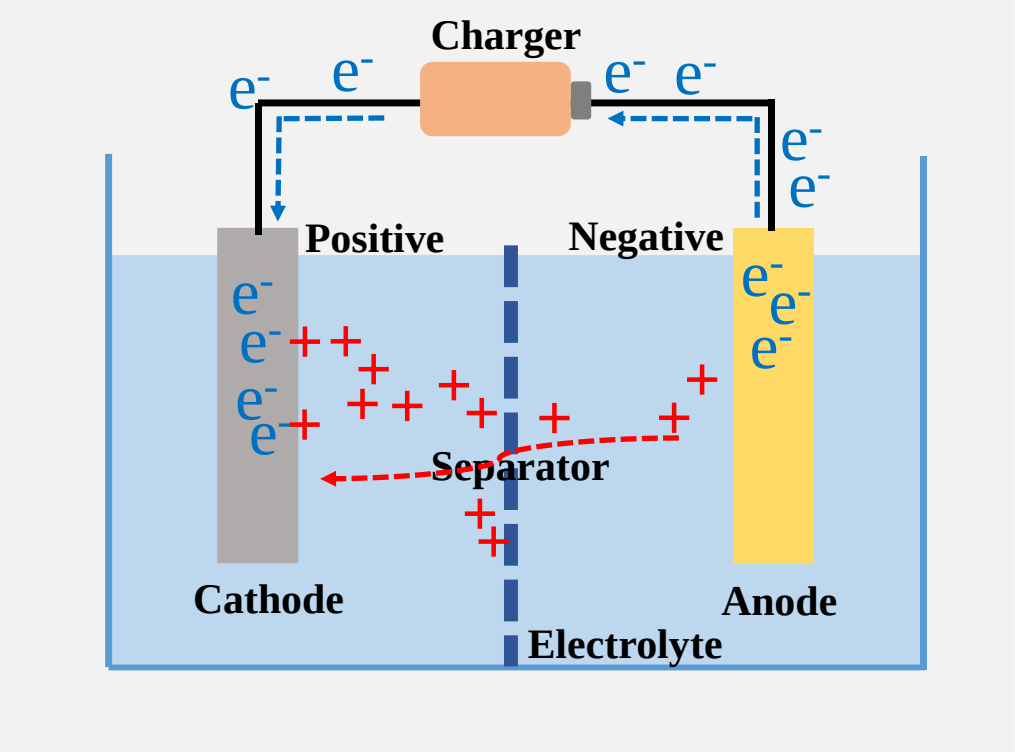

Fig. 1.9. Diagram of the charging process of a secondary battery.

1.3.3 Performances of Secondary Batteries

Figure 1.10 shows the performances of secondary batteries. Among the secondary batteries, the LIB, which was developed in Japan by Asahi Kasei Co. and first commercialized by Sony Co. in 1991, has a high energy density owing to lithium having a low atomic number. Hence, LIBs soon entered widespread use owing to their good performance. Nowadays, LIBs are mainly used for portable electronics, especially smartphones and laptops. Furthermore, motor companies are attempting to adapt LIBs for use in electric vehicles. Fig. 1.11 reveals that LIBs have many applications compared with other types of batteries, such as lithium ion capacitors, electrical double-layer capacitors, and lead-acid batteries.

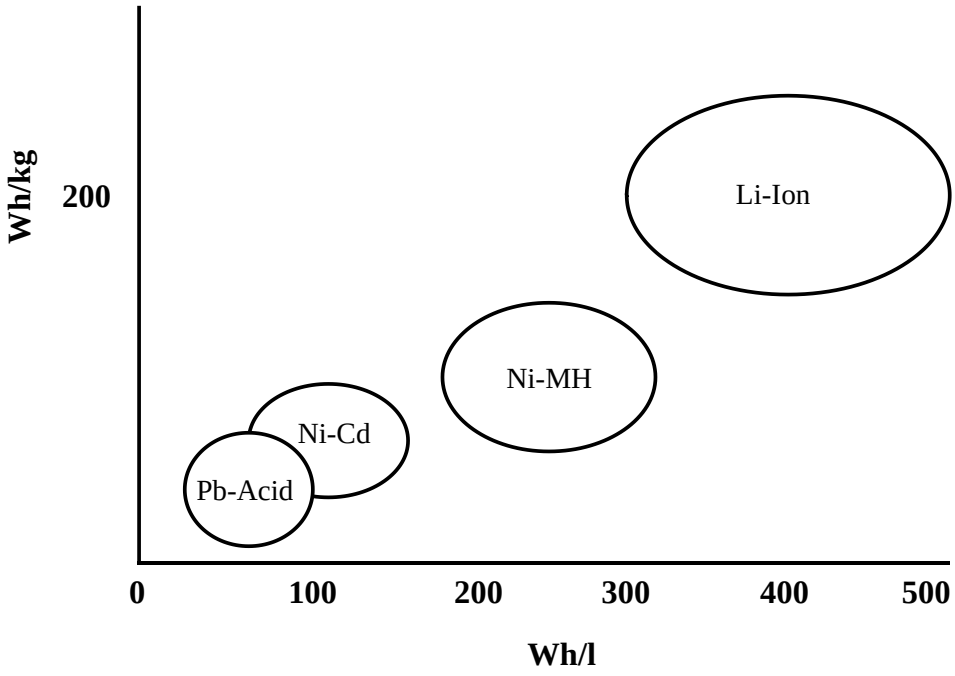

Fig. 1.10. Energy density (Wh/l) and specific energy (Wh/kg) for the major rechargeable battery systems [11].

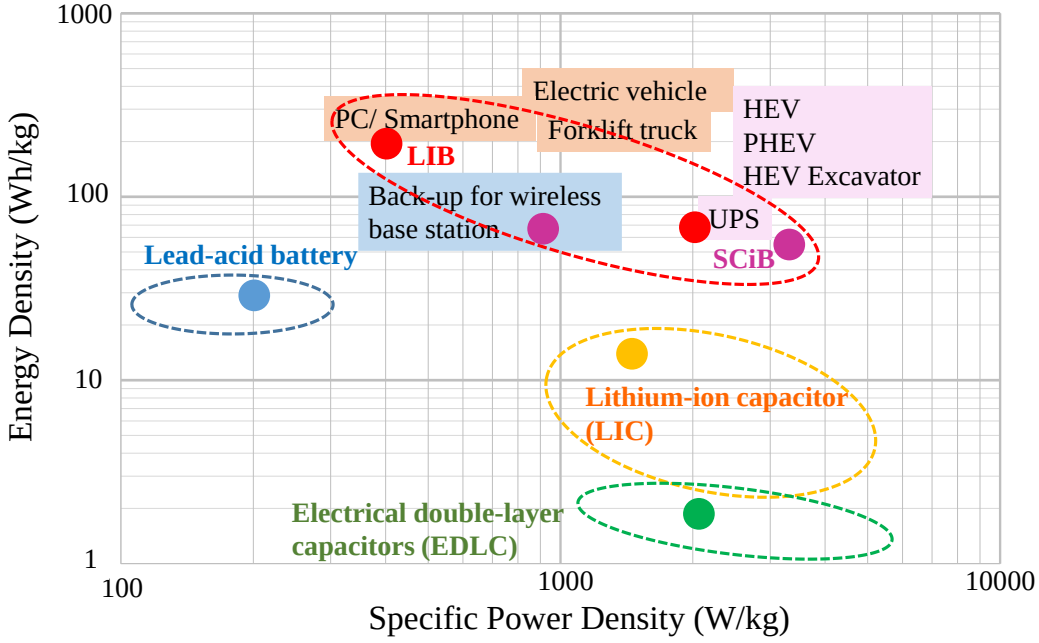

Fig. 1.11. Main types of batteries for various applications taken from the NEDO Roadmap.

Fig. 1.12 shows a typical LIB. The positive electrode is $LiCoO_2$, and the negative electrode is carbon. The battery is charged and discharged through the transport of Li^+ ions between the positive and negative electrodes. Electrons are exchanged by the process of Li^+ ion insertion and extraction. The electrode materials are layered compounds and only Li^+ ions take part in the charge and discharge reactions, which makes the reaction simple. Equations (1.1), (1.2), and (1.3) show the reaction formulae of the charging and discharging processes.

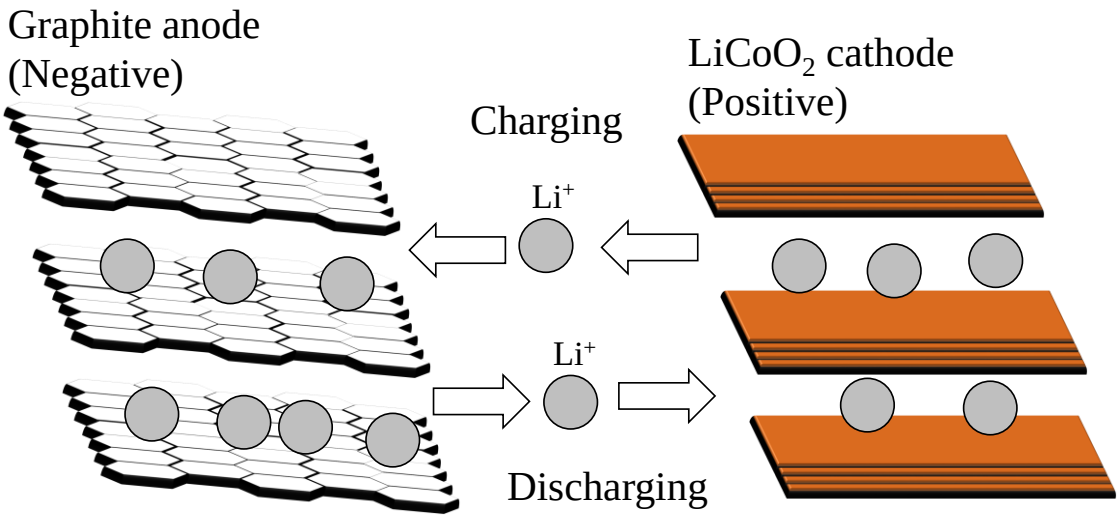

Fig. 1.12. Schematic illustration of the reactions in a lithium-ion battery [7].

Positive electrode: $$Li_{1-x}CoO_2 + xLi^+ + xe^- \underset{\text{charging}}{\overset{\text{discharging}}{\rightleftharpoons}} LiCoO_2 \quad (1.1)$$

Negative electrode: $$Li_xC \underset{\text{charging}}{\overset{\text{discharging}}{\rightleftharpoons}} C + xLi^+ + xe^- \quad (1.2)$$

Battery: $$Li_{1-x}CoO_2 + Li_xC \underset{\text{charging}}{\overset{\text{discharging}}{\rightleftharpoons}} LiCoO_2 + C \quad (1.3)$$

1.3.4 Importance of High-Speed Charge/Discharge

The high-speed charge/discharge of LIBs is an urgently needed technology in today's society. It will enable the use of LIBs in electric vehicles and as a back-up for solar energy, which requires a huge instantaneous current. For example, the Nissan Leaf electric vehicle requires about 30 min to be charged to 80% under rapid charging operation and about 8 h to be fully charged. To meet the needs of most users, the charge speed has to be increased greatly. Furthermore, medical equipment also requires a large instantaneous current in the case of sudden power failure to avoid putting lives at risk.

Furthermore, as smart grids are currently being developed and expected to be realized practically in the near future, emergency power sources that can provide a large instantaneous current are becoming increasingly necessary to solve the problem of sudden power outage.

1.3.5 Relationship between Internal Resistance and Charge/Discharge Speed

It is considered that for HEVs, the general goal for the charge/discharge rate is 100C rate. Here, the C rate is the current when the total capacity of the battery is charged or discharged in 1 h. A 100C rate means the battery is discharged with a current that is 100 times that for a 1C rate. In other words, it is necessary that the battery can be charged to full capacity in 36 s and also be discharged in 36 s.

A relationship concerning the C rate is given by Eq. (1.4), where m [g/cm^2] is the amount of active material per unit area of the electrode, σ [Ω cm^2] is the internal resistance per unit of the electrode of the battery, Q [Ah/g] is the theoretical capacity of

the active material, and η [V] is the overvoltage based on the thermodynamic equilibrium potential [12]. From Eq. (1.4), it can be observed that the internal resistance σ is the key factor determining the high-rate charge/discharge performance of the electrode.

$$m \le \frac{\eta}{\sigma Q C} \qquad (1.4)$$

The internal resistance consists of several types of resistances: a) metal resistance, b) surface oxide film insulation resistance, c) electron resistance, d) contact resistance, e) ion diffusion resistance, f) reaction resistance, and g) ion conduction resistance, as shown in Fig. 1.13. However, which type of resistance is the main factor impacting the charge/discharge speed is not yet clear. In this work, the electron resistance and reaction resistance will be focused on from the viewpoint of electron conduction.

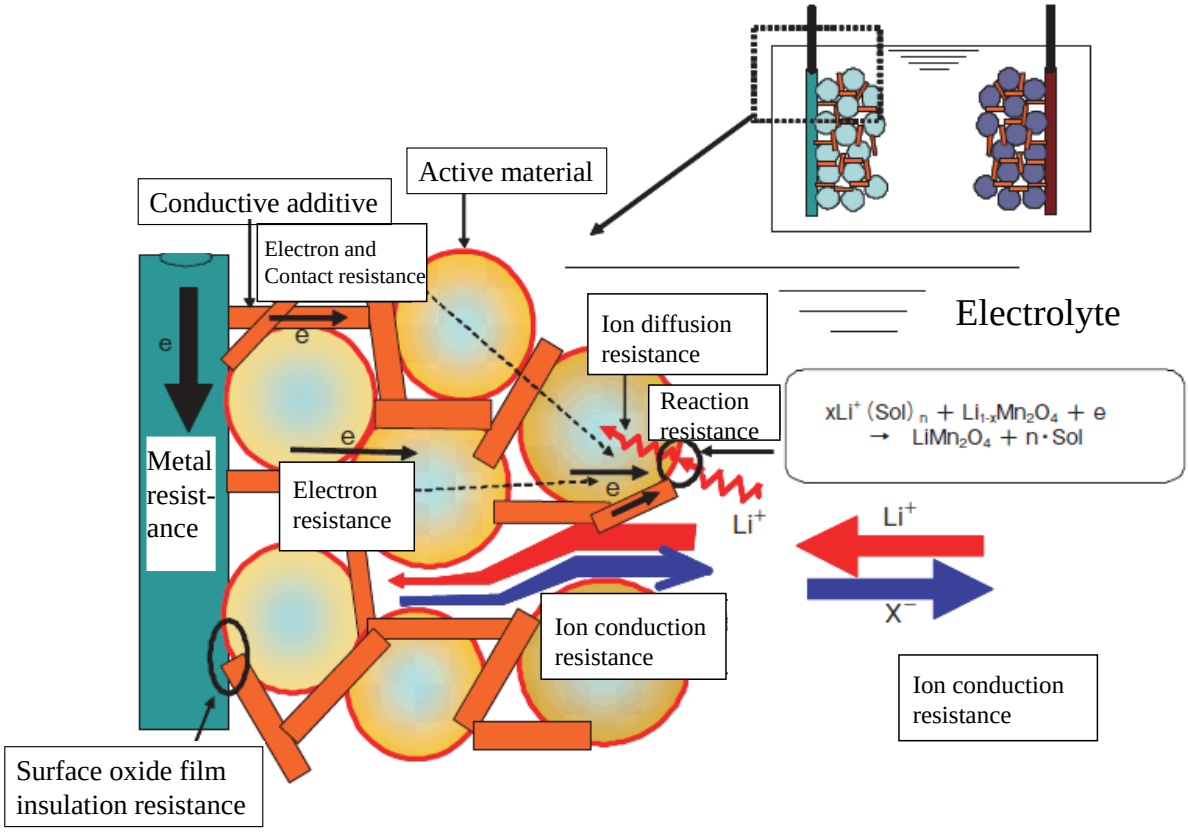

Fig. 1.13. Schematics of the internal resistance of batteries [12].

1.4 Purpose of This Work

LIBs are expected to be the most advanced means of energy storage in the near future [13-16]. The charge/discharge time is becoming increasingly important when evaluating the performance of batteries for their use in electric vehicles and other applications [16]. Although considerable effort has been made to study Li ion transportation to increase the charge/discharge speed [16-19], there has been little research on electron conduction to our knowledge. However, electrons and lithium ions both play important roles in determining the charge/discharge speed [20].

In this work, we attempted to increase the charge/discharge speed of LIBs from the viewpoint of electron conduction in the electrodes. Tungsten trioxide (WO_3) was chosen for the electrode material in this study. To improve the charge/discharge speed, it is necessary to develop processes that can increase the electron conductivity of crystalline WO_3 thin films. Thus, the electron transport mechanisms of WO_3 thin films were studied.

This thesis consists of six chapters as shown in Fig. 1.14.

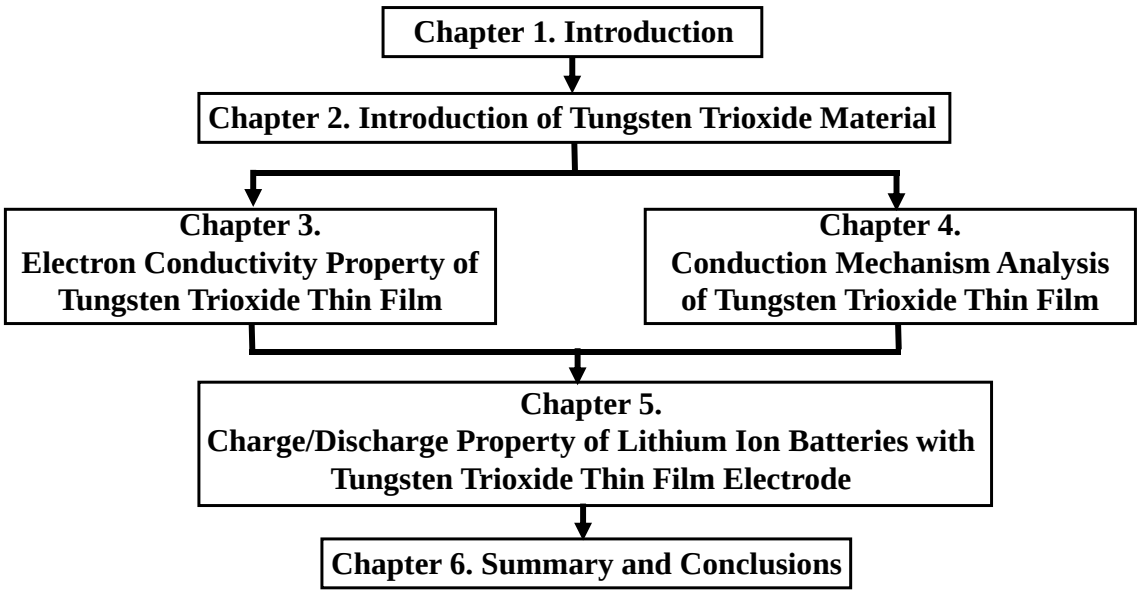

Fig. 1.14. Flow chart of this thesis.

In chapter 1, an introduction to the current status and future demand for energy has been given, as well as a simple outline of energy storage equipment, especially batteries. The importance of the high-speed charge/discharge of LIBs was discussed.

In chapter 2, a detailed introduction to WO_3 is given from various research aspects, such as its crystalline structure, electrochemical properties, electron conductivities, and so forth.

In chapter 3, the electron resistivity measurement method used in this thesis and experimental data for WO_3 thin films under different annealing conditions are given.

In chapter 4, on the basis of the experimental data for the electron resistivity, the conduction mechanism of WO_3 thin film is analyzed by resistivity fitting. Two types of electron mechanism are demonstrated to take part in electron conduction in WO_3 thin film.

In chapter 5, the charge/discharge property of LIBs with WO_3 thin film electrodes is studied. Also, the dependence of the crystalline structure of WO_3 thin film on the annealing conditions is investigated and discussed.

In chapter 6, a summary of this thesis is given, and future work worthy of further investigation is suggested.

Reference List

[1] A. Sieminski, *International Energy Outlook 2014*. USA: U.S. Energy Information Administration, 2014.

[2] A. Sieminski, *International Energy Outlook 2013*. USA: U.S. Energy Information Administration, 2013.

[3] http://www.emarketer.com/Article/Smartphone-Users-Worldwide-Will-Total-175-Billion-2014/1010536

[4] http://www.emarketer.com/Article/Smartphone-Users-Worldwide-Will-Total-175-Billion-2014/1010536

[5] http://laurageography.wordpress.com/

[6] http://www.eia.gov/todayinenergy/detail.cfm?id=5130

[7] Z. Ogumi and K. Nishio, *革新型蓄電池のすべて (All of Innovative Storage Batteries)*. Ohmsha, 2011.

[8] http://en.wikipedia.org/wiki/Daniell_cell

[9] http://en.wikipedia.org/wiki/Fuel_cell

[10] http://en.wikipedia.org/wiki/Rechargeable_battery

[11] M. Yoshio, R. J. Brodd, and A. Kozawa, *Lithium-Ion Batteries: Science and Technologies*. New York: Springer Science+Business Media, LLC, 2009.

[12] N. Tatsuo, ``高速充放電リチウムイオン二次電池の開発 (Express Charging/Discharging Lithium Ion Secondary Batteries)," *FB Technical News*, no. 64, pp. 3-18, 2008.

[13] B. Scrosati, ``Battery technology-challenge of portable power," *Nature*, vol. 373, no. 6515, pp. 557-558, 1995.

[14] A. R. Armstrong and P. G. Bruce, ``Synthesis of layered $LiMnO_2$ as an electrode for

rechargeable lithium batteries," *Nature*, vol. 381, pp. 499-500, 1996.

[15] N. Li, C. R. Martin, and B. Scrosati, ``Nanomaterial-based Li-ion battery electrodes," *J. Power Sources,* vol. 97, pp. 240-243, 2001.

[16] V. Etacheri, R. Marom, R. Elazari, G. Salitra, and D. Aurbach, ``Challenges in the development of advanced Li-ion batteries: a review," *Energy Environ. Sci.*, vol. 4, pp: 3243-3262, 2011.

[17] H. Zhao, Y. Li, Z. Zhu, J. Lin, Z. Tian, and R. Wang, ``Structural and electrochemical characteristics of $Li_{4-x}Al_xTi_5O_{12}$ as anode material for lithium-ion batteries," *Electrochim. Acta*, vol. 53, pp. 7079-7083, 2008.

[18] Y. Q. Wang, L. Gu, Y. G. Guo, H. Li, X. Q. He, S. Tsukimoto, Y. Ikuhara, and L. J. Wan, ``Rutile-TiO_2 nanocoating for a high-rate $Li_4Ti_5O_{12}$ anode of a lithium-ion battery," *J. Am. Chem. Soc.*, vol. 134, pp. 7874-7879, 2012.

[19] X. Y. Fan, Y. Li, J. J. Wang, L. Gou, P. Zhao, D. L. Li, L. Huang, and S. G. Sun, ``Synthesis and electrochemical performance of porous Li_2FeSiO_4/C cathode material for long-life lithium-ion batteries," *J. Alloys Compd.*, vol. 493, pp. 77-80, 2010.

[20] S. H. Lee, H. M. Cheong, C. E. Tracy, A. Mascarenhas, R. Pitts, G. Jorgensen, S. K. Deb, ``Influence of microstructure on the chemical diffusion of lithium ions in amorphous lithiated tungsten oxide films," *Electrochim. Acta,* vol. 46, pp. 3415-3419, 2001.

Chapter 2 Introduction of Tungsten Trioxide

2.1 Introduction

2.2 Semiconductor Properties of Tungsten Trioxide

2.2.1 Bandgap of WO_3

2.2.2 Electrical Properties of Semiconductor WO_3

2.3 Crystalline Structures

2.4 Electrochromic Characteristic

2.5 Applications of Tungsten Trioxide

2.5.1 Smart Windows

2.5.2 Photocatalyst

2.5.3 Gas-Sensing Devices

2.6 Conclusion

Reference List

2.1 Introduction

In the last few decades, many transition metal oxides such as tungsten, nickel, iridium, vanadium, titanium, cobalt, and molybdenum have been examined with respect to their use in electrochromic applications [1-4]. However, WO_3 is a key material because of its multiple valence states, high coloration efficiency, good stability, high capacity for reversible Li^+ insertion, and highly reversible intercalation properties. Moreover, WO_3 is non-toxic. In addition, thin films can be produced by low-cost techniques such as spray coating.

In this chapter, the semiconductor properties of WO_3 are introduced, including its bandgap and n-type property due to oxygen vacancies. Also, some typical crystalline structures of WO_3 are introduced, i.e., cubic, tetragonal I, and hexagonal structures. Moreover, the electrochromic characteristic is discussed in a separate subsection owing to its various applications, such as smart windows, gas sensors, a photocatalyst, the electrodes of LIBs, and so forth.

2.2 Semiconductor Properties of Tungsten Trioxide

2.2.1 Bandgap of WO_3

Tungsten trioxide (WO_3) is a wide-bandgap semiconductor. Its bandgap energy has mainly been measured by optical absorption, to be from about 2.6 to 3.0 eV. The valence band is dominated by the O 2p states, while W 5d states dominate the conduction band [5].

Also, it has been reported that the bandgap depends on the preparation conditions of

the material as shown in Fig. 2.1. It shows a monotonic decrease in E_g from 3.25 to 2.7 eV with increasing substrate temperature. The decrease is most rapid above 300 ^oC, which indicates that crystallization causes the bandgap to narrow [1].

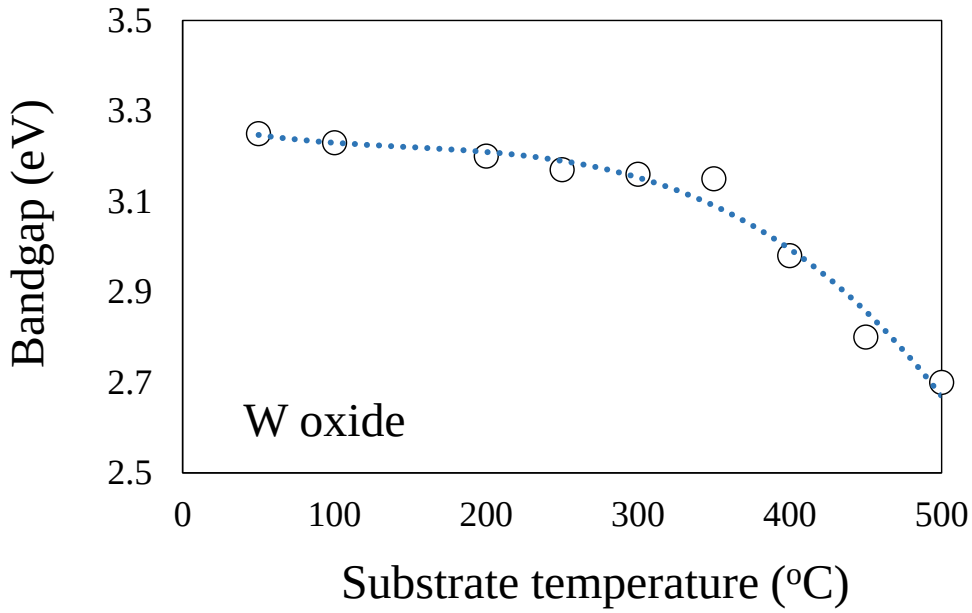

Fig. 2.1. Bandgap for W oxide films evaporated onto heated substrates [6].

There has been some investigation concerning the effect of ion intercalation on E_g. Although the reason is not yet clear, E_g enhancement upon the insertion of ions and electrons has been reported. As shown in Fig. 2.2, $Li_{0.13}WO_3$ shows an increase in E_g of ~0.1 eV compared with the unintercalated material, and E_g is increased by ~0.25 eV at the maximum Li ion content.

(a) (b) (c)

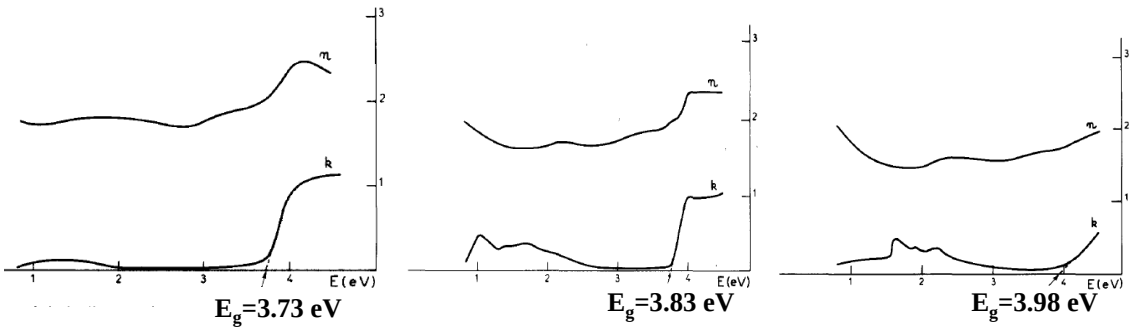

Fig. 2.2. Optical indices of ex situ film (a), colored sample (insertion rate x= 0.13) (b), and colored sample (maximum coloration) (c) [7].

2.2.2 Electrical Properties of Semiconductor WO_3

WO_3 is an n-type semiconductor whose electron concentration is determined mainly by the concentration of stoichiometric defects such as oxygen vacancies as shown in Fig. 2.3.

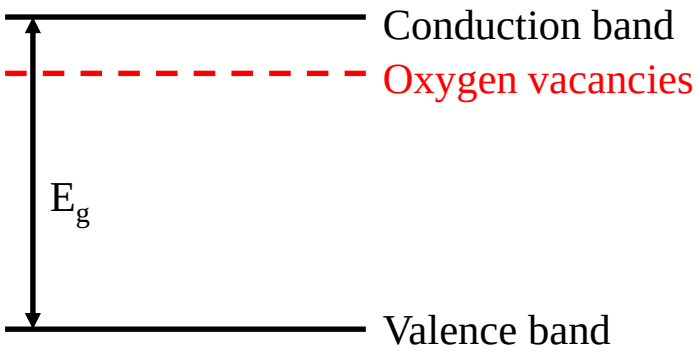

Fig. 2.3. Schematic illustrating origin of conduction in n-type semiconductor WO_3 using oxygen vacancies.

To investigate the existence of oxygen vacancies in WO_3, the photoluminescence (PL) measurement of WO_3 heat-treated by N_2-annealing at 300 ^oC and 700 ^oC was carried out, and the spectra shown in Figs. 2.4 (a) and (b) were observed. Two PL peaks were observed at approximately 720 nm and 610 nm where the latter appears as a shoulder for the WO_3

heat-treated at 300 ^{o}C, whereas a weak PL peak was recognized at approximately 720 nm for the WO_3 heat-treated at 700 ^{o}C. Two reasons are considered for the appearance of the PL emission. First, the PL can be ascribed to the residual hydrocarbons after the heat treatment at 300 ^{o}C, and the origin of the hydrocarbons is thought to the binder for the WO_3 particles coated on the substrate. Graphite does not emit PL since it has no bandgap. Hydrocarbons are an insulator in terms of the electrical meaning and are transparent in the visible wavelength region, both of which indicate the presence of a bandgap. The intense PL peaks are considered to be due to the residual hydrocarbons mixed with amorphous carbon, the presence of which can be seen in the wavelength range from 550 to 570 nm in the PL spectra. Second, the appearance of the intense PL is thought to be due to the defects inside the WO_3 particles heat-treated at 300 ^{o}C. The bandgap of WO_3 is on the order of about 2.8 eV, and the direct transition of electrons between the valence and conduction bands produces a PL peak at 443 nm. The shoulder peak at 610 nm appears to be related to the recombination reaction between oxygen vacancies and electrons in the WO_3, and the PL peak at 720 nm can be assigned to the presence of residual hydrocarbons and amorphous carbon since this PL peak was confirmed to almost disappear for the WO_3 heat-treated at 700 ^{o}C.

(a)

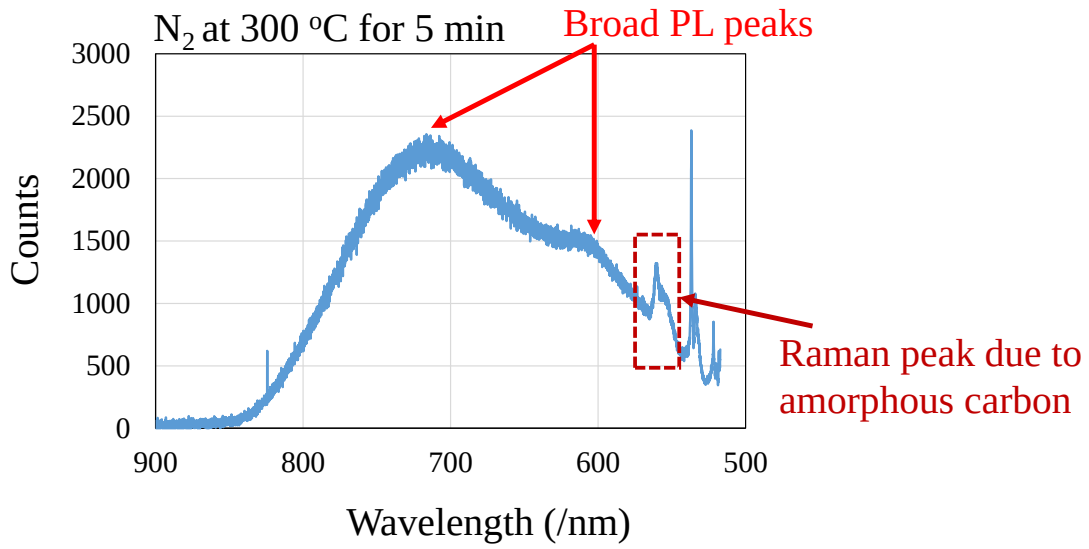

(b)

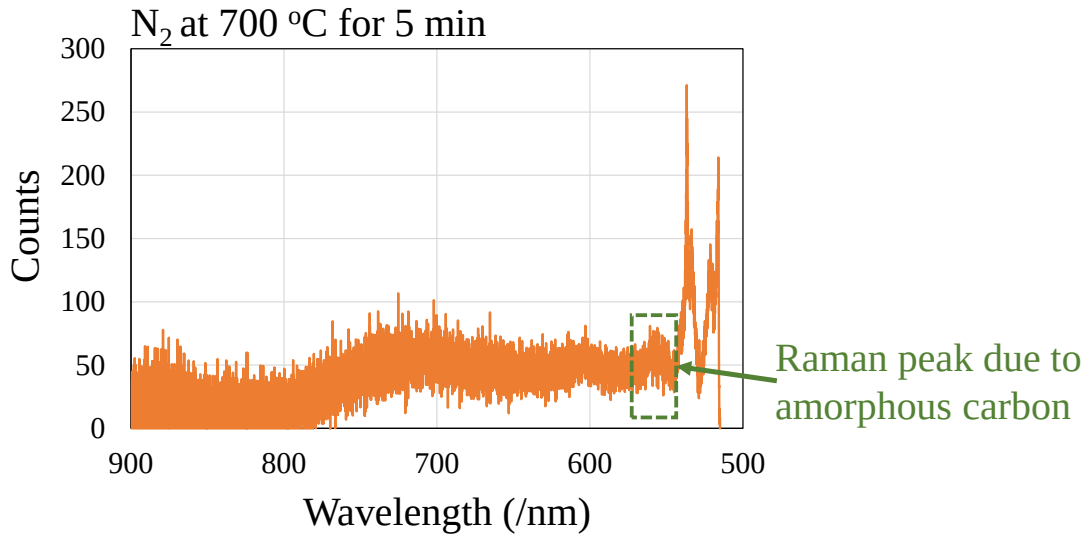

Fig. 2.4. Photoluminescence spectra of WO_3 heat-treated by N_2-annealing at 300 ºC (a) and 700 ºC (b).

The stoichiometric WO_3 has abrupt changes in conductivity and oxygen deficiency, and its conductivity increases by many orders of magnitude as shown in Fig. 2.5.

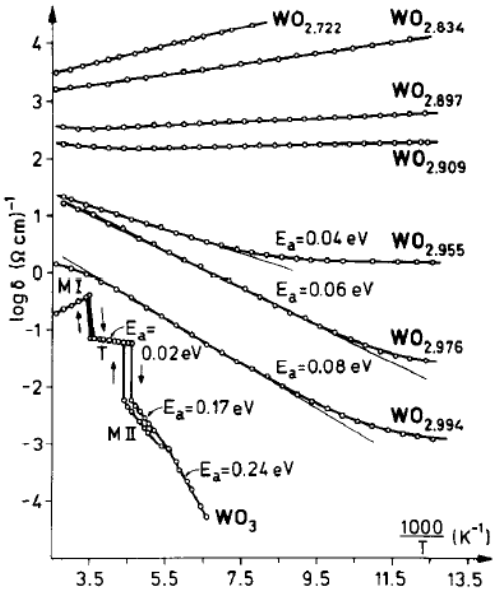

Fig. 2.5. Conductivity vs 1/T plots for WO_3 and WO_{3-x}. M I, T, and M II refer to monoclinic I, triclinic, and monoclinic II WO_3 [8].

2.3 Crystalline Structures

WO_3 crystals have perovskite-like atomic configurations based on corner-sharing WO_6 octahedra. However, tungsten oxide tends to form substoichiometric phases containing edge-sharing octahedra as shown in Fig. 2.6 [1].

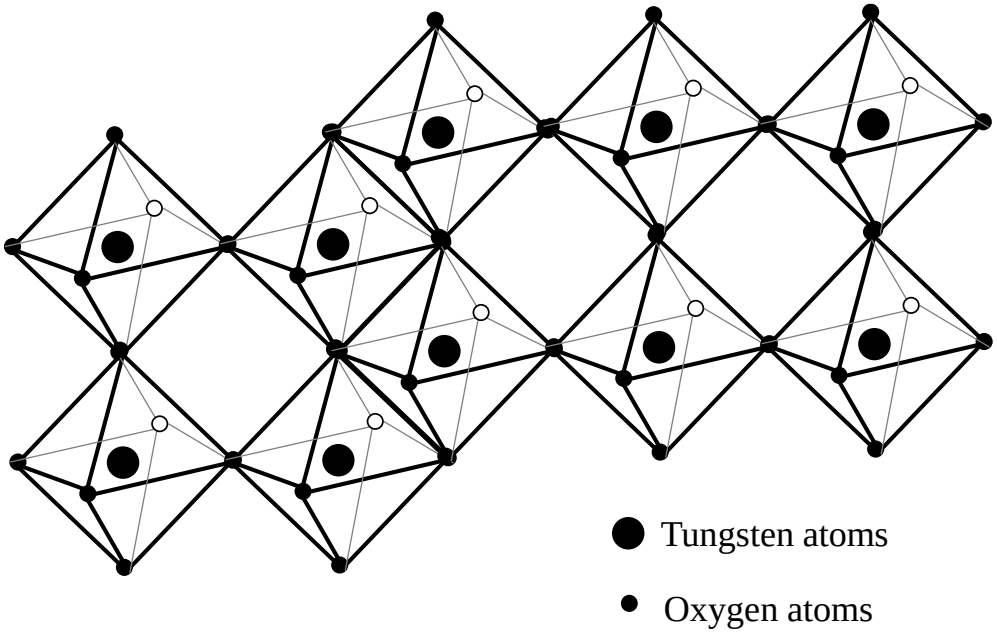

Fig. 2.6. Schematic illustrating corner-sharing and edge-sharing octahedra in a tungsten oxide crystal.

Fig. 2.7 illustrates the two main types of crystal structures of WO_3: the cubic and hexagonal structures.

(a)

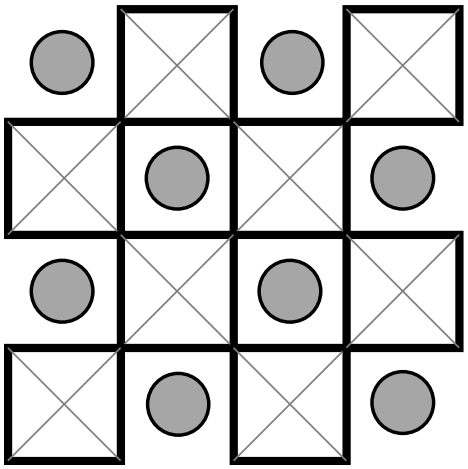

(b)

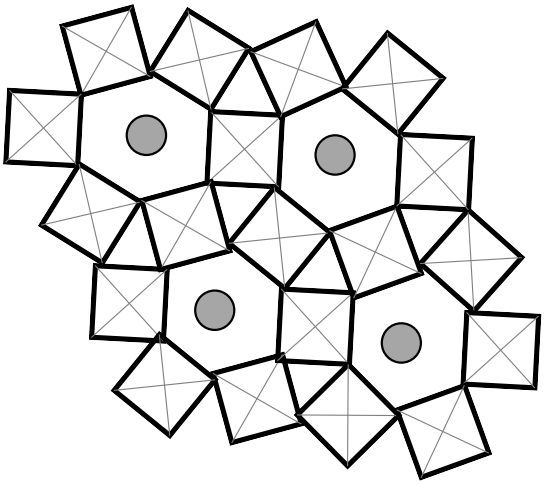

○ Sites available for ion insertion

Fig. 2.7. Atomic arrangements of crystalline tungsten bronzes with (a) cubic and (b) hexagonal structures.

The modifications of the crystalline structure during Li^+ intercalation/deintercalation have been reported as shown in Fig. 2.8. It can be observed that Li^+ intercalation induces a transform from monoclinic to tetragonal then to cubic with intermediate mixed phases. Deintercalation induces the opposite transformation but the phase changes do not occur at the same Li contents. The monoclinic structure is stable for $x<0.01$, and the tetragonal structure is stable at $x=\sim0.1$. The cubic is stable at $x>0.36$ in the case of intercalation and at $x>0.21$ in the case of deintercalation [1].

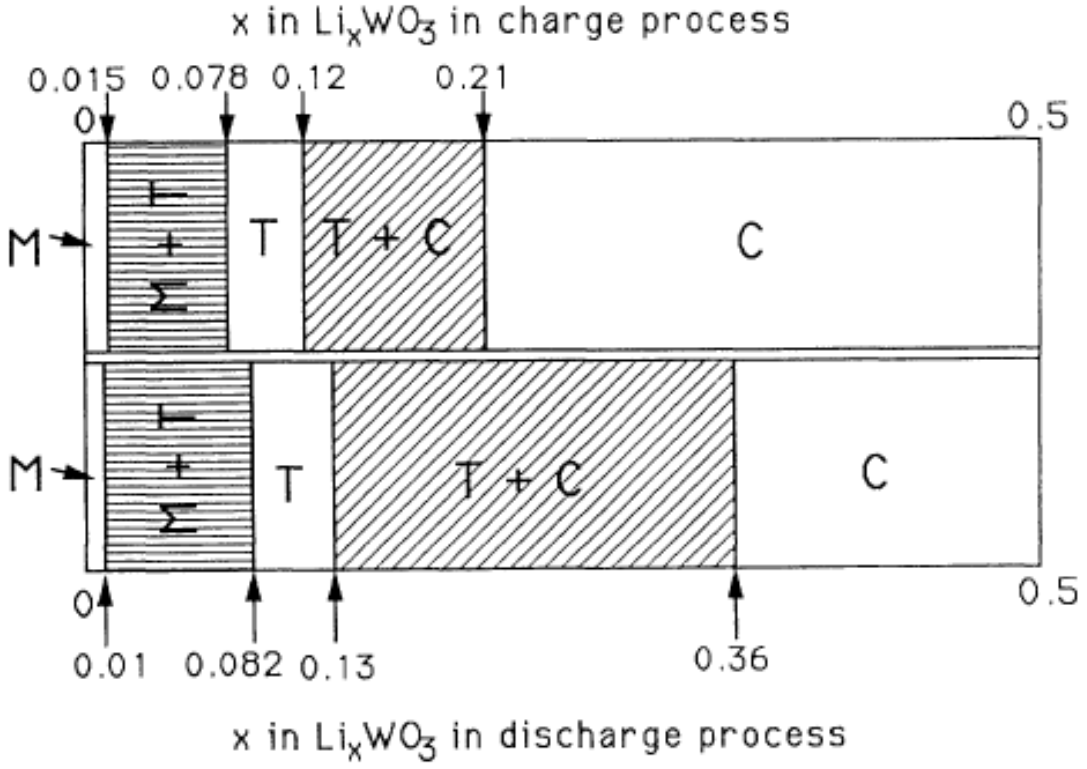

Fig. 2.8. Phase diagram for $LiWO_3$ electrochemically formed at room temperature [10].

2.4 Electrochromic Characteristic

An electrochromic material is characterized by its ability to undergo reversible and sustained changes in its optical properties when a voltage is applied to it. These properties can be easily controlled and therefore electrochromic materials have a wide range of applications. They can be used not only for ‘smart windows’ in buildings, which are capable of varying the throughput of visible light and solar energy, but also in cars and trucks, information displays, ski goggles, and motorcycle helmet visors [11].

The electrochromic phenomenon has been discovered in W oxide thin films, which remain the most promising material for electrochromic devices. The principle of W oxide

electrochromic devices can be summarized by the simple reaction

$$WO_3 + xM^+ + xe^- \leftrightarrow M_xWO_3 \quad (2.1)$$

where $M^+=H^+$, Li^+, Na^+, or K^+, and e^- denotes electrons. When W oxide, which is transparent as a thin film, incorporates electrons and ions, it can be reversibly transformed to a material with different properties; it is absorbing if it is heavily disordered and infrared-reflecting if it is crystalline [5]. Fig. 2.9 shows a five-layer electrochromic device structure that can be formed on a transparent substrate or between two transparent substrates. An electrolyte is set in the center, which is usually a polymer layer or a thin film of a hydrous oxide. On the right side of the electrolyte is a thin film of an electrochromic material, typically WO_3. On the left side of the electrolyte is an ion storage thin film, with or without electrochromism, usually an oxide film. Thin films with transparent and electrically conducting properties (such as ITO) are necessary as electrodes on the two sides. Applying a voltage of only 1–2 V d.c. across the ITO films can make ions move into or out of the WO_3 film, changing its optical absorption. The device has open-circuit memory; thus, only the voltage needs to be applied to alter the optical absorption, and the device retains its properties until another voltage is applied.

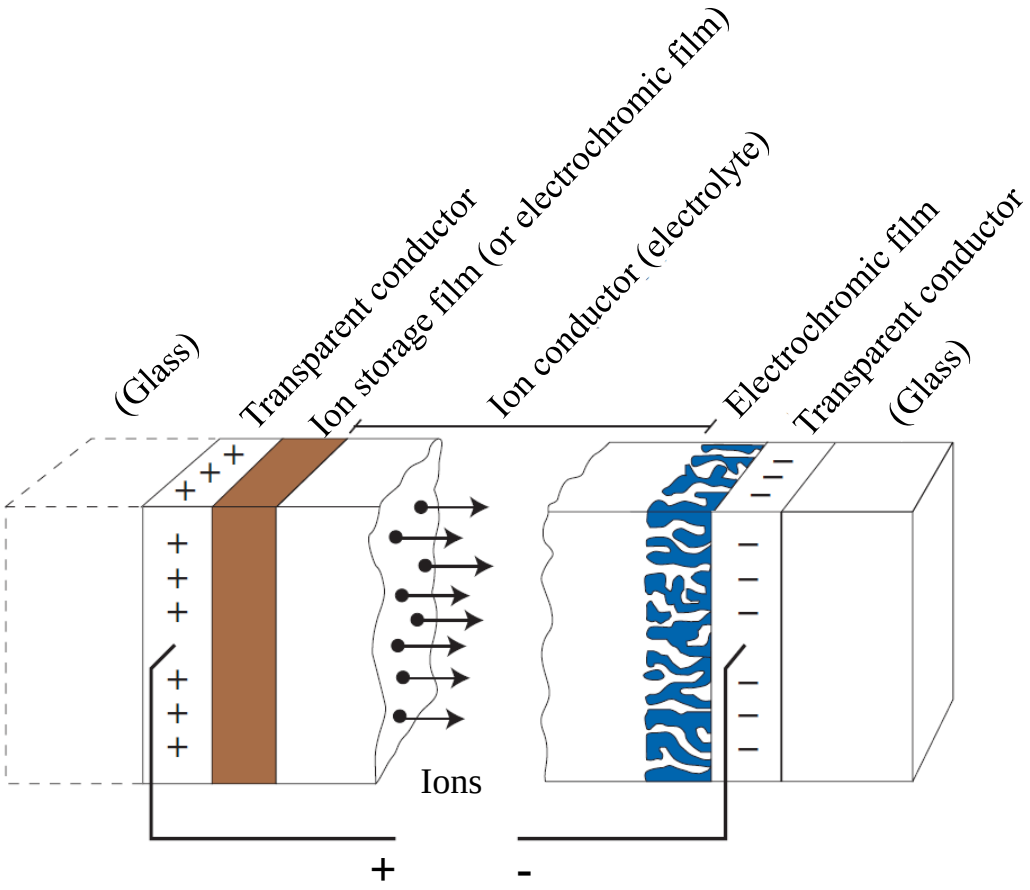

Fig. 2.9. Electrochromic device design, showing the movement of ions under an externally applied electric field [11].

Fig. 2.10 illustrates the transmittance of the electrochromic device in the fully colored and bleached states and with intermediate coloration. At λ=0.55 μm, the transmittance can be varied between ~13% and75%.

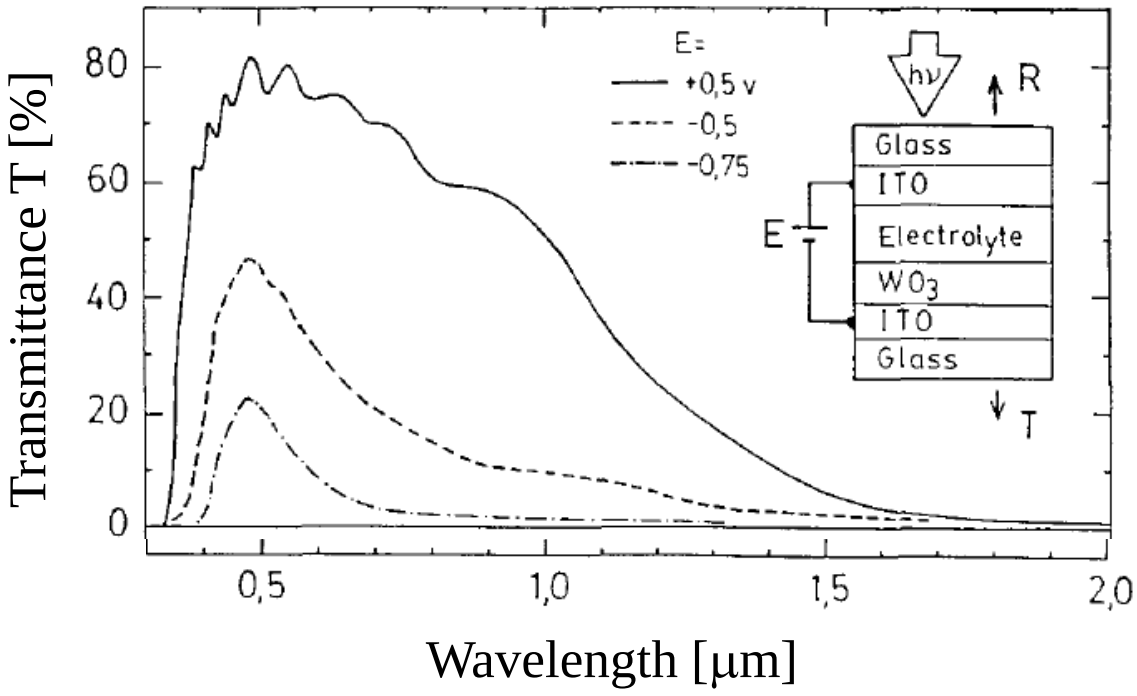

Fig. 2.10. Measured spectral transmittance as a function of applied voltage (E) [12].

For use in electrochromic devices, the WO_3 film must be thin and should be fabricated by a sputtering process and then annealed to change the amorphous film into a monoclinic thin film. The cycling life has been reported to be 10^5–10^6 cycles.

On the other hand, on the basis of its electrochromic property, WO_3 can also be used for the electrodes of LIBs. In the recharging and discharging processes of LIBs, lithium ions are respectively intercalated into and released from the cavities of a crystalline WO_3 thin film. When WO_3 is used as a positive electrode, Eq. (2.2) describes the discharge process and Eq. (2.3) describes the charge process. On the other hand, when WO_3 is used as a negative electrode, Eq. (2.2) describes the charge process and Eq. (2.3) describes the discharge process.

$$WO_3 + xM^+ + xe^- \rightarrow M_xWO_3 \quad (2.2)$$

$$M_xWO_3 \rightarrow WO_3 + xM^+ + xe^- \quad (2.3)$$

In this situation, a thick film of WO_3 is needed for ion storage. Such a film should be fabricated by a low-cost method, such as spray coating. The cycling life of LIBs with WO_3 electrodes has been reported to be 3000 cycles.

2.5 Applications of Tungsten Trioxide

Owing to its optical, chemical, and electronic properties, WO_3 has direct applications in electrochromic devices, photocatalysts, gas-sensing devices, and other devices. [13]

2.5.1 Smart Windows

A smart window refers to glass or glazing that changes its light transmission properties under the application of voltage, light, or heat. It can thus control the amount of light transmission. When activated, the glass changes from transparent to translucent, blocking some wavelengths of light [14]. The ability makes it possible to cool or warm up a room and thereby save energy costs.

WO_3 which is a well-known electrochromic material, has been studied for its application to smart windows since it can change color to reflect or absorb light when a low-voltage electrical current is applied. Fig. 2.11 shows a smart window using WO_3 and Eq. (2.4) gives the formula describing the electrochromic principle.

Fig. 2.11. Smart window using WO_3.

$$\underset{\text{transparent}}{WO_3 + xM^+ + xe^-} \rightleftharpoons \underset{\text{color}}{M_xWO_3} \quad (2.4)$$

2.5.2 Photocatalyst

When a photocatalyst captures light, oxidation and reduction reactions can occur at its surface. This property can decompose organic compounds near the surface of the photocatalyst. Because of its catalytic nature, photocatalysts are not consumed during the chemical reaction. The treated surface regenerates its photocatalytic effect by reacting with oxygen in the air.

There are two main types of photocatalyst: ultraviolet-light-responsive and visible-light-responsive. Ultraviolet-light-responsive photocatalysts are widely used in the external walls of buildings [15]. Compared with TiO_2 which has a bandgap of about 3.2

eV and utilizes solar energy, WO_3 has a smaller bandgap, indicating its possible use as a photocatalyst under visible light, for example, as an indoor deodorant or as an antibacterial and antifungal agent in building materials or furniture [16].

Using energy from light, WO_3 creates two oxidation reactants: hydroxyl radicals and H_2O_2, which decompose toxic organic substances by oxidation, as shown in Fig. 2.12.

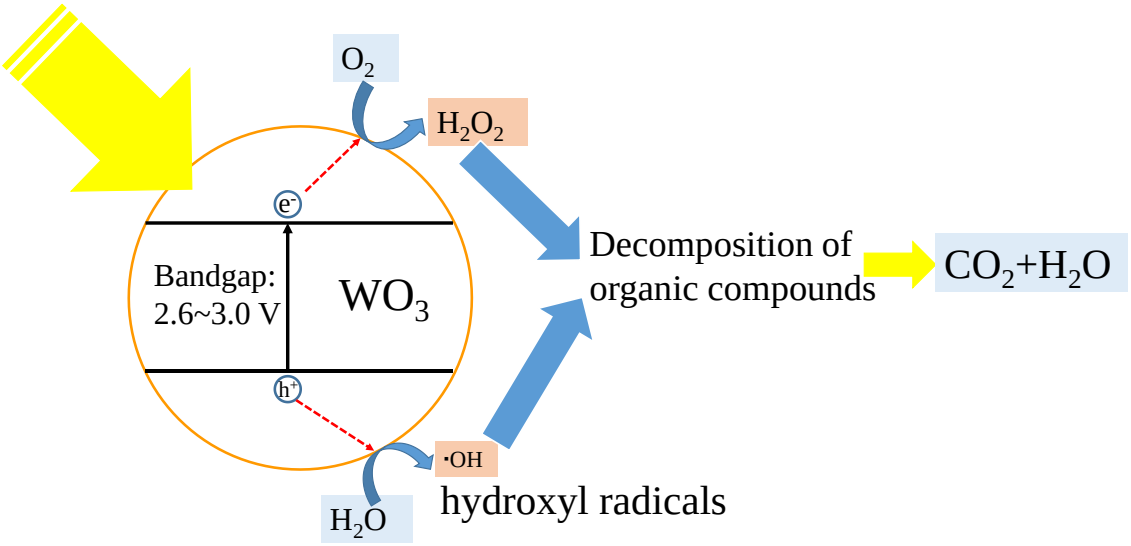

Fig. 2.12. Model of photocatalyst [17].

2.5.3 Gas-Sensing Devices

The working principle of gas-sensing devices is based on the modulation of electrical conductivity due to surface oxidation or reduction caused by gas exposure. Since only the surface layer is affected by such reactions, the sensitivity is strongly dependent on the surface-to-volume ratio of the material used. Thus, high-porosity materials are used in these devices [18].

WO_3, which can exhibit high porosity, as shown in Fig. 2.13 (a), and sensitivity to some gases, as shown in Fig. 2.13 (b), by controlling the fabrication process, is considered to be a promising gas sensor. The detection of H_2 using WO_3 was first reported by P. J.

Shaver [19], who showed that the conductivity of WO_3 films changed greatly upon exposure to H_2 ambient. Then, it was demonstrated by different authors that WO_3-based thin and thick films are both sensitive to NO_x gas. It was also reported that WO_3 materials have high sensitivity to low concentrations of NO_x gas [20].

(a) (b)

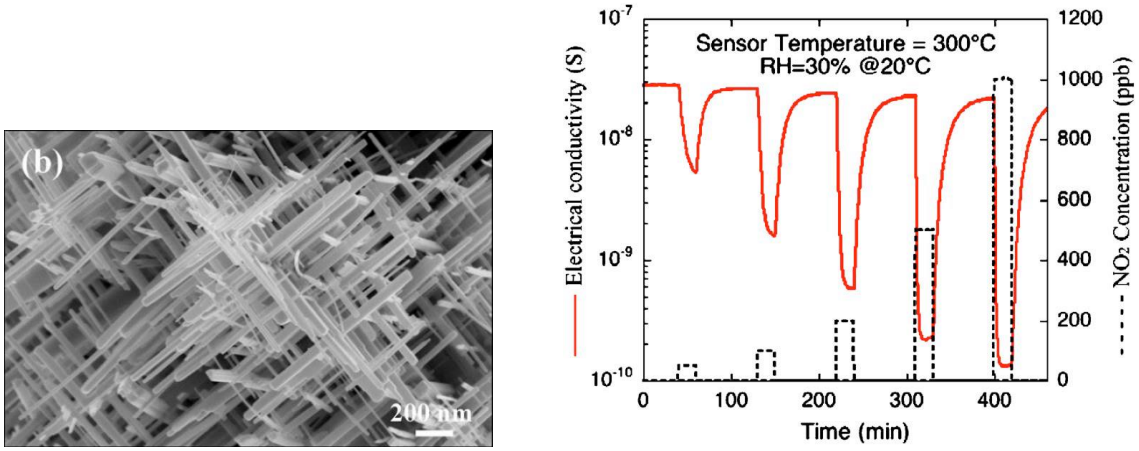

Fig. 2.13. (a) SEM image of tungsten oxide nanowire network. (b) Sensor response to NO_2 of different concentrations [18].

2.6 Conclusion

In this chapter, the semiconductor properties of WO_3 were illustrated, including bandgap modification due to ion intercalation and n-type semiconductor behavior due to oxygen vacancies. Some typical crystalline structures of WO_3 were introduced, i.e., cubic, tetragonal I, and hexagonal structures. Morover, the electrochromic characteristic was discussed in a separate subsection owing to its various applications, such as smart windows, gas sensors, a photocatalyst, electrodes of LIBs, and so forth. The principles of various applications of WO_3 were also introduced. Owing to its electrochromic characteristic, the application of WO_3 electrodes in LIBs is expected.

Reference List

[1] C. G. Granqvist, *Handbook of Inorganic Electrochromic Materials*. Elsevier, 1995.

[2] C.M. Lampert and C.G. Granqvist, ``Large-area chromogenics: Materials and devices for transmittance control," in *Proc. The International Society for Optical Engineering*, Sep. 1988.

[3] D. T. Gillaspie, R. C. Tenent, and A. C. Dillon, ``Metal-oxide films for electrochromic applications: present technology and future directions," *Journal of Materials Chemistry*, vol. 20, pp. 9585–9592, 2010.

[4] R. D. Rauh, ``Electrochromic windows: an overview," *Electrochimica Acta*, vol. 44, pp. 3165–3176, 1999.

[5] C. G. Granqvist, ``Electrochromic tungsten oxide films: review of progress 1993–1998," *Solar Energy Materials and Solar Cells*, vol. 60, no. 3, pp. 201-262, 2000.

[6] K. Miyake, H. Kaneko, M. Sano and N. Suedomi, ``Physical and electrochromic properties of the amorphous and crystalline tungsten oxide thick films prepared under reducing atmosphere," *Journal of Applied Physics*, vol. 55, no. 7, pp. 2747-2753, 1984.

[7] P. Delichere, P. Falaras, and A. H. Goff, ``Electrochromism in anodic WO_3 films II: Optical and electrochromic properties of coloured “distorted” hexagonal films," *Thin Solid Films*, vol. 161, pp. 47-58, 1988.

[8] W. Sahle and M. Nygren, ``Electrical conductivity and high resolution electron microscopy studies of WO_{3-x} crystals with $0 \leq x \leq 0.28$," *Journal of Solid State Chemistry*, vol. 48, no. 2, pp. 154-160, 1983.

[9] I. Webman, J. Jortner, and M. H. Cohen, ``Electronic transport in alkali-tungsten bronzes," *Physical Review B*, vol. 13, no.2, pp. 713-724, 1976.

[10] Q. Zhong, J. R. Dahn, K. Colbow, ``Lithium intercalation into WO_3 and the phase

diagram of Li_xWO_3," *Phys. Rev. B*, vol. 46, pp. 2554-2560, 1992.

[11] C. G. Granqvist, ``Electrochromic materials: out of a niche," *Nature materials*, vol. 5, no. 2, pp. 89-90, 2006.

[12] T. Kamimori, J. Nagai, and M. Mizuhashi, ``Electrochromic devices for transmissive and reflective light control," *Solar energy materials*, vol. 16, no. 1, pp. 27-38, 1987.

[13] F. Wang, C. D. Valentin, and G. Pacchioni, ``Rational band gap engineering of WO_3 photocatalyst for visible light water splitting," *ChemCatChem*, vol. 4, no. 4, pp. 476-478, 2012.

[14] http://en.wikipedia.org/wiki/Smart_glass

[15] I. M. Szilágyi, B. Fórizs, O. Rosseler, Á. Szegedi, P. Németh, P. Király, G. Tárkányi, B. Vajna, K. Varga-Josepovits, K. László, A. L. Tóth, P. Baranyai, M. Leskelä, ``WO_3 photocatalysts: influence of structure and composition," *Journal of Catalysis*, vol. 294, pp. 119-127, 2012.

[16] Presentation material from Toshiba Material Co., Ltd. ``Enhancement of decomposition rate of acetaldehyde gas by using visible light sensitive WO_3 photocatalyst controlled with crystal structure and particle size,"

[17] http://www.supesolar.com/mosquito-fly-trap/photocatalyst-mosquito-trap principle.htm

[18] A. Ponzoni, E. Comini, G. Sberveglier, J. Zhou, S. Z. Deng, N. S. Xu, Y. Ding and Z. L. Wang, ``Ultrasensitive and highly selective gas sensors using three-dimensional tungsten oxide nanowire networks," *Applied Physics Letters*, vol. 88, no. 20, pp. 203101-1-3, 2006.

[19] P. J. Shaver, ``Activated tungsten oxide gas detectors," *Applied Physics Letters*, vol. 11, no. 8, pp. 255-257, 1967.

[20] M. Akiyama, J. Tamaki, N. Miura and N. Yamazoe, ``Tungsten oxide-based semiconductor sensor highly sensitive to NO and NO_2," *Chemistry Letters*, vol. 9, pp. 1611-1614, 1991.

Chapter 3 Electron Conductivity Property of Tungsten Trioxide Thin Film

3.1 Introduction

3.2 Experiment Process

3.2.1 Device Fabrication Process

3.2.1.1 Device fabrication flow

3.2.1.2 Spray coating methods

3.2.2 Resistivity Measurement Process

3.2.2.1 The four-point probe method

3.2.2.2 Resistivity measurement process

3.2.2.3 Activation energy measurement method

3.3 Conductivity Property of Tungsten Trioxide Thin Film Depending on Different Annealing Conditions

3.3.1 Conductivity Property of Tungsten Trioxide Thin Film Depending on Different Annealing Conditions

3.3.2 Derivation of E_a values

3.4 Conclusion

Reference List

3.1 Introduction

WO_3 thin films, which are well known for their excellent ability to promote the reversible intercalation of lithium ions, are considered to be a possible cathode-active material for use in lithium ion rechargeable batteries [1]. Moreover, the porosity of WO_3 thin films makes it easier for lithium ions to undergo intercalation, leading to secondary lithium ion batteries with high energy density [2].

In the recharging and discharging processes of secondary lithium ion batteries, lithium ions are intercalated into or released from the cavities of a crystalline WO_3 thin film, while electrons simultaneously enter or leave the cavities of the film; thus, both lithium ion transportation and electron transportation affect the recharging and discharging speed [3]. Although the performance of lithium ion transportation has been extensively studied, detailed research on the mechanism of electron conduction in crystalline WO_3 thin films for their application as an active cathode is still required. Furthermore, to improve the recharging and discharging speed, it is necessary to develop processes that can increase the electron conductivity of crystalline WO_3 thin films. Two main types of WO_3 crystalline structure, i.e., monoclinic WO_3 (*m*-WO_3) and hexagonal WO_3 (*h*-WO_3), are usually chosen for the active cathode [4,5]. *m*-WO_3 is preferable owing to its stability even at high temperatures (above 400 ^oC) [6].

In this chapter, electron conductivity property of *m*-WO_3 thin film was studied by measuring resistivity through the four-point probe method. The measurements were carried out in the temperature range of 243–443 K after annealing in N_2 or 5% O_2+95% N_2 ambient. The activation energy values (E_a) were derived, from which we supposed the oxygen vacancies' location in the bandgap of the WO_3 thin film. Moreover, annealing in N_2 ambient successfully decreased the resistivity, which was also supposed to be owing

to the increased number of oxygen vacancies in the WO_3 thin film.

3.2 Experiment Process

The experiment process can be divided into three main parts. The first part is device fabrication process which introduces the fabrication flow of the samples used in the resistivity measurement and a detailed introduction of the swirling flow spray coating method which is adopted for WO_3 nanoparticle fabrication. In the second part, resistivity measurement process is described. Besides, the four-point probe method and the E_a measurement method by changing measurement temperature are explained.

3.2.1 Device Fabrication Process

An aqueous dispersion of WO_3 nanoparticles of about 30 nm diameter was coated on a SiO_2 substrate of 400 nm thickness using swirling flow spray coating method, which was followed by annealing in air ambient at 450 ^oC for 30 min. The *m*-WO_3 thin film was formed with a thickness of about 150 nm, a porosity of about 35%, and a Brunauer–Emmett–Teller (BET) specific surface area of about 37 m^2/g. Fig. 3.1 (a) shows a transmission electron microscopy (TEM) image of the sample. Fig. 3.1 (b) shows a typical X-ray diffraction spectrum of an *m*-WO_3 thin-film sample. Fig. 3.1 (c) shows XPS data which also indicated WO_3 formation. The band gap was investigated by UV-Vis measurement and 2.78 eV was calculated as shown in Fig. 3.1 (d). The porosity of 35% was chosen for the experiment because, under this condition, a WO_3 film can be formed from WO_3 nanoparticles through a spraying method and the necking property of the nanoparticles can be obtained. When the porosity is less than 35%, a WO_3 coating cannot be formed. When the porosity is more than 35%, the resistivity of WO_3 increases. Then,

tungsten metal (W) was deposited by RF magnetron sputtering used for the electrodes in the four-point probe measurement. W electrode patterns were formed by lithography followed by the wet etching method with H_2O_2 solution. The formed sample was annealed at various temperatures in N_2 or 5% O_2+95% N_2 ambient.

(a)

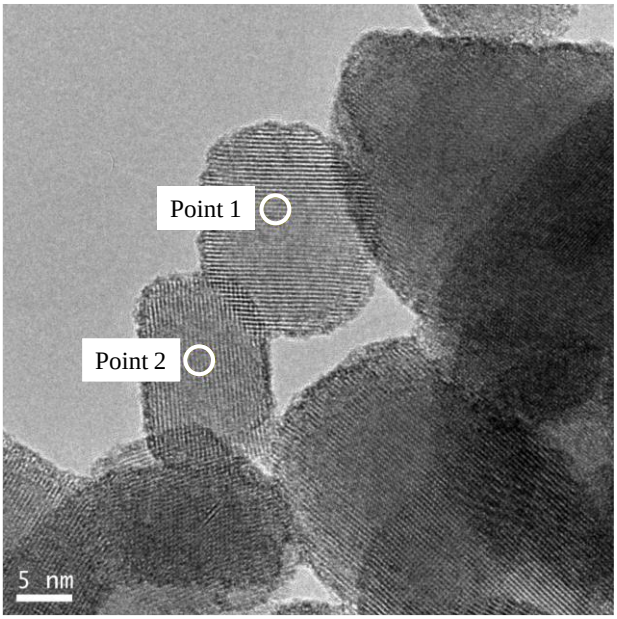

(b)

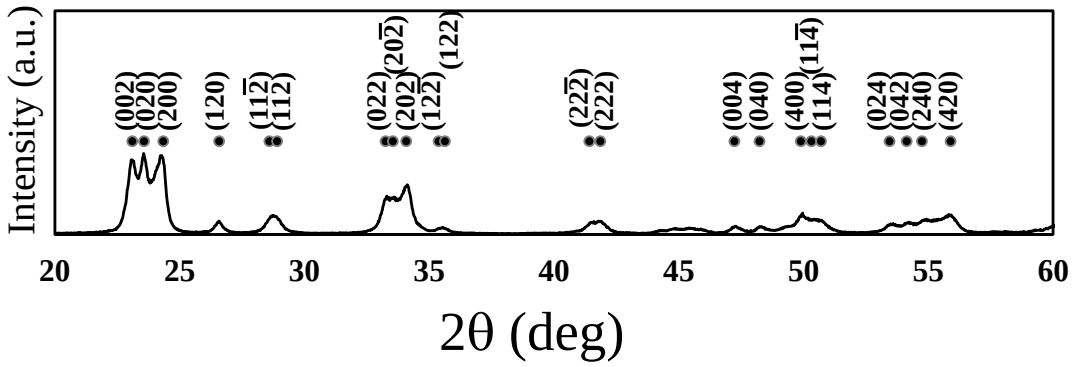

(c)

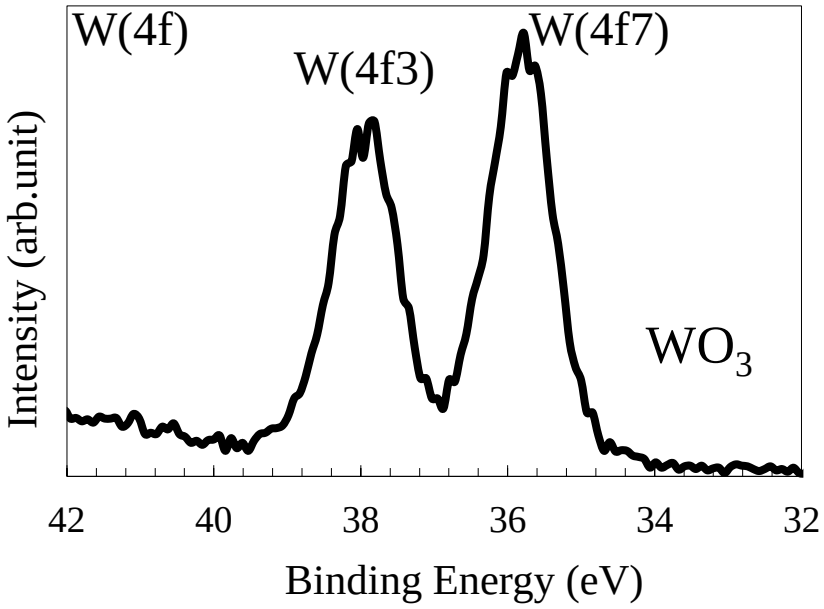

(d)

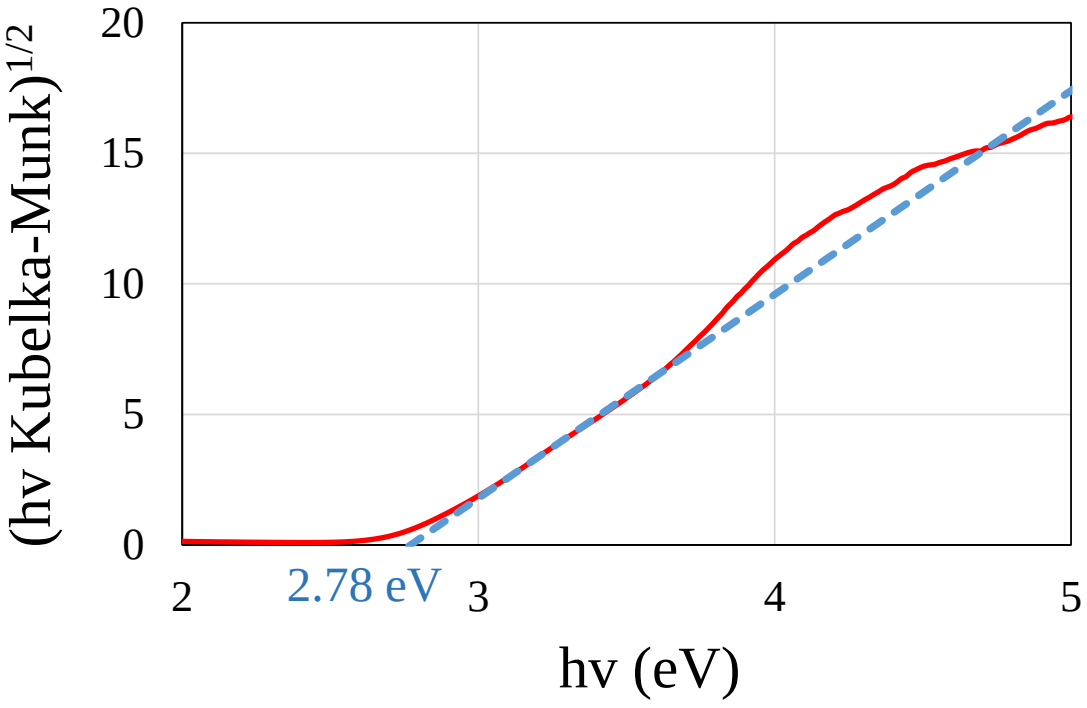

Fig. 3.1. (a) TEM image, (b) XRD spectrum, (c) XPS data and (d) UV-Vis data of *m*-WO_3

formed from WO_3 nanoparticles and adopted in this study.

3.2.1.1 Device fabrication flow

Fig. 3.2 shows the device fabrication process flow chart.

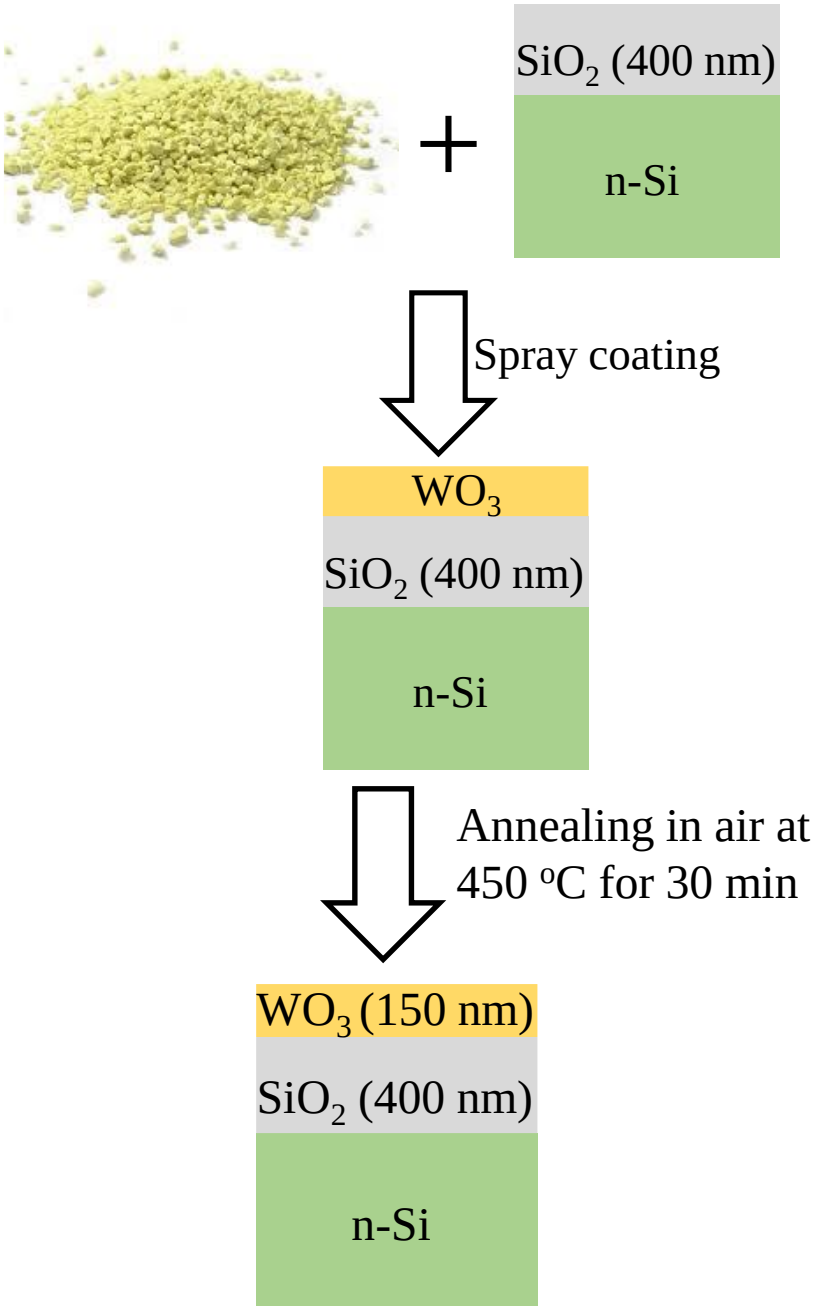

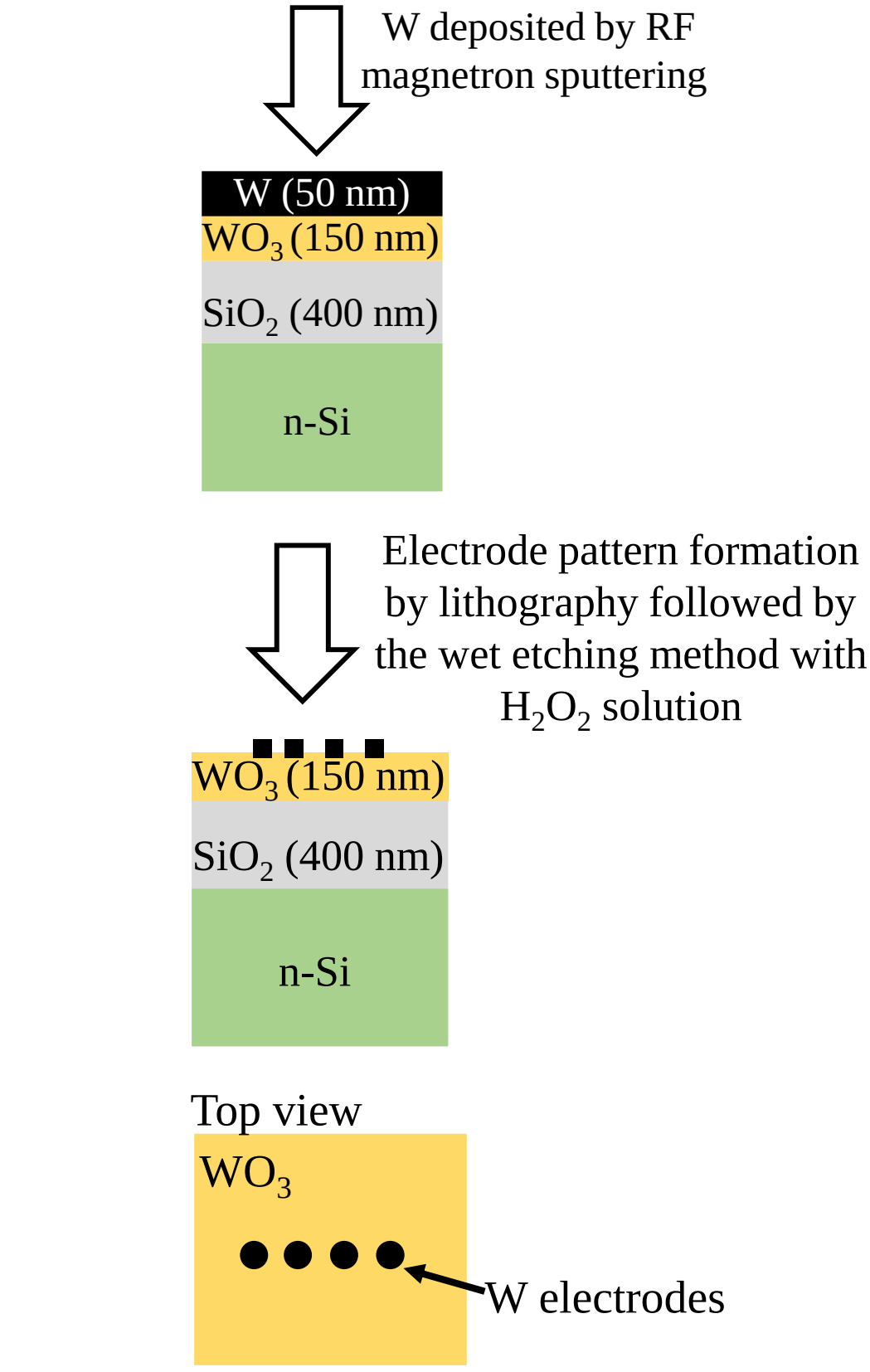

Fig. 3.2. Device fabrication process flow chart.

3.2.1.2 Spray coating method [7]

There are kinds of spray coating methods for film deposition, like ink coating method, roller coating method, squeegee print method, plasma spray coating method, and swirling flow spray coating method.

Among them, plasma spray coating which is a thermal spray coating process using an atmospheric pressure plasma, is used to produce a high quality coating of almost any metallic or ceramic on to a large range of materials. Plasma indicates gas which has been raised to such a high temperature that it ionizes and becomes electrically conductive. In plasma spray coating equipment as shown in Fig. 3.3, an arc is formed between two electrodes in a plasma forming gas, which is inert spraying medium, usually argon. As the plasma gas is heated by the arc, it expands and is accelerated with high particle velocities through a nozzle. Though it is a good method of making high density films, the control of the crystalline quality is difficult. Therefore, in this experiment, this method did not be examined to increase the packing density.

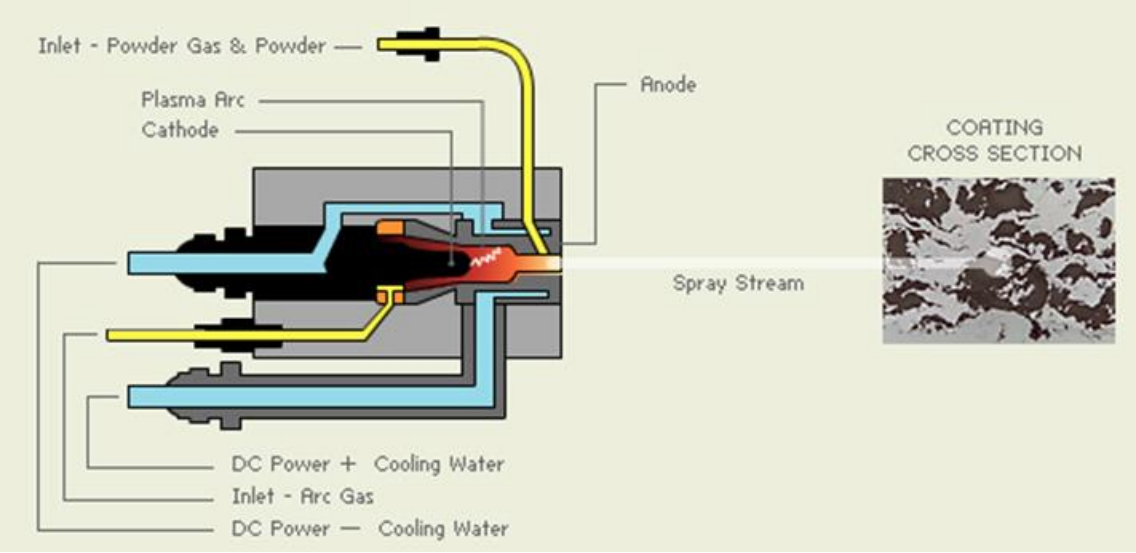

Fig. 3.3. Schematic diagram of plasma spray coating. [8]

In this experiment, swirling flow spray coating apparatus was used for WO_3 film deposition. The NVD (Nano Vapor Deposition) nozzle as shown in Fig. 3.4 (b) was adopted instead of the normal nozzle shown in Fig. 3.4 (a). Compared with the normal nozzle, NVD nozzle has swirl flow, which decreases attack angle and rebounding material. The NVD nozzle decreases material loss during deposition and makes the film denser.

(a)

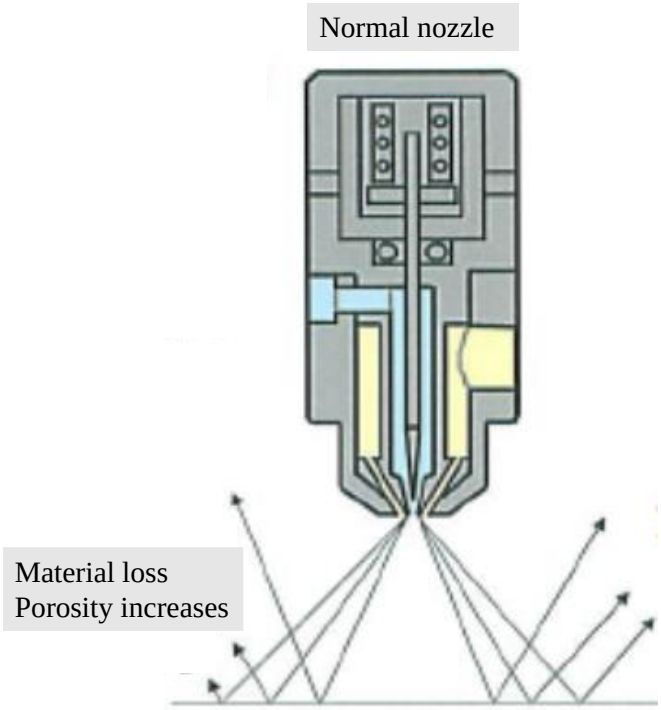

(b)

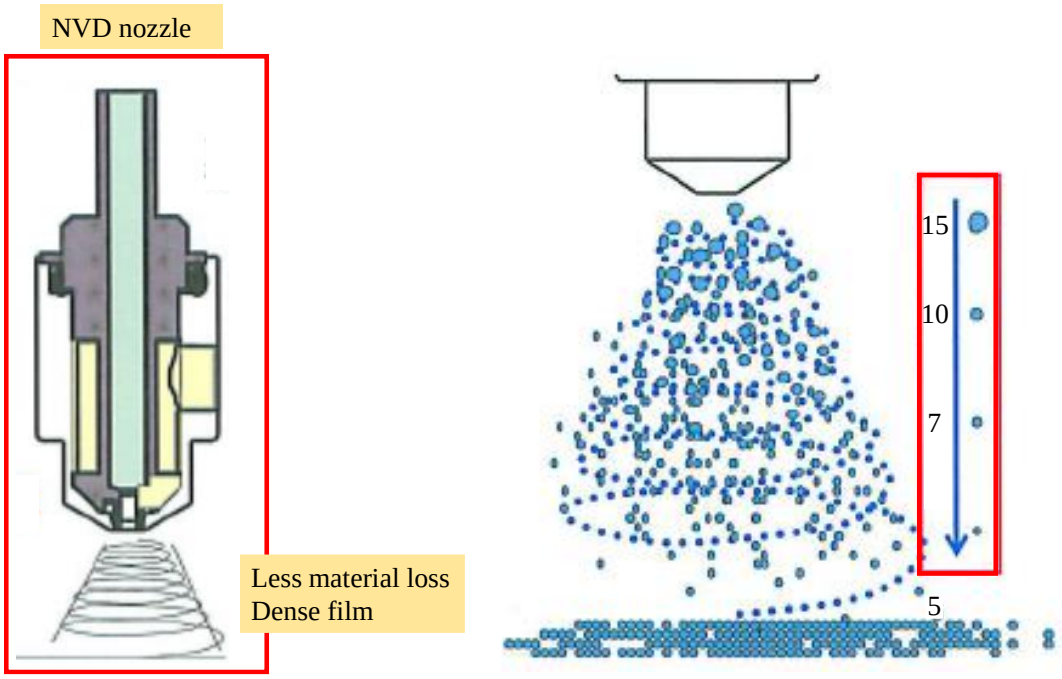

Fig. 3.4. Schematic diagram of spray coating with normal nozzle (a) and NVD nozzle (b).

Fig. 3.5 (a) and (b) show a comparison of SEM images of films fabricated respectively by squeegee print method and swirling flow spray coating method. Table 3.1 lists the porosity values of the films fabricated by the two methods. It is obviously observed that the swirling flow spray coating film is denser than squeegee print film.

(a) (b)

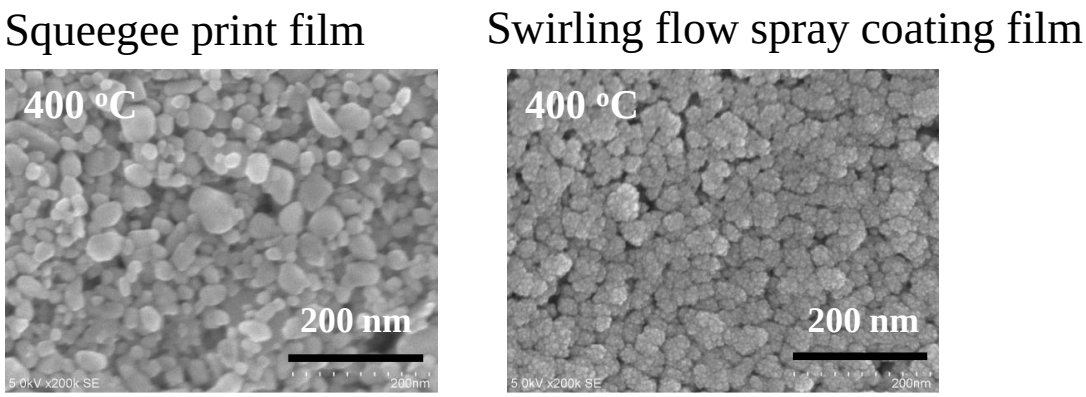

Fig. 3.5. SEM images of WO_3 film fabricated by (a) squeegee print, (b) swirling flow

spray coating.

Table 3.1. Porosity comparison of films fabricated by squeegee print method and swirling flow spray coating method.

		Film thickness	**weight**	**area**	volume	Weight density	Volume density	porosity
		[μm]	[g]	[cm2]	[cm3]	[g/cm3]	[vol%]	[vol%]
Spray coating	1	4.73	1.67E-02	7.60	3.60E-03	4.65	64.6	35.4
	2	6.75	2.30E-02	8.00	5.40E-03	4.26	59.1	40.9
	3	4.93	1.52E-02	6.80	3.35E-03	4.53	62.9	37.1
Squeegee print	1	3.9	4.10E-03	4.14	1.61E-03	2.54	35.3	64.7
	2	9.3	9.30E-03	4.14	3.85E-03	2.42	33.5	66.5
	3	15.4	1.55E-02	4.14	6.38E-03	2.43	33.8	66.2

3.2.1.3 Annealing Process

In this work, annealing treatment was done by using infrared lamp rapid thermal annealing equipment (QHC-P610CP developed by ULVAC-RIKO, Inc.). It is a high-speed heating and cooling system. It consists of an infrared lamp furnace with a quartz thermal treatment chamber and a temperature controller, as shown in Fig. 3.6. The ambience in furnace was vacuumed adequately prior to every annealing cycle and then annealing gas was provided with a flow rate of 1.0 L/min with preserving the furnace pressure at atmosphere pressure. Annealed samples were taken out from the chamber under 100 ^{o}C.

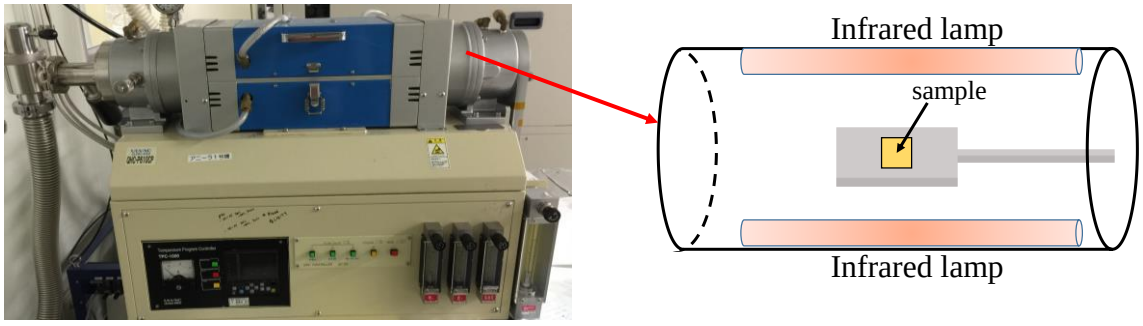

Fig. 3.6. Schematic diagram of infrared lamp rapid thermal annealing equipment.

3.2.2 Resistivity Measurement Process

The four-point probe method was used to measure the resistivity. First, the four-point probe method is introduced. Then, the detailed measurement process is described. Also, derivation method of E_a is explained.

3.2.2.1 The four-point probe method

The four-point probe method was proposed by Wenner in 1961 to measure the earth's resistivity. [9] Then Valdes adopted it for semiconductor wafer resistivity measurement in 1954. [10] The probes are arranged in-line with equal distance, as shown in Fig. 3.7.

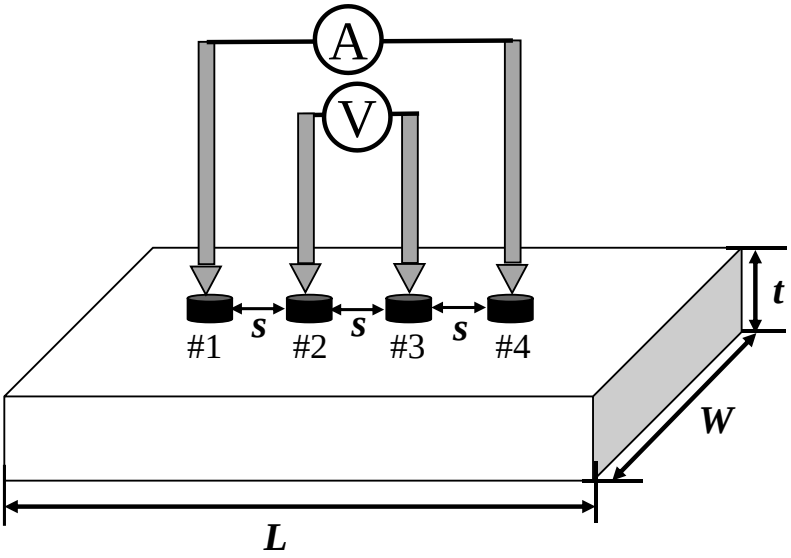

Fig. 3.7. Scheme of the four-point probe method.

The detailed derivation can be referred to [10]. The resistivity ρ can be calculated from Eq. (3.1), in which V is the voltage between #2 and #3, I is the current between #1 and #4, and t is the thickness of the WO_3 thin film.

$$\rho = 4.532t\frac{V}{I} \qquad (3.1)$$

3.2.2.2 Resistivity measurement process

Fig. 3.8 (a) introduces the measurement parameters of the four probes. The data in Fig. 3.8 (b) and (c) were used to calculate the sheet resistivity which is shown in Fig. 3.8 (d).

(a)

measurement

#1 V_1= -15~15V, I_1
#2 V_2, I=0
#3 V_3, I=0
#4 V_4=0V, I_4

(b)

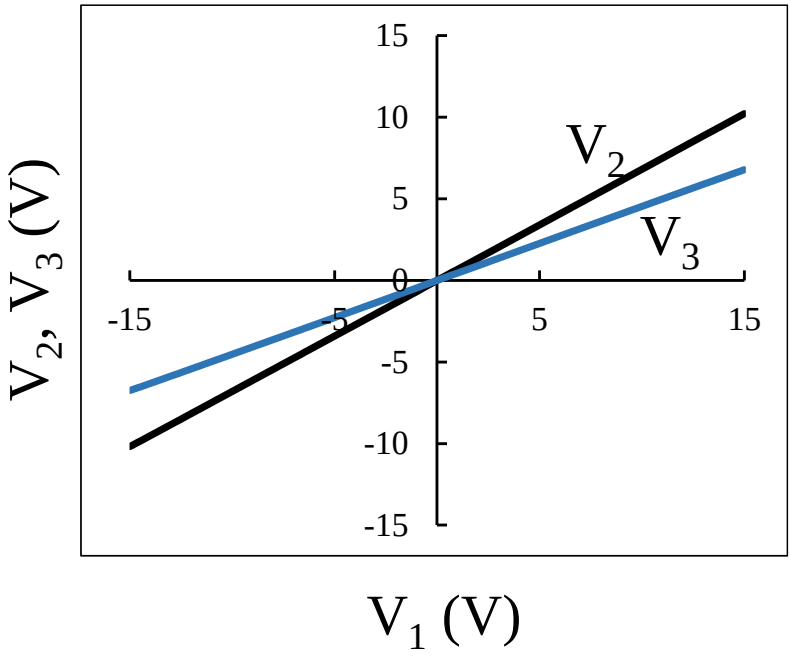

(c)

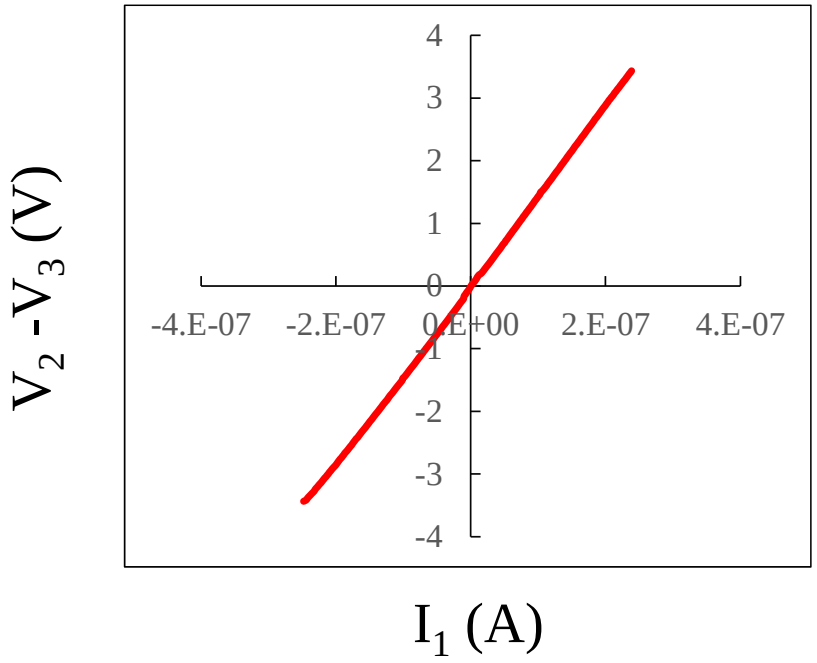

(d)

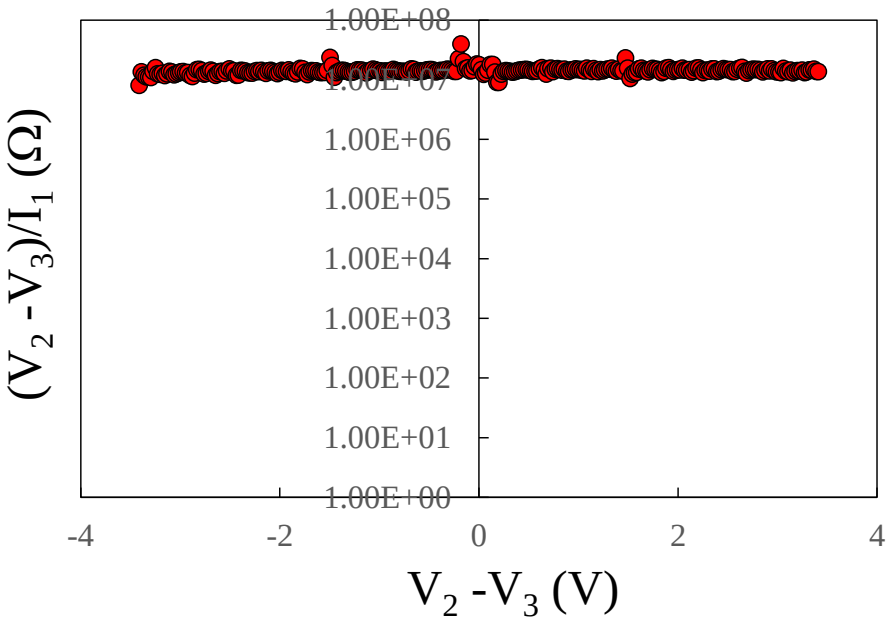

Fig. 3.8. A typical measurement data using the four-point probe method. (a) shows the measurement parameters, (b) shows the voltage values of #2 and #3 with applying a voltage sweep ranging from -15 V to +15 V between #1 and #4, (c) shows the voltage

difference between #2 and #3, and (d) shows the value of (V_2-V_3)/I.

3.2.2.3 Activation energy measurement method

E_a is a very important parameter which can indicate the donor level of semiconductor materials. E_a can be extracted using the Arrhenius equation (3.2). [11]

$$\rho = \rho_0 \exp(E_a / kT) \Rightarrow \ln \rho = \frac{E_a}{k} \cdot \frac{1}{T} + \ln \rho_0 \quad (3.2)$$

Here, ρ is the measured resistivity, ρ_0 is a pre-exponential factor, T is the measurement temperature, which is from 443 K to 243 K in this study, and k is the Boltzmann constant. E_a is proportional to the gradient of the schematic resistivity-temperature curve shown in Fig. 3.9.

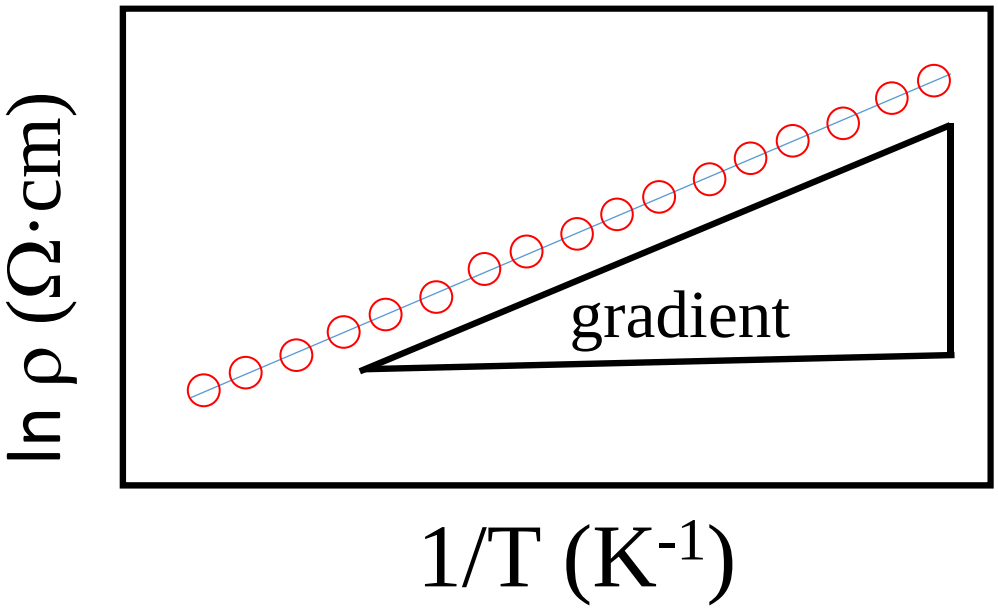

Fig. 3.9 Schematic resistivity-temperature curve.

3.3 Conductivity Property of Tungsten Trioxide Thin Film Depending on Different

Annealing Conditions

In this chapter, the electron conductivity of *m*-WO_3 thin films was studied through measuring the film resistivity after annealing under various conditions. We clarified the impact of a high-temperature N_2 annealing process in improving electron conductivity and also the oxygen vacancies' location in the bandgap of WO_3.

3.3.1 Conductivity Property of Tungsten Trioxide Thin Film Depending on Different Annealing Conditions

Fig. 3.10 shows the measured resistivity (plotted against 1000/T) for three samples, which were not subjected to annealing, annealed in N_2 ambient at 300 ^oC for 5 min, and annealed in N_2 ambient at 300 ^oC for 5 min followed by 5% O_2+95% N_2 ambient at 300 ^oC for 5 min. Although annealing in N_2 reduces the resistivity of the *m*-WO_3 film, subsequent annealing in 5% O_2+95% N_2 ambient results in the resistivity returning to its initial value.

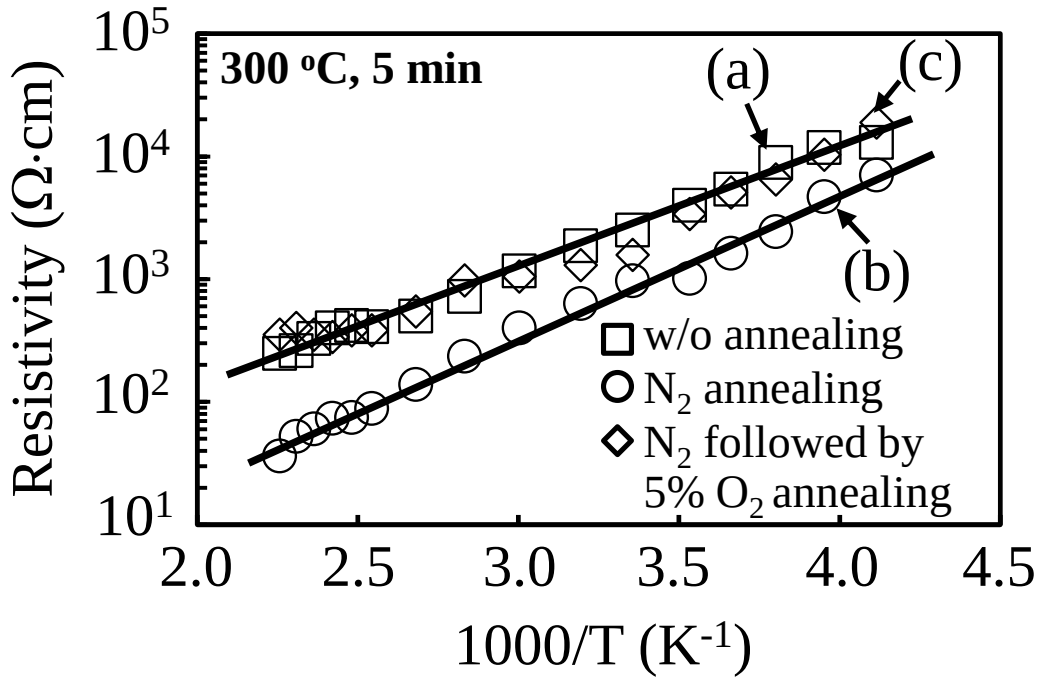

Fig. 3.10. Measured resistivity ρ versus 1000/T for samples annealed in different ambients: no annealing (a), annealed in N_2 ambient at 300 ^oC for 5 min (b), annealed in N_2 ambient at 300 ^oC for 5 min followed by 5% O_2+95% N_2 ambient at 300 ^oC for 5 min.

The changes in the resistivity after annealing in N_2 or 5% O_2+95% N_2 ambient exhibited in Fig. 3.10 can be explained by oxygen vacancy generation and annihilation in a tungsten oxide thin film. After annealing at 300 ^oC in N_2 ambient, oxygen vacancies, which create trap levels in the bandgap for activated electrons to mobile, were generated, leading to a decrease in the resistivity. After annealing at 300 ^oC in 5% O_2+95% N_2 ambient, the oxygen vacancies were annihilated, leading to a decrease in the number of carrier trap sites and a simultaneous decrease in the number of carriers taking part in the conduction. Therefore, the resistivity increased to almost the same value as before annealing.

Fig. 3.11 (a) shows a thermogravimetric analysis data of the WO_3 sample. The measurement was carried out in N_2 ambient with increasing the temperature from room temperature to 100 ^oC in a rate of 5 ^oC/min. It was observed that as temperature increased, the weight of the sample decreased, which is considered to be due to the loss of oxygen atom. Besides, Fig. 3.11 (b) shows a XPS data of W (4f) of the three types of WO_3 samples which are without N_2 annealing, with N_2 annealing at 300 ^oC and 700 ^oC. It clearly shows that N_2 annealing at 700 ^oC made the peaks of W (4f) shift, which indicates an increase of oxygen vacancies in WO_3.

(a)

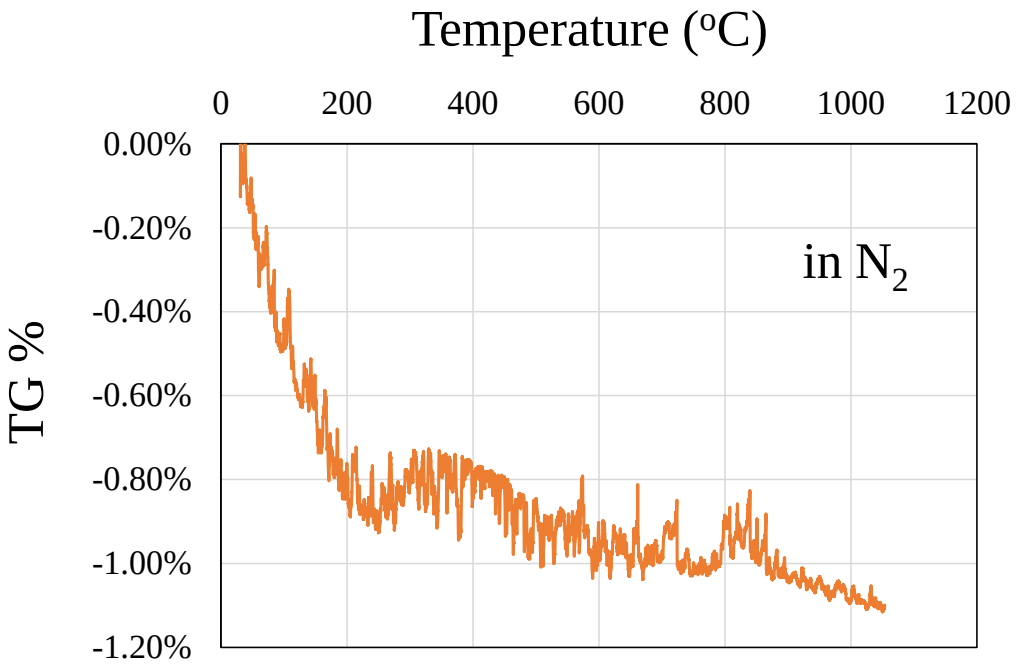

(b)

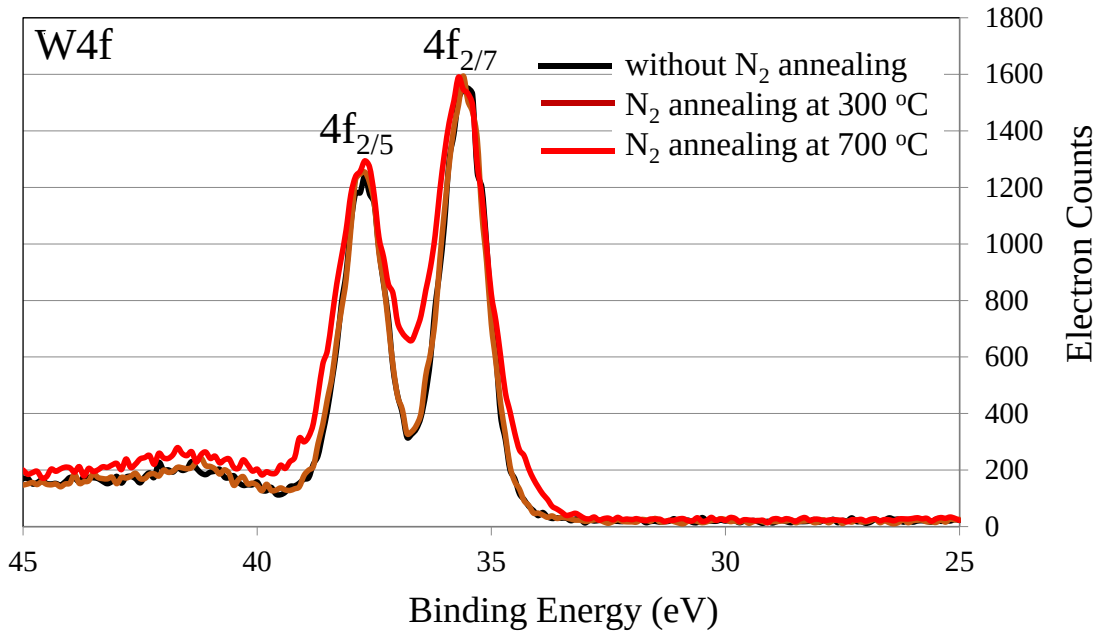

Fig. 3.11. (a) a thermogravimetric analysis data of the WO_3 sample in N_2 ambient, and (b) a XPS data of W (4f) of the three types of WO_3 samples which are without N_2 annealing, with N_2 annealing at 300 °C and 700 °C.

Fig. 3.12 shows the resistivity ρ plotted against 1000/T for the samples after annealing in N_2 at temperatures from 300 ^oC to 750 ^oC for 5 min. For the samples annealed at temperatures from 300 ^oC to 500 ^oC, the gradients of the curves were almost the same as that for the sample without annealing. On the other hand, for the samples annealed at temperatures from 600 ^oC to 750 ^oC, the curves could be divided into two parts with different gradients. The first part is in the temperature range from 443 K to 393 K, which has almost the same gradient as that for the sample without annealing. The other part is in the temperature range from 373 K to 243 K, which has a smaller gradient. The detailed discussion about the different gradients of the curves will be done in Chapter 4.

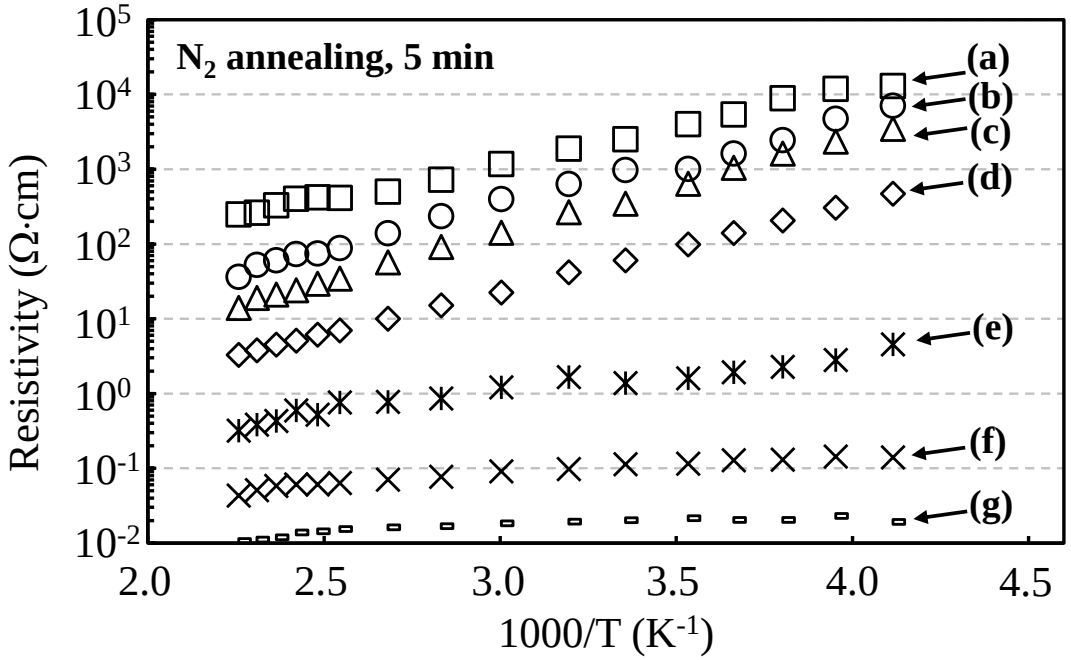

Fig. 3.12. Measured resistivity ρ versus 1000/T after annealing in N_2 for 5 min at different temperatures: no annealing (a), annealed at 300 ^oC (b), 400 ^oC (c), 500 ^oC (d), 600 ^oC (e), 700 ^oC (f), 750 ^oC (g).

3.3.2 Derivation of E_a values

E_a values were derived for the three samples and are shown in Table 3.2, where E_a can be interpreted in the form of a trap depth in the bandgap in this study. It was observed that all the E_a values of the three curves shown in Fig. 3.10 were approximately 0.2 eV, indicating that oxygen vacancies stably exist at approximately 0.2 eV below the bottom of the conduction band as shown in Fig. 3.13.

Table 3.2. Derived values of E_a for different annealing conditions.

	w/o annealing	300 °C annealing in N_2 ambient	300 °C annealing in 5% O_2 ambient
E_a (eV)	0.19	0.23	0.18

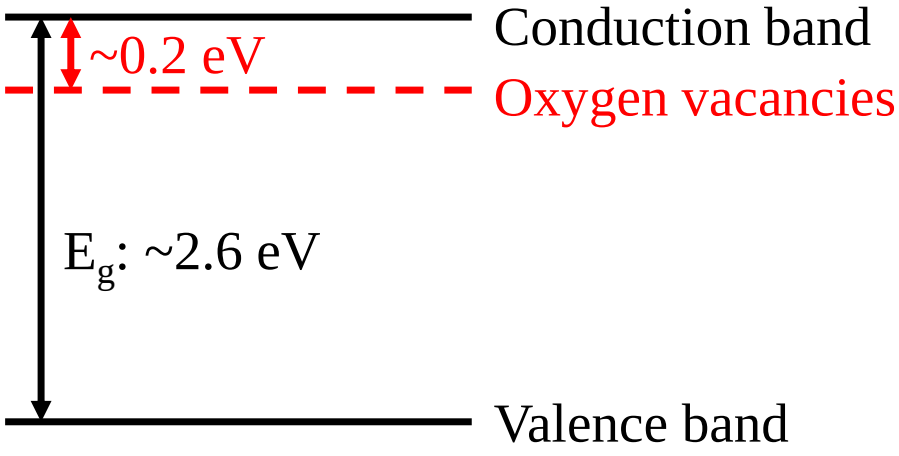

Fig. 3.13. Suggestion for oxygen vacancies' location in the bandgap of WO_3 thin film.

3.4 Conclusion

In this chapter, we focused on improving electron conductivity of m-WO_3 thin film.

Fabrication methods of devices used for resistivity measurement of WO_3 thin film was introduced. Especially, a NVD swirling flow spray coating was introduced in detail since in this work, this method made a denser WO_3 thin film compared with other print methods.

The four-point probe method was introduced and used for the resistivity measurement. Activation energy derivation method was also explained.

We successfully improved the electron conduction property of WO_3 powder thin films fabricated from nanoparticles. Resistivity measurements were carried out after annealing in N_2 or 5% O_2+95% N_2 ambient. Annealing in N_2 ambient decreases the resistivity. Subsequent annealing in 5% O_2+95% N_2 ambient results in the resistivity returning to its initial value. This was explained by derivation of activation energy, suggesting that oxygen vacancies stably exist at approximately 0.2 eV below the bottom of the conduction band. Moreover, compared with low-temperature annealing in N_2, high-temperature (from 600 ^oC to 750 ^oC) annealing in N_2 had a greater effect on decreasing the resistivity of m-WO3 thin films.

Reference List

[1] K. Huang, Q. Zhang, ``Rechargeable lithium battery based on a single hexagonal tungsten trioxide nanowire," *Nano Energy*, vol. 1, pp. 172-175, 2012.

[2] M. F. Parkinson, J. K. Ko, A. Halajko, S. Sanghvi, G. G. Amatucci, ``Effect of Vertically Structured Porosity on Electrochemical Performance of FeF_2 Films for Lithium Batteries," *Electrochim. Acta*, vol. 125, pp. 71-82, 2014.

[3] S. H. Lee, H. M. Cheong, C. Edwin Tracy, A. Mascarenhas, R. Pitts, G. Jorgensen, S. K. Deb, ``Influence of microstructure on the chemical diffusion of lithium ions in amorphous lithiated tungsten oxide films," *Electrochim. Acta*, vol. 46, pp. 3415-3419, 2001.

[4] N. Kumagai, M. Abe, N. Kumagai, K. Tanno, J. P. Pereira-Ramos, ``Kinetics of electrochemical insertion of lithium into WO," *Solid State Ionics*, vol. 70-71, pp. 451-457, 1994.

[5] A. Yu, N. Kumagai, Z. Liu, J. Y. Lee, ``Electrochemical lithium intercalation into WO_3 and lithium tungstates $Li_xWO_{3+x/2}$ of various structures," *J. Solid State Electrochem.* vol. 2, pp. 394-400, 1998.

[6] A. Al Mohammad, M. Gillet, ``Phase transformations in WO_3 thin films during annealing," *Thin Solid Films*, vol. 408, pp. 302-309, 2002.

[7] Fabricated by Kyushu Institute of Technology

[8] http://www.tstcoatings.com/plasma_spray.html

[9] D. K. Schroder, *Semiconductor Material and Device Characterization.* John Wiley & Sons, 2006.

[10] D. K. Schroder, *Semiconductor Material and Device Characterization*. New York: John Wiley &Sons, 2006.

[11] S. Ambily, C. S. Menon, ``Determination of the thermal activation energy and optical band gap of cobalt phthalocyanine thin films," *Mater. Lett.* vol. 34, pp. 124-127, 1998.

Chapter 4 Conduction Mechanism Analysis of Tungsten Trioxide Thin Film

4.1 Introduction

4.2 Introduction of Typical Conduction Mechanisms of Semiconductor Materials

4.3 Resistivity Fitting by a Mixture of Band Conduction and Nearest-Neighboring Hopping Conduction Mechanisms

4.4 Conclusion

Reference List

4.1 Introduction

Electron transport in amorphous or doped semiconductors has been investigated for decades. [1-4] In this process, many transport models have been approached and discussed. [5-7] Impurity conduction is one of them, which has been observed in many semiconductors at low temperatures. [8] It is shown that the conductivity at low temperatures has the following characteristics:

(a) It is the form as shown in Eq. (4.3), where the activation energy ε is usually an order of magnitude less than that required to free an electron from a donor or a hole from an acceptor E_a as described in Eq. (4.2).

(b) ε depends strongly on the concentration of donors or acceptors.

The mechanism is illustrated in Fig. 4.1. The electrons are thought to tunnel from one center to the next. Fig. 4.2 shows some experimental results on the resistivity of doped p-type germanium.

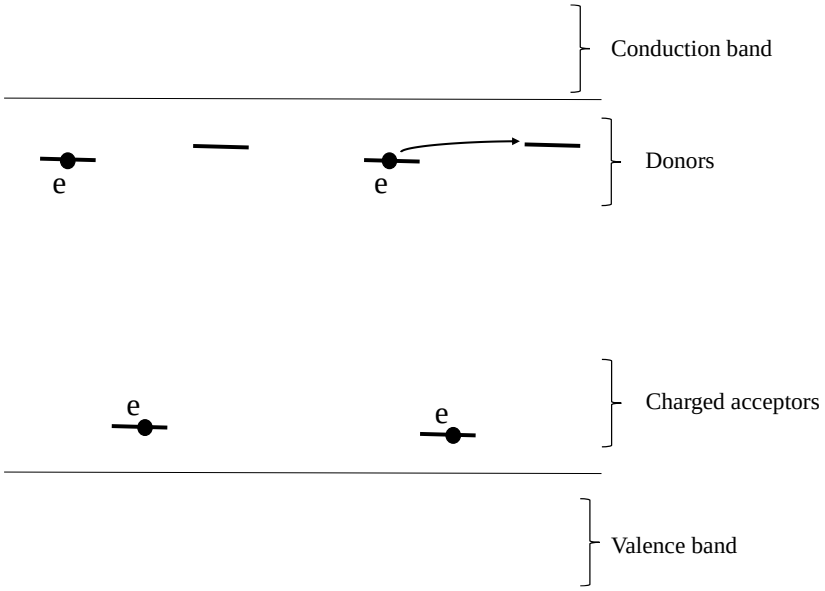

Fig. 4.1. Energy levels for a doped n-type semiconductor; the rate-determining process is the hopping of an electron from an occupied center. [1]

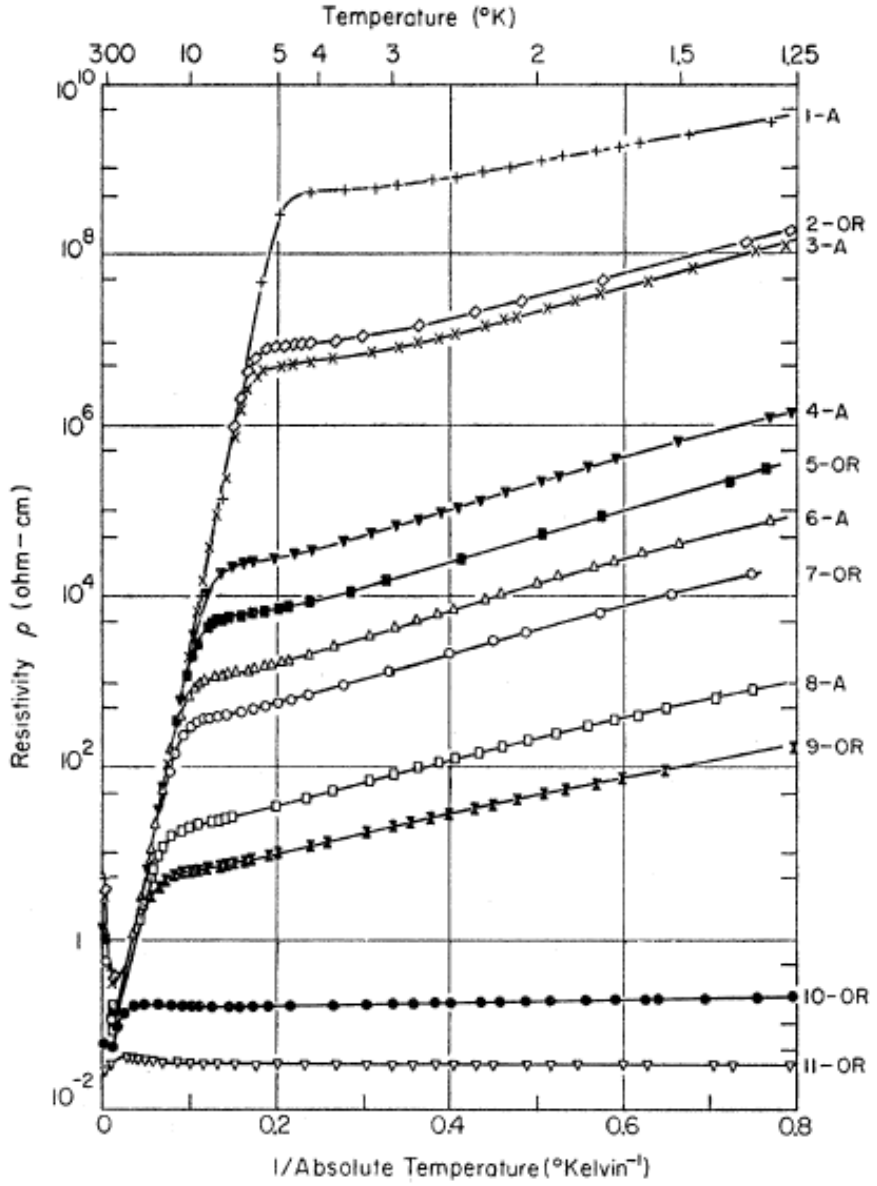

Fig. 4.2. Resistivity ρ of p-type germanium with compensation K(=N_D/N_A)=0.4 as a function of 1/T. [9]

In this chapter, fitting results obtained from the resistivity shown in Fig. 3.12 of chapter 3 are used to propose the simultaneous existence of two types of electron conduction mechanism, band conduction and nearest-neighbor hopping (NNH) conduction, contributing to electron conduction in WO_3 thin films.

4.2 Introduction of Typical Conduction Mechanisms of Semiconductor Materials

Normally, for semiconductor materials, band conduction is the main type of electron conduction mechanism as shown in Fig. 4.3. The temperature dependence of resistivity in band electron conduction is given by Eq. (4.1).

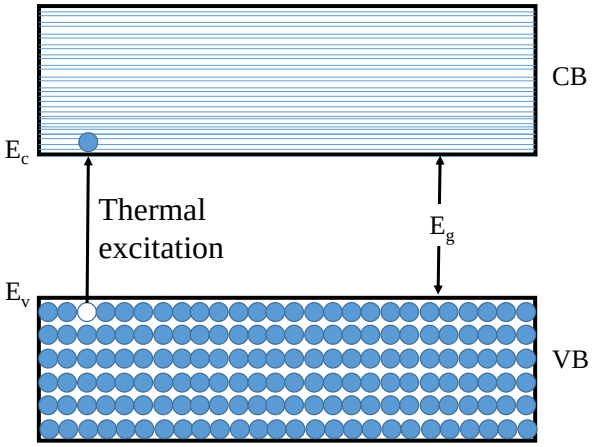

Fig. 4.3 Energy band diagram of a semiconductor. CB is the conduction band and VB is the valence band. At 0 K, the VB is filled with all the valence electrons.

$$\rho = A\exp(E_g / 2kT) \tag{4.1}$$

Moreover, in doped semiconductors, band conduction and hopping conduction both play important roles in the electronic conduction. [3] Fig. 4.4 (a) shows the band conduction mechanism when the semiconductor has donor levels. Besides, there are two main types of electron hopping conduction mechanism for doped semiconductors, that is, nearest-neighbor hopping (NNH) conduction and variable-range hopping (VRH) conduction [4,7,10-11], as depicted in Figs. 4.4 (b) and (c). In NNH conduction, the

phonon-assisted hopping happens between the nearest neighbor impurity sites. For VRH conduction, in a disordered insulator, N. Mott first pointed out that at low temperature the most frequent electron hopping among localized sites would not be to the nearest neighbor. [5] Mott's VRH gives the relation between electron resistivity ρ and temperature T, as shown in Eq. (4.4). [5] There are some materials which have been demonstrated to be consistent with the law of Eq. (4.4), such as amorphous germanium in the temperature range 60 K≤T≤ 300 K, amorphous silicon, carbon, and in vanadium oxide. [12]

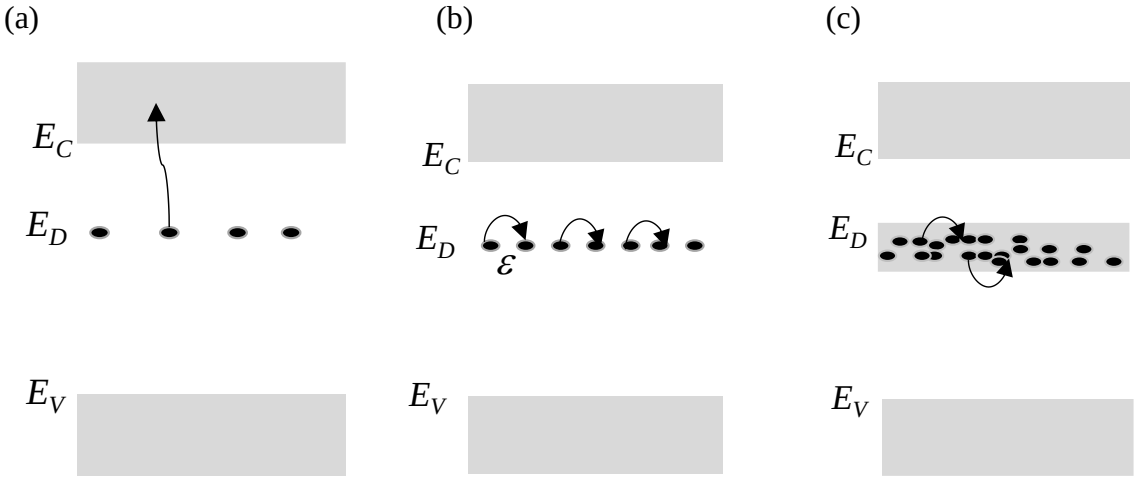

Fig. 4.4. Schematic representations of three types of conduction mechanism of semiconductor materials: (a) band conduction mechanism, (b) NNH conduction mechanism, (c) VRH conduction mechanism.

$$\rho(T) \propto \exp\left(\frac{E_a}{kT}\right)$$
$$E_a = E_C - E_D \qquad (4.2)$$

$$\rho(T) \propto \exp\left(\frac{\varepsilon}{kT}\right) \qquad (4.3)$$

$$\rho(T) \propto \exp\left(\frac{1}{T}\right)^{\frac{1}{4}} \qquad (4.4)$$

4.3 Resistivity Fitting by a Mixture of Band Conduction and Nearest-Neighboring Hopping Conduction Mechanisms

As shown in Fig. 3.12 of chapter 3, when the annealing was carried out below 600 ^{o}C, the resistivity-temperature curves gave almost the same E_a values as that of the sample without annealing, indicating that, in this situation, the band conduction is still the dominant type of electron conduction. However, when the annealing was carried out at 600 ^{o}C or above, two different activation energies, which were dependent on the measurement temperature *T*, were observed. This is because at high measurement temperatures, the thermal activation energy is sufficiently large for electrons to jump from the traps to the conduction band. On the other hand, at low measurement temperatures, the thermal activation energy is insufficient for electrons to jump to the conduction band. Thus, in the latter case, electrons move between nearest- neighbor traps. Thus, NNH conduction is assumed to be dominant. VRH conduction did not occur in this experiment since VRH conduction satisfies the relation shown in Eq. (4.3) and, we found that the resistivity shown in Fig. 3.12 was related to T^{-1} not to $T^{-1/4}$.

Resistivity fitting using a mixture of band conduction and NNH conduction was carried

out using Eq. (4.5).

$$\rho(T)=\left\{\left[\frac{1}{qN_d\mu_b}\exp\left(\frac{qE_a}{kT}\right)\right]^{-1}+\left[\frac{1}{qN_o\mu_h}\exp\left(\frac{q\varepsilon}{kT}\right)\right]^{-1}\right\}^{-1} \tag{4.5}$$

Here, N_d and N_o are the carrier densities of donors involved in band conduction and NNH conduction, respectively, μ_b and μ_h are the conductivity mobilities of carriers involved in band conduction and NNH conduction, respectively, E_a is the energy difference from the donor level to the bottom of the conduction band, and ε is the average activation energy of electrons hopping between neighboring carrier trap sites at the donor level. The experimental data obtained from annealing in N_2 ambient at 700 ^oC and 750 ^oC were used for the fitting. The fitting results are shown in Fig. 4.5 and the values of the fitting parameters are summarized in Table 4.1. As shown in Table 4.1, compared with annealing in N_2 ambient at 700 ^oC, annealing in N_2 ambient at 750 ^oC induced more oxygen vacancies, which caused ε to decrease and N_o to increase. Moreover, some carriers involved in band conduction jumped to oxygen vacancies at the donor level and took part in NNH conduction, thus decreasing N_d. Along with the increase in N_o and decrease in N_d decreasing, μ_h decreased and μ_b increased. In this work, fitting result gives a qualitative evaluation of how many oxygen vacancies there are. Since nanoparticle film of WO3 has a relatively high porosity, it is difficult for quantitative evaluation.

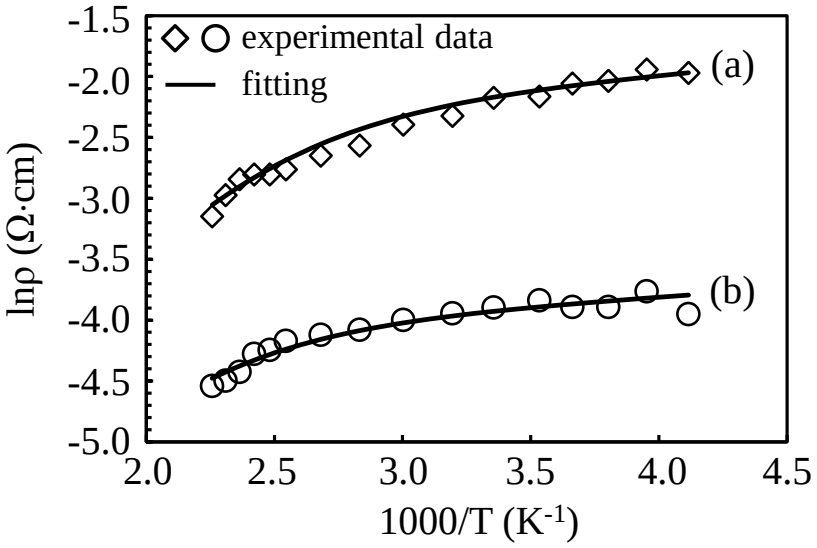

Fig. 4.5. Results of resistivity fitting assuming a mixture of band conduction and NNH conduction. Resistivity fitting of sample annealed in N_2 ambient for 5 min at 700 ^oC (a), and 750 ^oC (b). Circles and rhombi represent the experimental data and black lines represent the results of fitting.

Table 4.1. Values of parameters used for resistivity fitting.

	N_d (cm^{-3})	μ_b (cm^2/Vs)	E_a (eV)	N_o (cm^{-3})	μ_h (cm^2/Vs)	ε (eV)
700 ^{o}C annealing in N_2 ambient	7.2×10^{22}	0.4	0.23	5.0×10^{20}	0.19	0.016
750 ^{o}C annealing in N_2 ambient	7.0×10^{22}	1.13	0.23	7.0×10^{21}	0.07	0.012

4.4 Conclusion

The electron transport mechanism of *m*-WO_3 thin films was studied by fitting the resistivity obtained after N_2 annealing at different temperatures by assuming two types of electron conduction mechanism: band conduction and NNH conduction. It is proposed

for the first time that two conduction mechanisms simultaneously exist in the electron conduction of *m*-WO_3 thin films. Moreover, after high-temperature annealing in N_2, the NNH conduction mechanism becomes dominant owing to the increased number of oxygen vacancies.

Reference List

[1] N. F. Mott and E. A. Davis, *Electronic Processes in Non-Crystalline Materials*. Oxford University Press, 2012.

[2] A. K. Jonscher, ``Electronic conduction in amorphous semiconductors," *Journal of Vacuum Science and Technology*, vol. 8, no. 1, pp. 135-144, 1971.

[3] A. Kurobe and H. Kamimura, ``Correlation effects on variable range hopping conduction and the magnetoresistance," *Journal of the Physical Society of Japan*, vol. 51, no. 6, pp. 1904-1913, 1982.

[4] K. Nomura, T. Kamiya, H. Ohta, K. Ueda, M. Hirano and H. Hosono, ``Carrier transport in transparent oxide semiconductor with intrinsic structural randomness probed using single-crystalline $InGaO_3(ZnO)_5$ films," *Applied Physics Letters*, vol. 85, no. 11, pp. 1993-1995, 2004.

[5] N. F. Mott, *Conduction in Non-Crystalline Materials*. Oxford University Press, 1993.

[6] B. I. Shklovskii and A. L. Efros, ``Electronic properties of doped semiconductors," *Moscow Izdatel Nauka*, vol. 1, 1979.

[7] D. Yu, C. Wang, B. L. Wehrenberg and P. Guyot-Sionnest, ``Variable range hopping conduction in semiconductor nanocrystal solids," *Physical review letters*, vol. 92, no. 21, pp. 216802-1-4, 2004.

[8] C. S. Hung, ``Theory of resistivity and Hall effect at very low temperatures," *Physical Review*, vol. 79, no. 4, pp. 727-728, 1950.

[9] H. Fritzsche and M. Cuevas, ``Impurity conduction in transmutation-doped p-type germanium," *Physical Review*, vol. 119, no. 4, pp. 1238-1245, 1960.

[10] E. M. Conwell, ``Impurity band conduction in germanium and silicon," *Physical Review*, vol. 103, no. 1, pp. 51-61, 1956.

[11] T. Sato and K. Ohashi, ``Transport of heavily boron-doped synthetic semiconductor diamond in the hopping regime," *Physical Review B*, vol. 61, no. 19, pp. 12970-12976, 2000.

[12] V. Ambegaokar, B. I. Halperin and J. S. Langer, ``Hopping conductivity in disordered systems," *Physical review B*, vol. 4, no. 8, pp. 2612-2620, 1971.

Chapter 5 Charge/Discharge Property of Lithium Ion Batteries with Tungsten Trioxide Thin Film Electrode

5.1 Introduction

5.2 Experiment Process

5.2.1 WO_3 Electrode Fabrication

5.2.2 LIBs Assembly Process

5.3 Measurement Method

5.3.1 Charge/Discharge with Constant Current

5.3.2 Frequency Response Analyzer (FRA)

5.3.3 Cyclic Voltammetry

5.3.4 Charge Rate

5.4 Charge/Discharge Performance

5.5 Investigation of Crystalline Structures Depending on Different Annealing Conditions

5.6 Conclusion

Reference List

5.1 Introduction

LIBs have been considered to be the most advanced means of energy storage in the near future [1-4]. The charge/discharge time is becoming increasingly important in evaluating the performance of batteries for their use in electric vehicles and other applications [4]. Although much effort has been made to study Li ion transportation to increase the charge/discharge speed [4-7], there has been little research on electron conduction to our knowledge. However, electrons and lithium ions both play important roles in determining the charge/discharge speed [8].

In this chapter, we aim to demonstrate that the electron conduction of electrodes greatly impacts the charge/discharge performance of LIBs by evaluating the performance of LIBs with WO_3 electrodes having different conductivities. We used the WO_3 electrode as the positive electrode with Li metal as the negative electrode to investigate the charge/discharge characteristics.

5.2 Experiment Process

The experiment process can be divided into two main parts. The first part is WO_3 electrode fabrication process which introduces the fabrication flow of the samples used in the LIBs' assemble. In the second part, LIB's property measurement methods are described.

5.2.1 WO_3 Electrode Fabrication

WO_3 electrodes were prepared by the following process. m-WO_3 nanopowder (diameter: 20–30 nm), a transmission electron microscopy (TEM) image of which is shown in Fig. 5.1, was dispersed with an amount of 20 wt.% in EC-100FTP. EC-100FTP

is an ETHOCEL (Ethylcellulose) solvant used as a binder to form a powder past produced by Nisshin Kasei Co. Ltd. [9] Then a rotating mixer (1500 rpm, 10 min) was used to obtain a uniform paste of m-WO_3 powder. The paste was coated on a Ti film (thickness: ~20 μm) to a thickness of 50 μm. Then the paste was annealed in air ambient at 450 ^oC for 1 h to remove EC solvent and induce the necking of the m-WO_3 nanoparticles. After the annealing, the thickness of the WO_3 paste was ~5 μm. The paste was cut into circular patterned electrodes (diameter: ~16 mm), which were annealed at 300 or 700 ^oC in N_2 ambient for 5 min. A sample not subjected to N_2 annealing was also prepared. As shown in Figs. 5.2 (a), (b), and (c), the color of the electrodes changed from gray to blue after annealing at 300 ^oC and dark blue after annealing at 700 ^oC. This color change can be attributed to the generation of oxygen vacancies in the prepared WO_3 electrodes, and the resistivity decreased as the number of oxygen vacancies increased [10]. Fig. 5.3 shows the fabrication process.

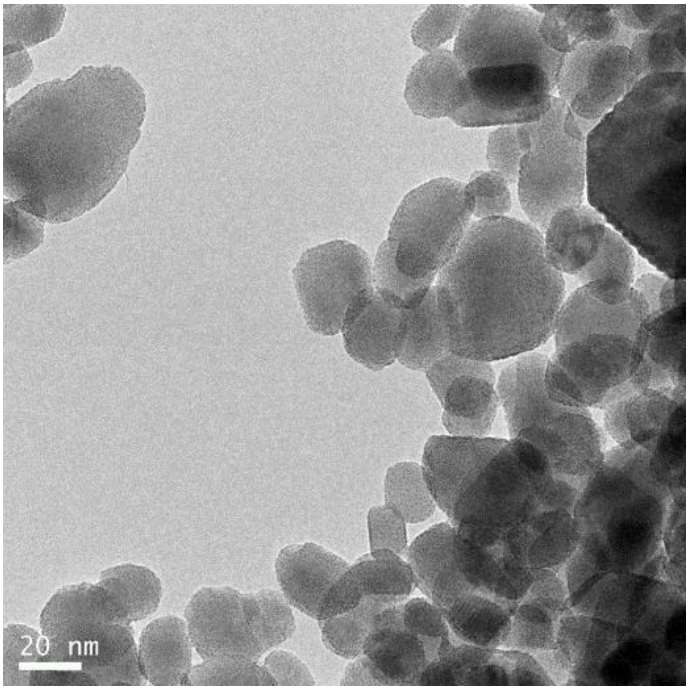

Fig. 5.1. TEM image of m-WO_3 powder used in the experiment.

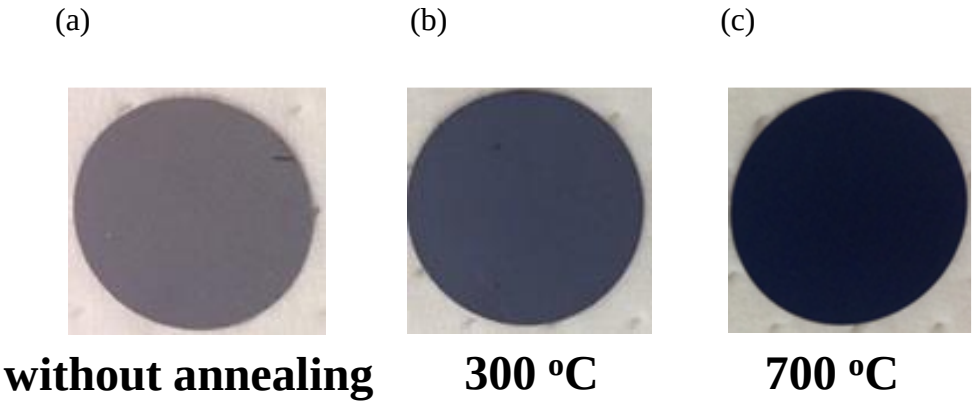

Fig. 5.2. Photographs of electrodes not subjected to annealing treatment (a), after annealing in N_2 ambient at 300 °C for 5 min (b), and after annealing in N_2 ambient at 700 °C for 5 min (c).

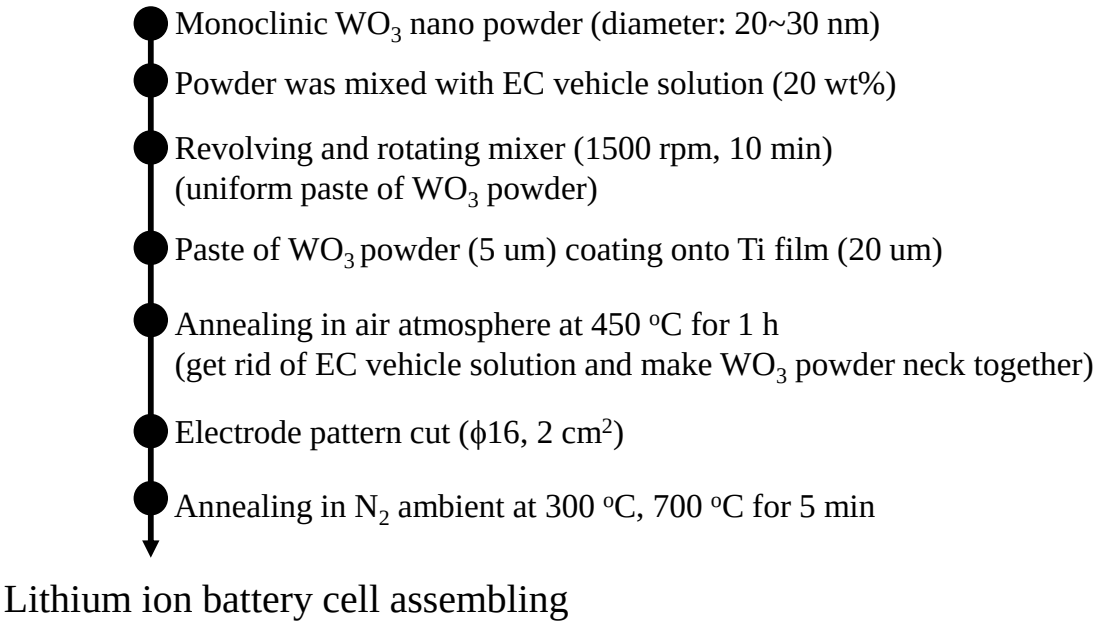

Fig. 5.3 Fabrication process of WO_3 electrodes

5.2.2 LIBs Assembly Process

LIBs were assembled that included the prepared electrodes with a Li metal counter

electrode separated by a separator and an electrolyte consisting of 1 M $LiPF_6$ in an EC/diethyl carbonate (DEC) (1:1) mixture. The assembly was carried out in Ar ambient in a dry glove box. Fig. 5.4 (a) and (b) show the fabrication and structure of LIBs used in this work.

(a)

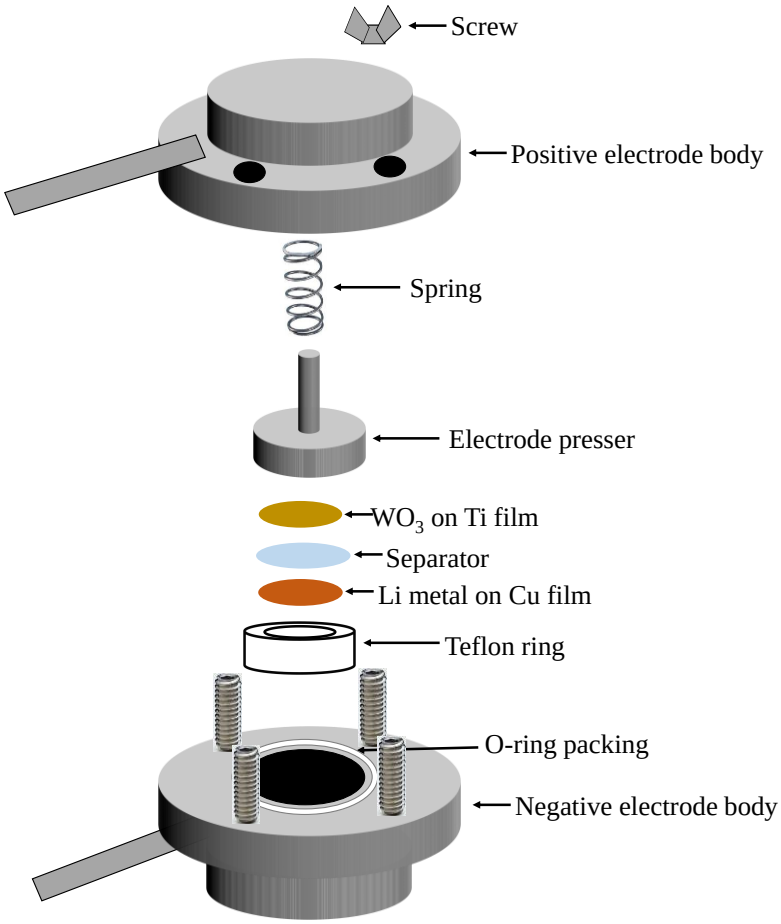

(b)

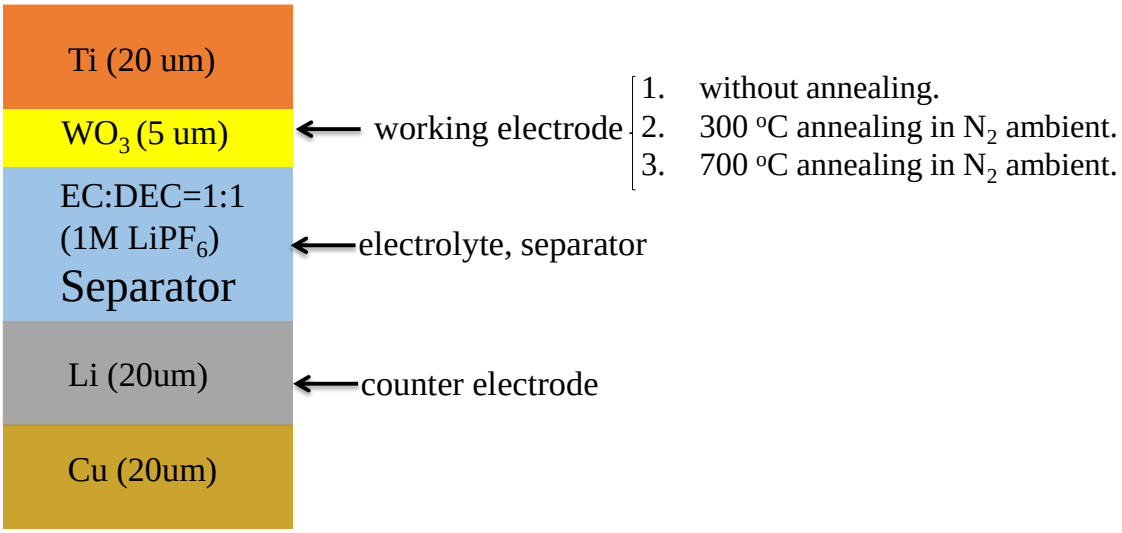

Fig. 5.4 Fabrication (a) and structure (b) of LIBs used in this study.

5.3 Measurement Method

Measurement methods of electrode performance are introduced. The electrode performance was evaluated by measuring the charge-discharge properties, performing cyclic voltammetry, frequency response analysis (FRA), and charge capacity measurement at different charge rates.

5.3.1 Charge/Discharge with Constant Current

Constant current chargers vary the voltage they apply to the battery to maintain a constant current flow, switching off when the voltage reaches the level of a full charge. [11] Fig. 5.5 shows experimental data of discharge property with constant current.

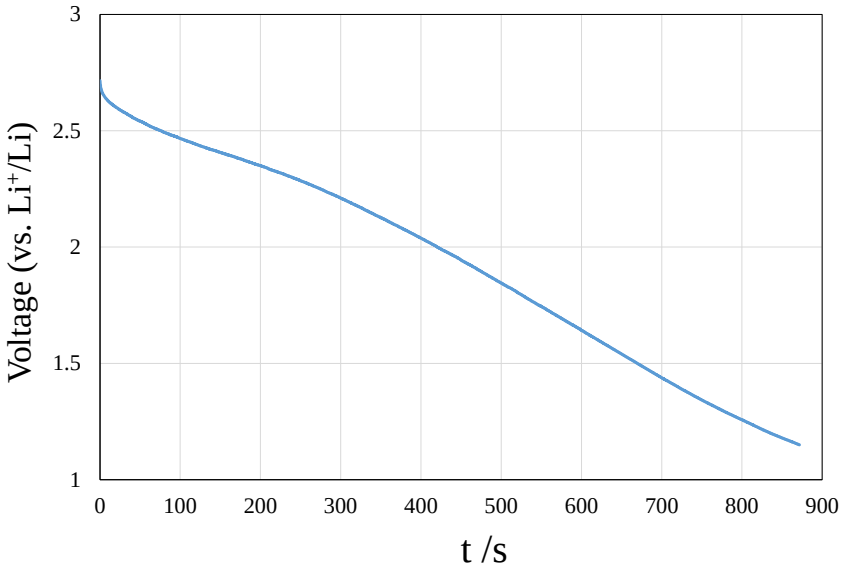

Fig. 5.5 Discharge property with constant current.

5.3.2 Frequency Response Analyzer (FRA)

Electrochemical impedance spectroscopy measurements can be performed with FRA. In a typical electrochemical impedance measurement, FRA generates a sine wave with a user-defined frequency and a small amplitude. This signal is superimposed on the applied DC potential or current on the cell. The schematic diagram of impedance measurement system used in this experiment is shown in Fig. 5.6 (a).

The impedance of the single-electrode cells can be interpreted in terms of the simple circuit shown in Fig. 5.6 (b), in which a resistance (R)-capacitance (C) network is connected in series with an electrolyte resistance R_{sol}, where R represents the electrode-reaction resistance and C represents the capacitance of the battery cell. As shown in Fig. 5.6 (c), the diameter of the semicircle in the Cole-Cole plot represents the electrode-reaction resistance R.

(a)

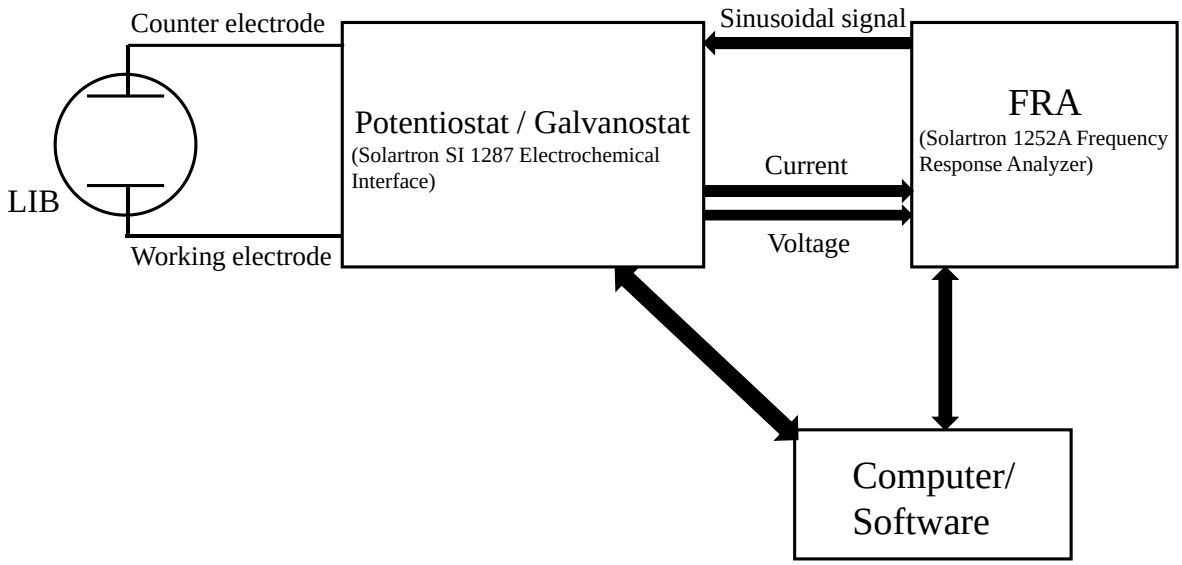
Counter electrode
LIB
Working electrode
Potentiostat / Galvanostat
(Solartron SI 1287 Electrochemical Interface)
Sinusoidal signal
Current
Voltage
FRA
(Solartron 1252A Frequency Response Analyzer)
Computer/
Software

(b)

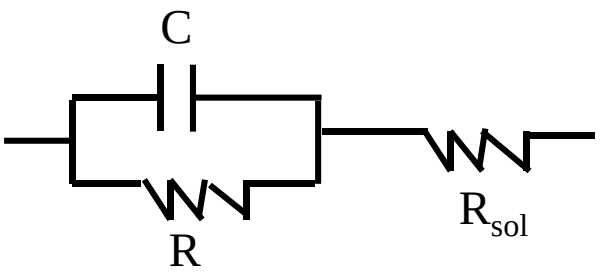
C
R
R_{sol}

(c)

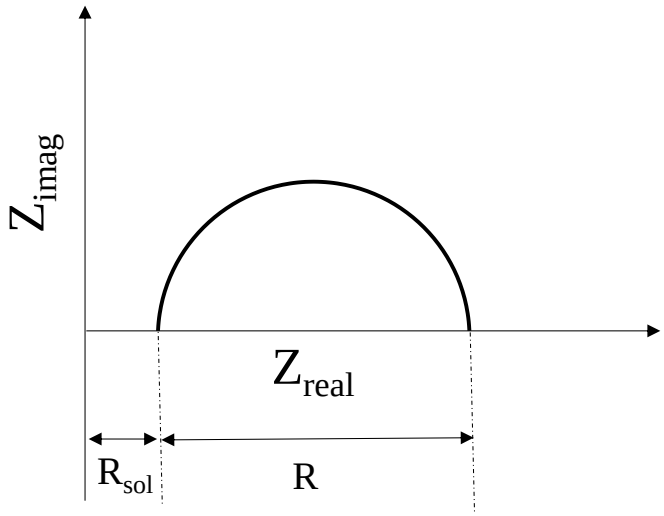

Fig. 5.6 (a) The schematic diagram of impedance measurement system used in this experiment, (b) Simple equivalent circuit of the LIBs in this experiment, (c) Cole–Cole plot of the complex impedance.

5.3.3 Cyclic Voltammetry

Cyclic voltammetry is a type of electrochemical measurement. In a cyclic voltammetry experiment, the working electrode potential is ramped linearly versus time. After the set potential is reached in a cyclic voltammetry experiment, the working electrode's potential is ramped in the opposite direction to return to the initial potential. These cycles of ramps in potential may be repeated as many times as desired. Fig. 5.7 (a) shows the waveform used for the potential scanning. Before measurement, a blank test of Ti film is needed for investigating the reaction between Ti and electrolyte as shown in Fig. 5.7 (b). The sample with no-annealed WO_3 electrode was chosen for comparison. It was clearly observed that Ti film has little reaction with electrolyte. Fig. 5.7 (c) shows the experimental data of the sample used in this work with different rate of potential scanning. [12]

(a)

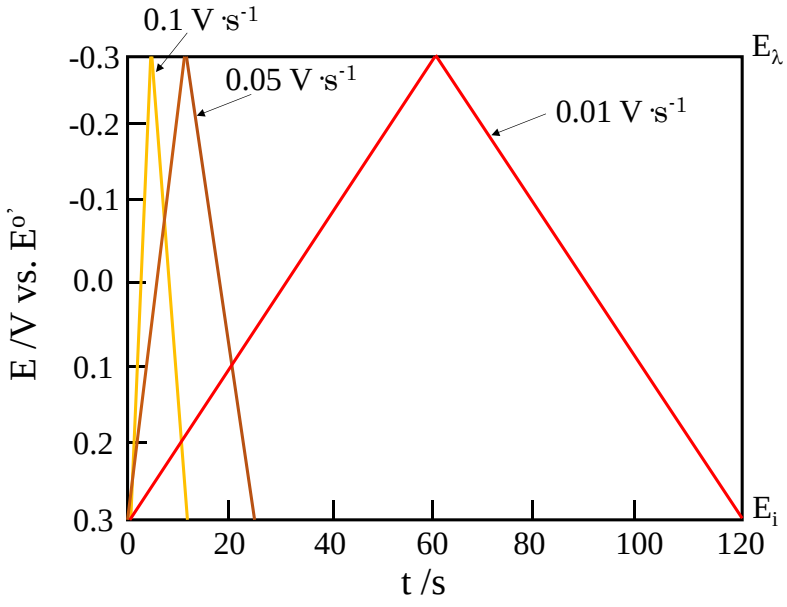
0.1 V ·s-1
0.05 V ·s-1
0.01 V ·s-1
Eλ
Ei
E /V vs. Eo'
t /s
-0.3
-0.2
-0.1
0.0
0.1
0.2
0.3
0
20
40
60
80
100
120

(b)

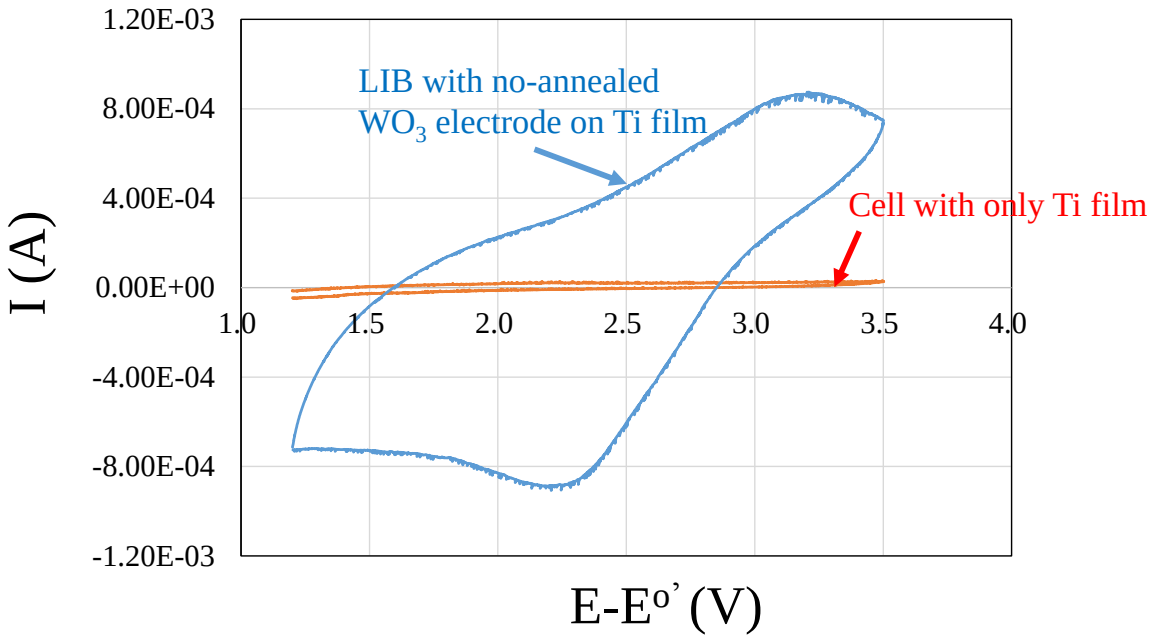
LIB with no-annealed
WO3 electrode on Ti film
Cell with only Ti film
I (A)
E-Eo' (V)
1.20E-03
8.00E-04
4.00E-04
0.00E+00
-4.00E-04
-8.00E-04
-1.20E-03
1.0
1.5
2.0
2.5
3.0
3.5
4.0

(c)

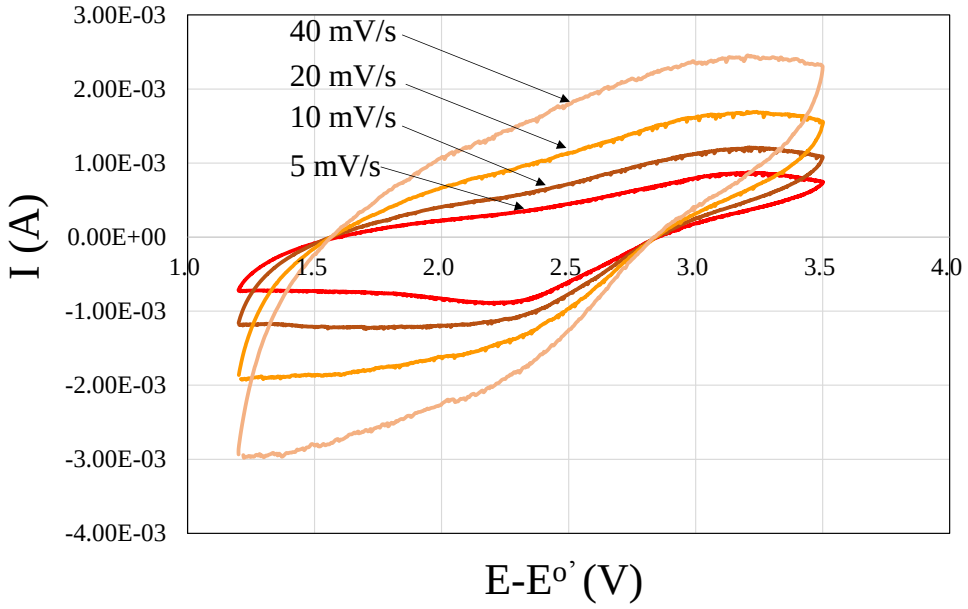

Fig. 5.7 (a) the waveform used for the potential scanning, (b) CV blank test of Ti film for investigating the reaction between Ti and electrolyte, and (c) the experimental data of the sample used in this work with different rate of potential scanning.

5.3.4 Charge Rate

Charge rate is often denoted as C or C-rate and signifies a charge or discharge rate equal to the capacity of a battery in one hour. For a 1.6Ah battery, C = 1.6A. A charge rate of C/2 = 0.8A would need two hours, and a charge rate of 2C = 3.2A would need 30 minutes to fully charge the battery from an empty state. [13]

5.4 Charge/Discharge Performance

The charge/discharge performance was measured at room temperature at a rate of 0.1 C. Fig. 5.8 (a), (b), and (c) respectively show the charge/discharge curves of the LIBs with the electrodes not subjected to annealing, annealed in N_2 at 300 ^oC, and annealed in N_2 at 700 ^oC. It was observed that the capacity difference between the charge and

discharge processes was ~3.122 mAh/g (3.88%) for the sample not subjected to annealing, ~1.170 mAh/g (1.49%) for the 300 ºC-annealed sample, and ~0.924 mAh/g (1.22%) for the 700 ºC-annealed sample. The capacity percentages given above were obtained as the capacity difference between the charge and discharge processes divided by the capacity of the discharge process at 1.5 V. The results indicate that the capacity difference between the charge and discharge processes decreased as the annealing temperature increased, implying reduced electrode degradation. Here, electrode degradation means the capacity loss between the charge and discharge processes. This improvement may be caused by the increased conduction of electrons in the N_2-annealed WO_3 electrodes. Furthermore, the discharge curve of the 700 ºC-annealed sample had a different shape from the other curves in the voltage range of 2.9–2.6 V, which indicates a change in the crystalline structure [14].

(a)

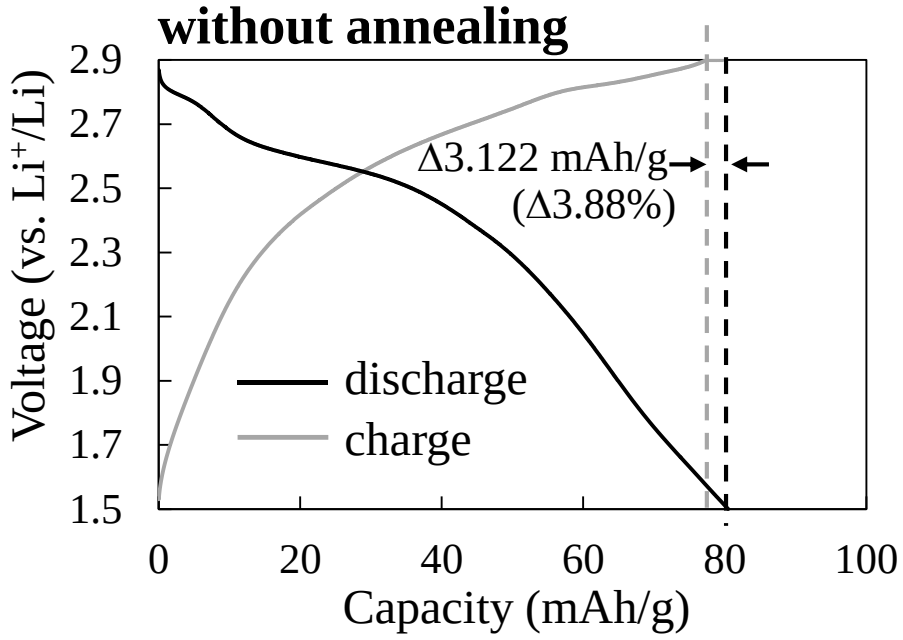

(b)

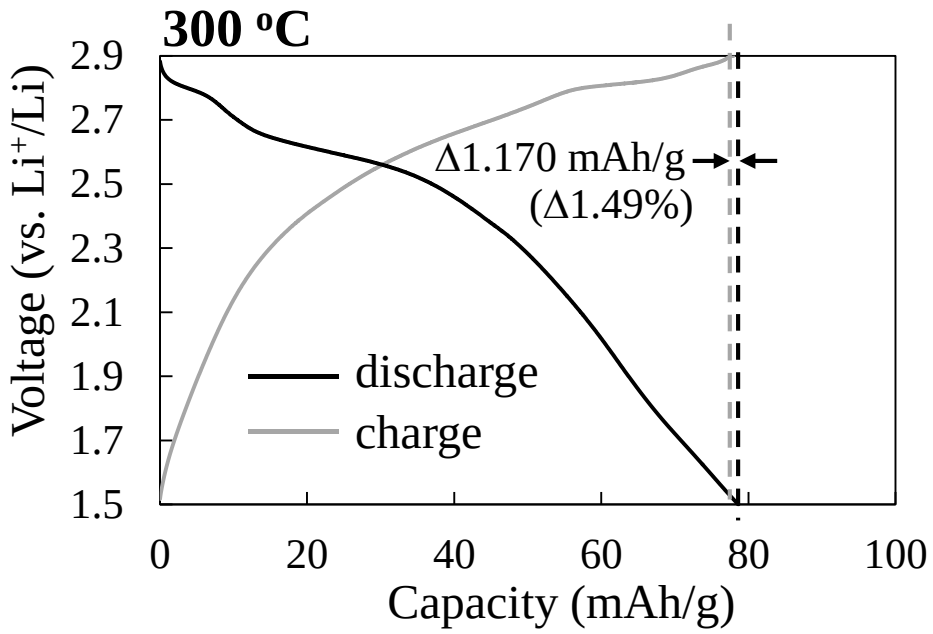

(c)

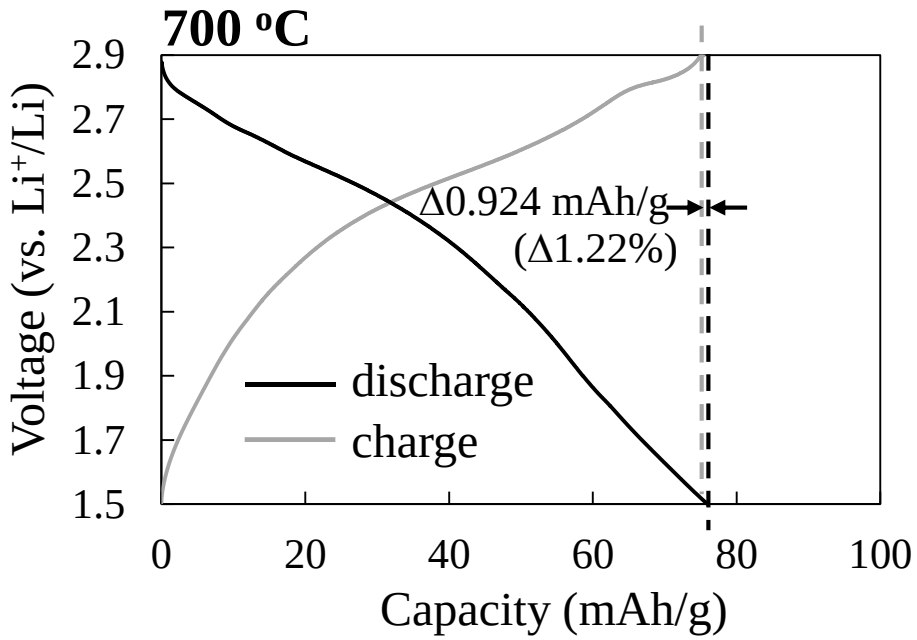

Fig. 5.8 Charge/discharge curves of the LIBs with the electrodes not subjected to annealing (a), annealed in N_2 at 300 ºC annealing (b), and annealed in N_2 at 700 ºC (c).

Cyclic voltammetry was carried out between 1.2 and 3.5 V at a sweep rate of 5 mV/sec for three cycles. The third cyclic voltammetry curves were recorded and are shown in Fig. 5.9. There is one oxidation peak and one reduction peak in the cyclic voltammetry curves for the three types of samples. The oxidation peaks are located at approximately 3.19, 3.03, and 2.82 V for the non-annealed, 300 ^{o}C-annealed, and 700 ^{o}C-annealed samples, respectively. The oxidation peak potential decreased as the annealing temperature increased, which may indicate that higher-temperature annealing generates more oxygen vacancies and promotes the oxidation reaction. Moreover, the reduction peaks are located at approximately 2.28, 2.40, and 2.37 V, respectively. The potential difference between the anodic peak and cathodic peak decreased as the annealing temperature increased (~0.91, ~0.63, and ~0.45 V, respectively), revealing the improved reversibility of the electrode reaction. The voltammetric cathodic charges (the top parts of the cyclic voltammetry curves) and anodic charges (the bottom parts of the cyclic voltammetry curves) were calculated by integrating the area of the respective regions as shown in Fig. 5.9 (b)~(d). The cathodic-to-anodic charge ratio was ~0.22 for the sample not subjected to annealing, ~0.51 for the 300 ^{o}C-annealed sample, and ~0.79 for the 700 ^{o}C-annealed sample. The ratio increased as the annealing temperature increased, demonstrating improved reversibility.

(a)

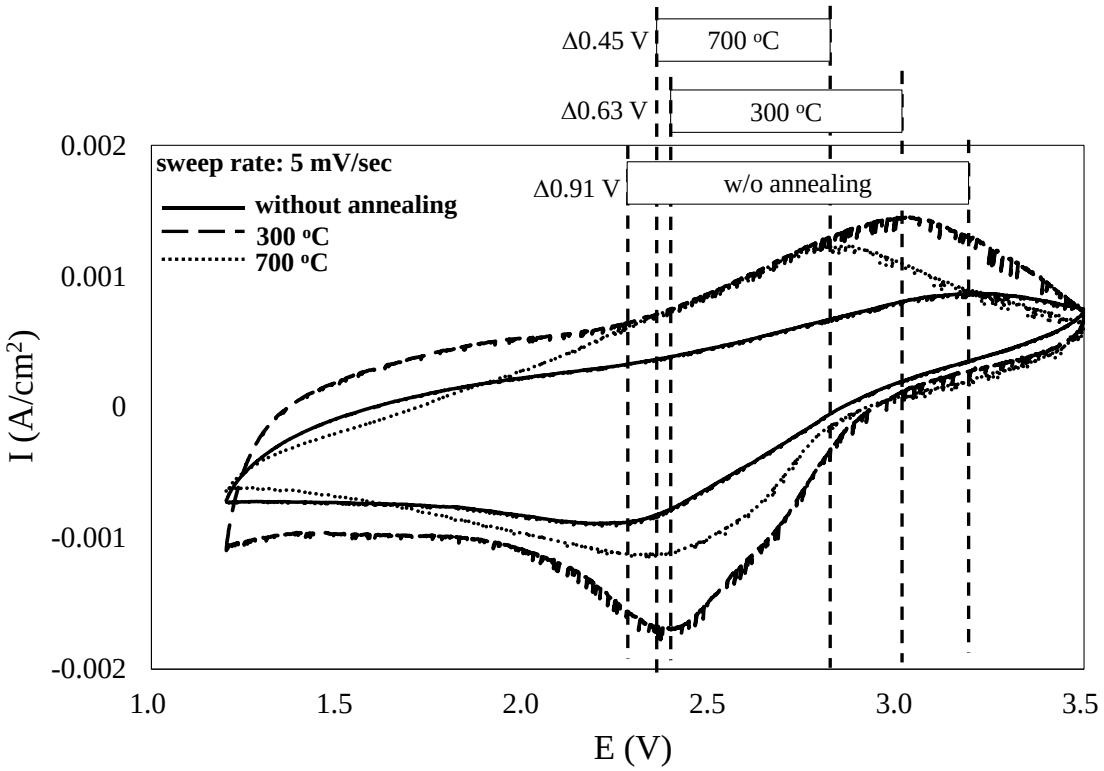
Δ0.45 V
700 °C
Δ0.63 V
300 °C
Δ0.91 V
w/o annealing
sweep rate: 5 mV/sec
without annealing
300 °C
700 °C
0.002
0.001
0
-0.001
-0.002
I (A/cm²)
1.0
1.5
2.0
2.5
3.0
3.5
E (V)

(b)

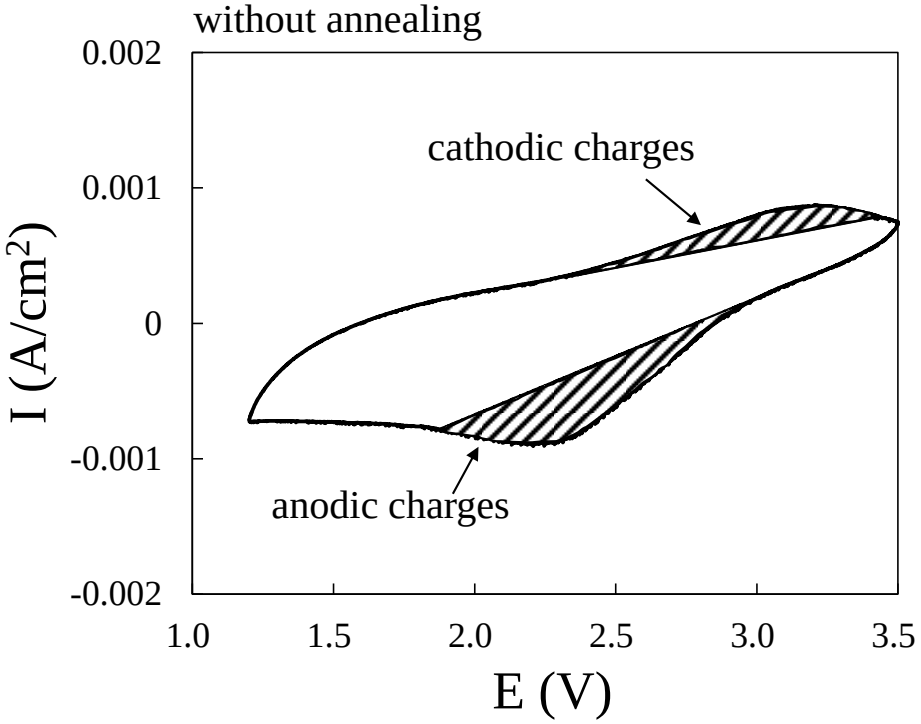
without annealing
cathodic charges
anodic charges
0.002
0.001
0
-0.001
-0.002
I (A/cm²)
1.0
1.5
2.0
2.5
3.0
3.5
E (V)

(c)

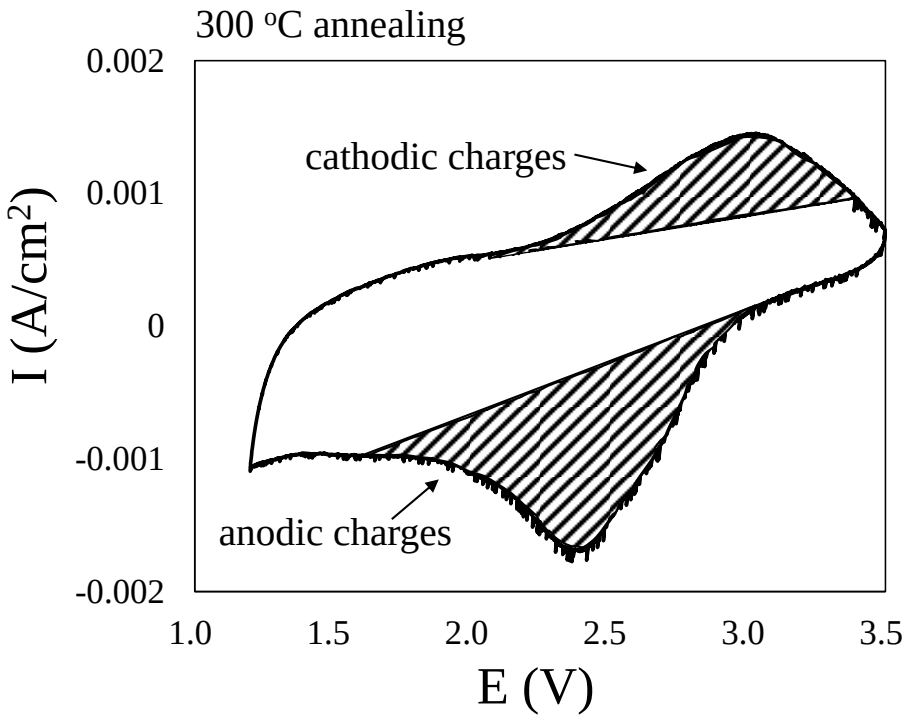
300 °C annealing
0.002
0.001
0
-0.001
-0.002
I (A/cm2)
cathodic charges
anodic charges
1.0
1.5
2.0
2.5
3.0
3.5
E (V)

(d)

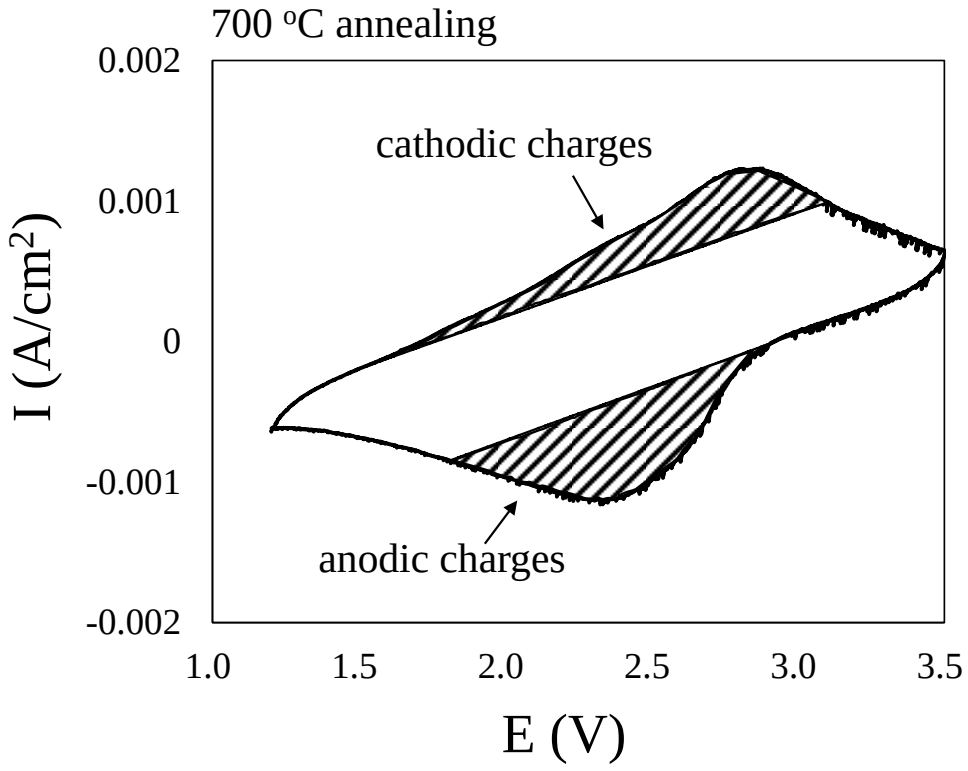
700 °C annealing
0.002
0.001
0
-0.001
-0.002
I (A/cm2)
cathodic charges
anodic charges
1.0
1.5
2.0
2.5
3.0
3.5
E (V)

Fig. 5.9. Cyclic voltammetry curves of the LIBs with the electrodes not subjected to annealing, annealed in N_2 at 300 ^oC, and annealed in N_2 at 700 ^oC (a), calculation area of cathodic charges (the top parts of the cyclic voltammetry curves) and anodic charges (the bottom parts of the cyclic voltammetry curves) of electrodes not subjected to annealing (b), annealed in N_2 at 300 ^oC annealing (c), and annealed in N_2 at 700 ^oC (d).

AC impedance spectra were measured for the three types of LIBs in their discharge state with a voltage of 2.0 V at room temperature. The amplitude of the applied ac voltage signal was 10 mV and the frequency range was from 10^5 to 10^{-2} Hz. The reaction process of the WO_3 electrodes followed Eq. (2.1). Cole–Cole plots of the complex impedance obtained using the experimental data are shown in Fig. 5.10. It is clearly shown that the electrode-reaction resistance decreased as the annealing temperature of the electrodes increased. A lower R value indicates faster charge/discharge of the WO_3 electrodes. Thus, compared with the sample with the electrode not subjected to annealing, the samples with the annealed electrodes exhibited a faster charge/discharge process. Moreover, annealing at 700 ^oC had a greater effect than annealing at 300 ^oC. The enhanced charge/discharge property is partly because the N_2-annealed WO_3 electrodes had lower resistivities, which results in high conductivity of the electrons in the electrodes and simultaneously enables faster intercalation of the Li ions into the WO_3 electrodes.

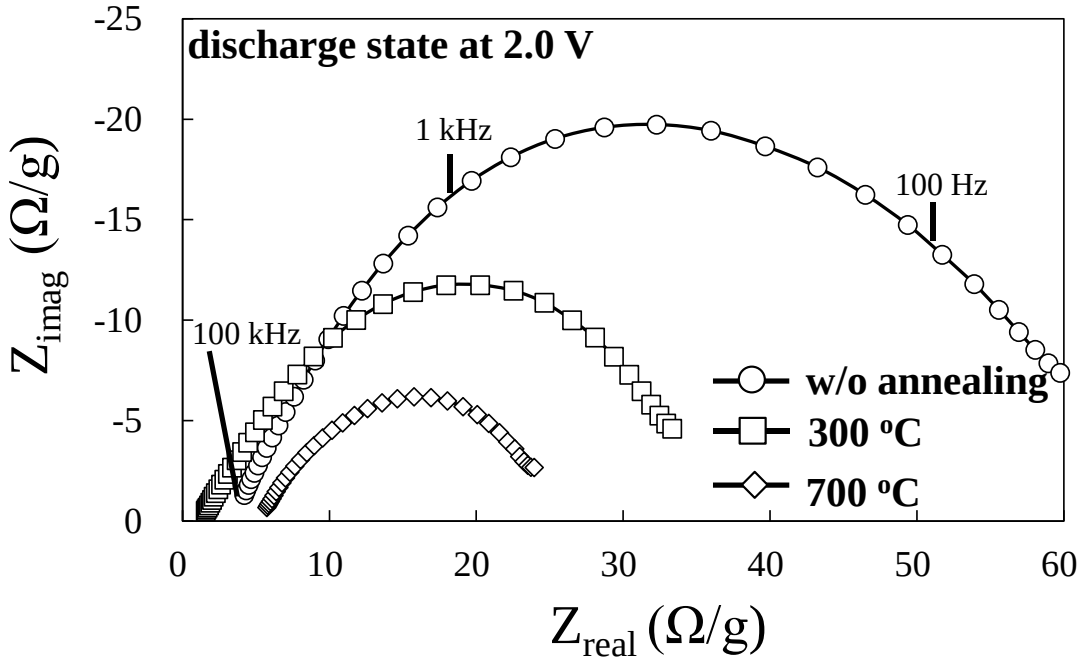

Fig. 5.10 Experimentally obtained Cole–Cole plots of the LIBs with the electrodes not subjected to annealing, annealed in N_2 at 300 °C, and annealed in N_2 at 700 °C for an AC voltage of 10 mV in the frequency range from 10^5 to 10^{-2} Hz.

To verify the increase in the charge/discharge speed discussed above, the charge capacities were measured at charge rates of 0.2, 1, and 5 C as shown in Fig. 5.11. The charge capacities were normalized by those obtained at 0.2 C. As the charge rate increased, the capacity of the sample with the electrode not subjected to annealing decreased by the largest amount, the sample with the 300 °C-annealed electrode showed better capacity retention, and the sample with the 700 °C-annealed electrode showed the best performance.

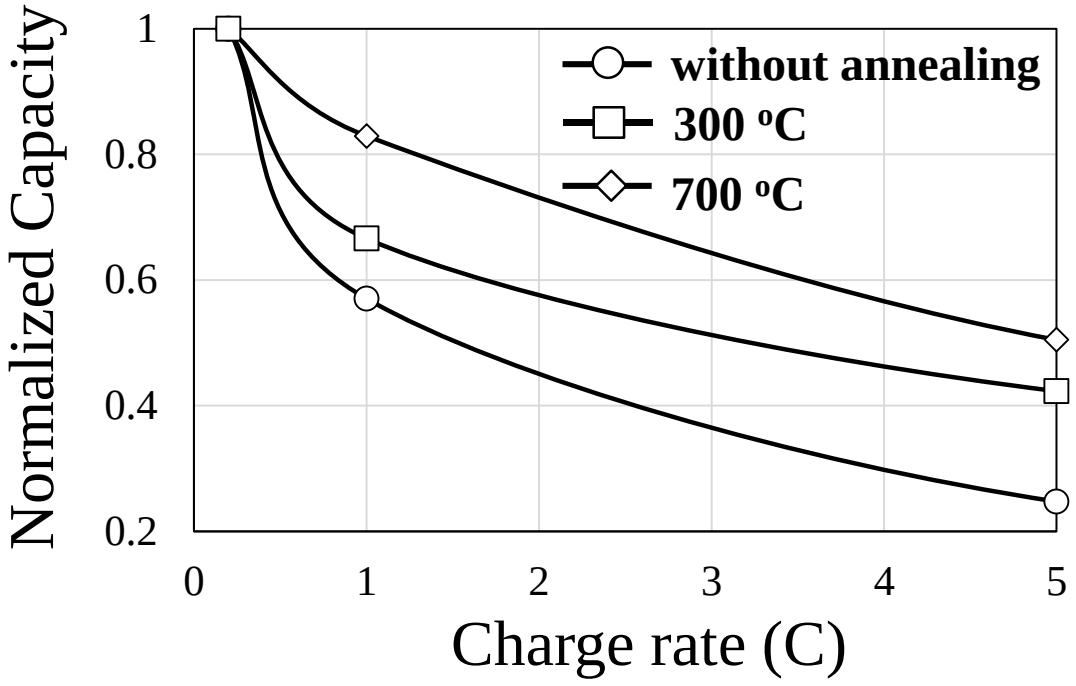

Fig. 5.11. Normalized capacities for different charge rates of the LIBs with the electrodes not subjected to annealing, annealed in N_2 at 300 ^oC, and annealed in N_2 at 700 ^oC.

5.5 Investigation of Crystalline Structures Depending on Different Annealing Conditions

The change in the crystalline structure after high-temperature annealing may also be a reason for the improved charge/discharge performance. Thus, TEM observation, the XRD patterns and Raman spectra of the electrodes were obtained to investigate the crystalline structure.

Fig. 5.12 (a) and (b) show the TEM images of WO_3 with N_2 annealing treatment at 300 ^oC and at 700 ^oC. It indicates that compared with 300 ^oC-annealed sample, 700 ^oC-

annealed sample has a larger particle size. Besides, both of the samples show the necking property.

(a)

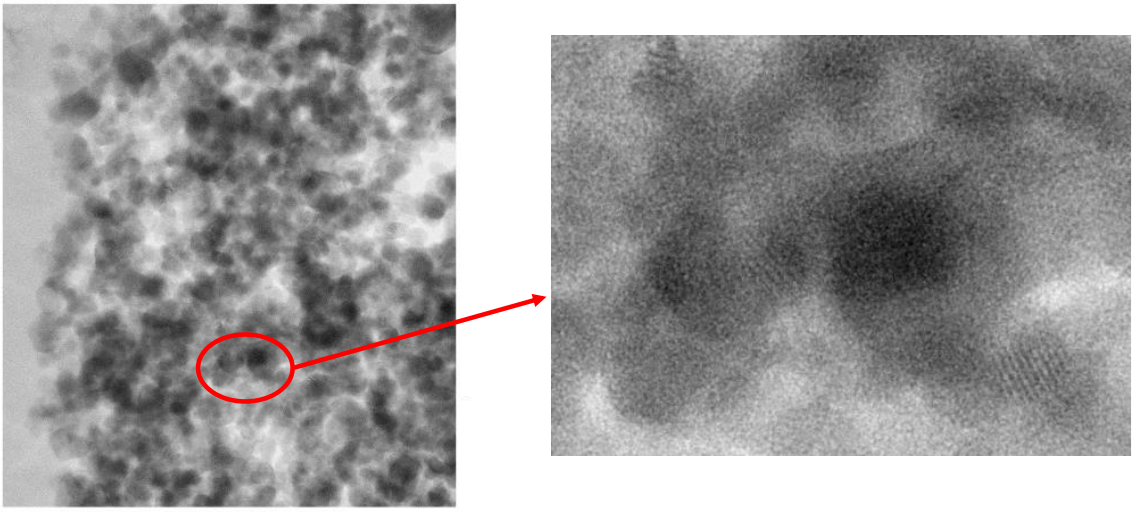

(b)

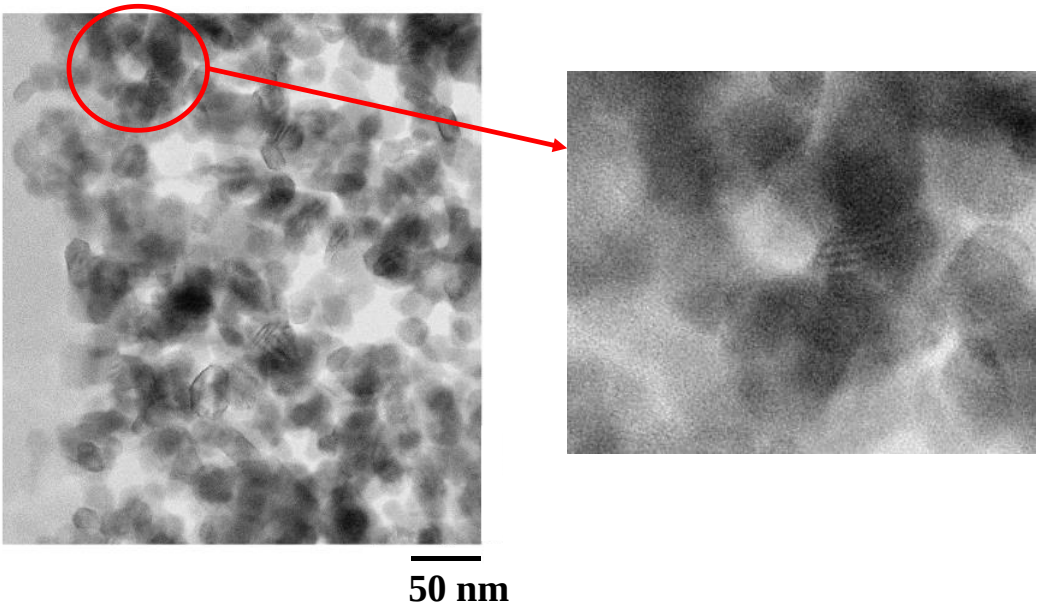

Fig. 5.12 TEM images of WO_3 with N_2 annealing treatment at 300 ^oC (a) and at 700 ^oC (b).

In this work, automatic X-ray diffraction equipment (RINT2100) developed by Rigaku Corporation was used for XRD measuremnt. Maximum rated output is 2 kW, and rated current is 2~50 mA. The measurement condition is shown in Table 5.1. Fig. 5.13 (a), (b), and (c) show the XRD patterns of the three types of electrodes. The electrode after annealing at 300 ^oC had almost the same XRD pattern as that of the electrode not subjected to annealing, both of them exhibiting a monoclinic structure. The XRD pattern of the electrode after annealing at 700 ^oC exhibited a cubiclike structure.

Table 5.1. The measurement condition of XRD patterns.

x-ray source	CuKα
Tube voltage	40 kV
Tube current	40 mA
Divergence slit	1^o
Receiving slit	0.3^o
Measurement angle	$10\sim50^o$
Scan speed	2^o/min
Sampling width	0.02^o

(a)

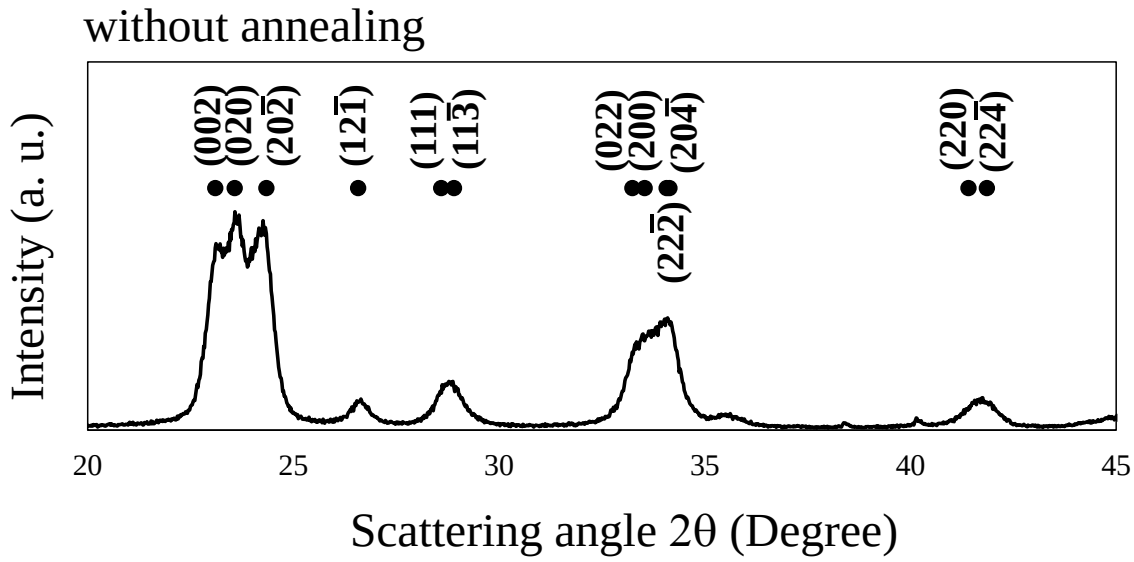
without annealing
Intensity (a. u.)
(002)
(020)
(20$\bar{2}$)
(12$\bar{1}$)
(111)
(11$\bar{3}$)
(022)
(200)
(20$\bar{4}$)
(2$\bar{2}$2)
(220)
(22$\bar{4}$)
20
25
30
35
40
45
Scattering angle 2θ (Degree)

(b)

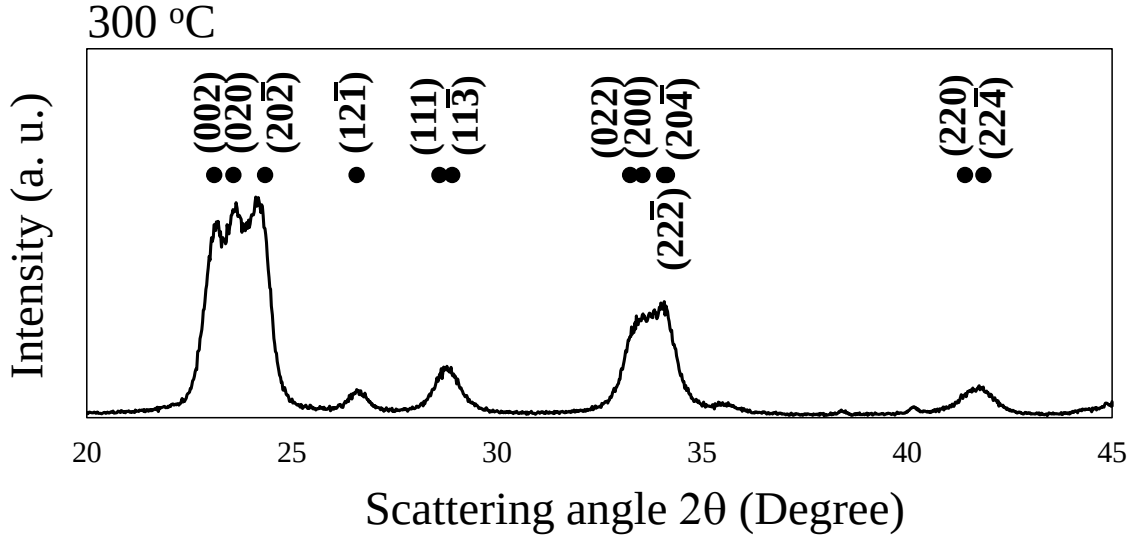
300 °C
Intensity (a. u.)
(002)
(020)
(20$\bar{2}$)
(12$\bar{1}$)
(111)
(11$\bar{3}$)
(022)
(200)
(20$\bar{4}$)
(2$\bar{2}$2)
(220)
(22$\bar{4}$)
20
25
30
35
40
45
Scattering angle 2θ (Degree)

(c)

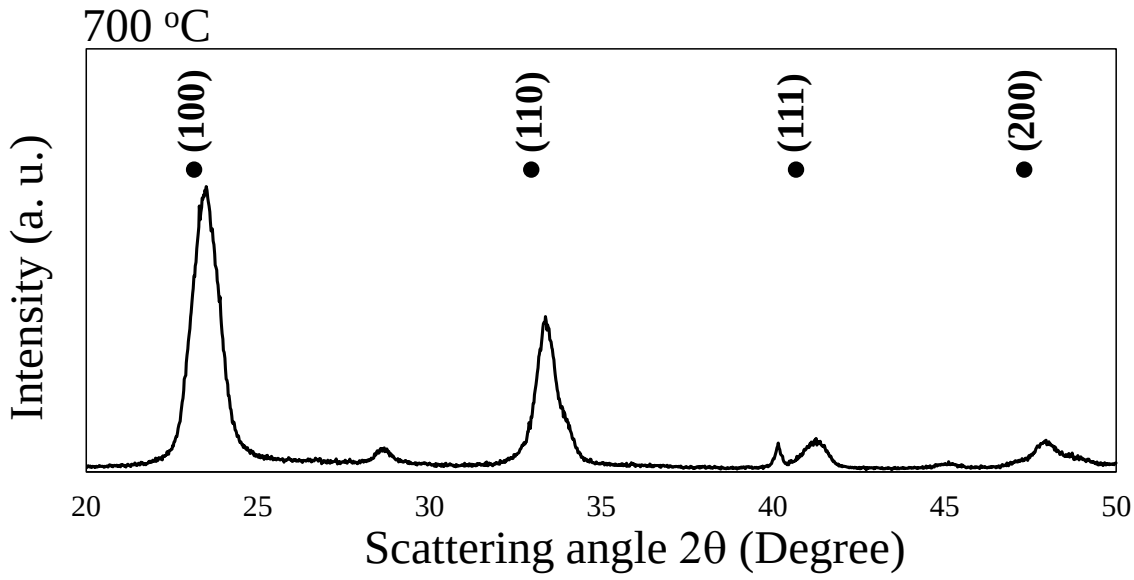

Fig. 5.13. XRD patterns of electrodes not subjected to annealing (a), annealed in N_2 at 300 °C (b), and annealed in N_2 at 700 °C (c).

Furthermore, the Raman spectra also suggested a change in the crystalline structure after annealing at 700 °C treatment as shown in Fig. 5.14. In this work, Renishaw InVia-Raman equipment was used for Raman measurement. The measurement condition is shown in Table 5.2. In Fig. 5.14 (a), the spectrum of the 300 °C-annealed sample has two main peaks at ~808 and ~710 cm^{-1}, quite similar to the spectrum reported for m-WO_3 [15]. They are both assigned to the υ ($O–W^{6+}–O$) vibrational stretching mode of the W–O–W bridging oxygen [16]. The peak at ~710 cm^{-1} is considered to be sensitive to changes in the crystal symmetry and distortion [17]. Moreover, a very weak peak located at ~324 cm^{-1} can be seen in the spectrum. This peak corresponds to the vibrations of the $O–W^{5+}–O$ and indicates the presence of an oxygen-deficient phase [18]. The peak at ~270 cm^{-1} can be assigned to the δ ($O–W^{6+}–O$) bending mode [19]. Fig. 5.14 (b) shows the

Raman spectrum of the 700 ºC-annealed sample. The υ (O–W^{6+}–O) vibrational stretching mode at ~710 cm^{-1} and the δ (O–W^{6+}–O) bending mode at ~270 cm^{-1} in Fig. 14 (a) were respectively shifted to ~697 and ~256 cm^{-1}, indicating a change in the crystalline structure. The peak at ~697 cm^{-1} became broader, which may also be caused by a change in the crystal symmetry and lattice distortion [17]. Moreover, the peak located at ~324 cm^{-1} representing an oxygen-deficient phase was also observed. The intensity of this peak was higher than that in Fig. 5.14 (a), which may indicate that more oxygen vacancies were generated. Therefore, from the analysis of the XRD patterns and Raman spectra, it is suggested that annealing at 300 ºC in N_2 ambient did not change the crystalline structure of m-WO_3; however, annealing at 700 ºC treatment changed the structure from monoclinic to a cubiclike structure in which the W-O bond length is equal in all three directions. Since it was reported that Li ions intercalate into cubic WO_3 more easily than into m-WO_3 [20], the change in the crystalline structure may explain the best performance of the 700 ºC-annealed electrode.

Table 5.2. The measurement condition of Raman spectra.

Excitation wavelength	514.5 nm (Ar ion laser)
Output	5 mW
Objective lens	20 times
Measurement wavelength	50 cm^{-1}~980 cm^{-1} (static measurement; diffraction lattice fixation)
Exposure time	10 sec/time; integration of 10 times (static measurement)
Diffraction lattice ruling number	1800 lines/mm

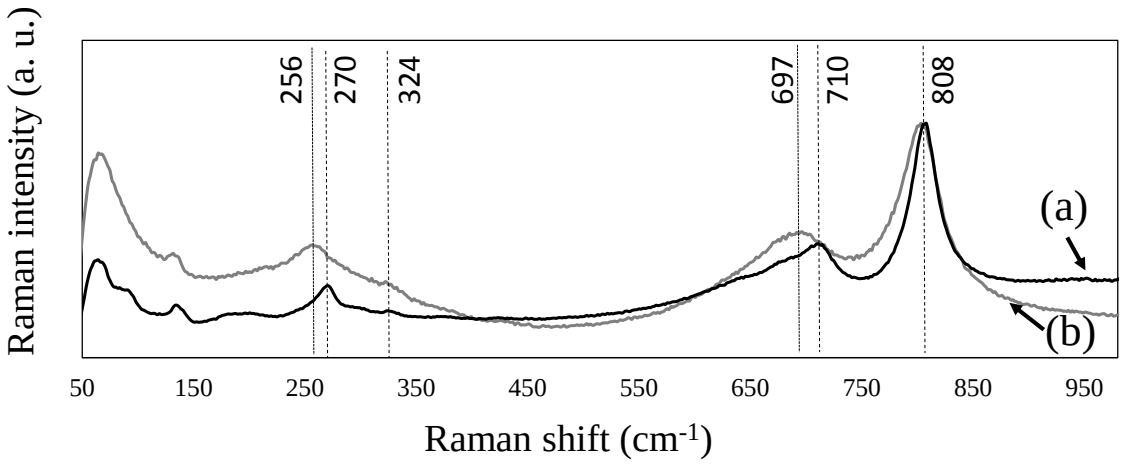

Fig. 5.14. Raman spectra of electrodes annealed at 300 ºC (a) and 700 ºC (b) in N_2 ambient.

Fig. 5.15 (a), (b) and (c) show the charge and discharge curves. On charge curves (black lines), no-annealed sample and 300 ºC-annealed sample have a plateaus which is circled by a gray circle. However, 700 ºC-annealed sample has no plateau. This phenomenon also indicates a crystalline change after 700 ºC-annealed sample.

(a)

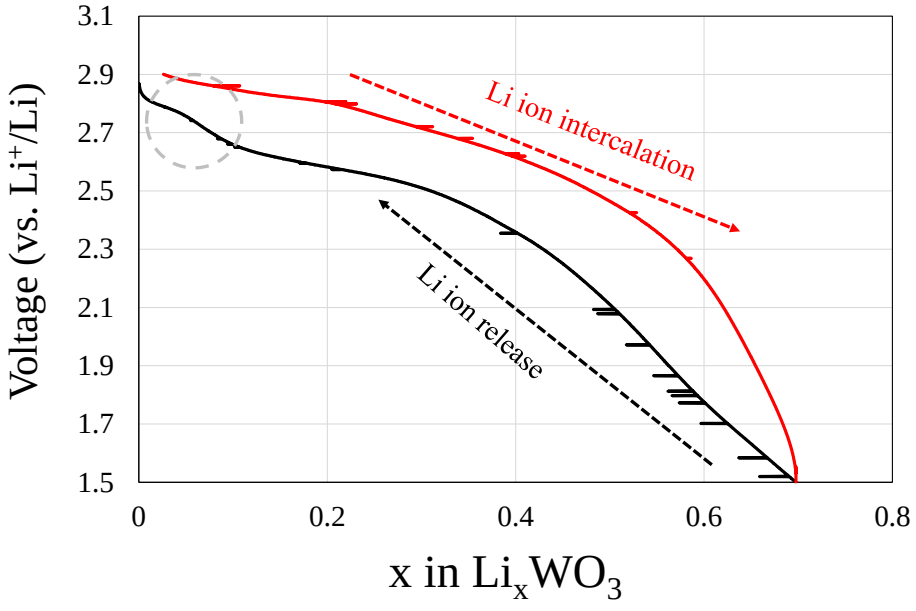

(b)

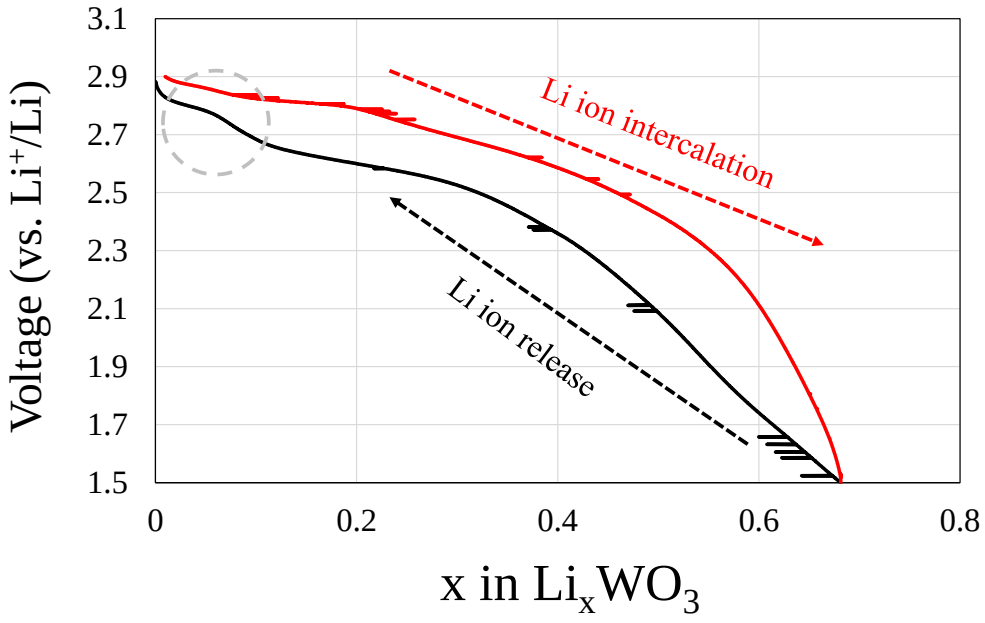
3.1
2.9
2.7
2.5
2.3
2.1
1.9
1.7
1.5
Voltage (vs. Li+/Li)
0
0.2
0.4
0.6
0.8
x in LixWO3
Li ion intercalation
Li ion release

(c)

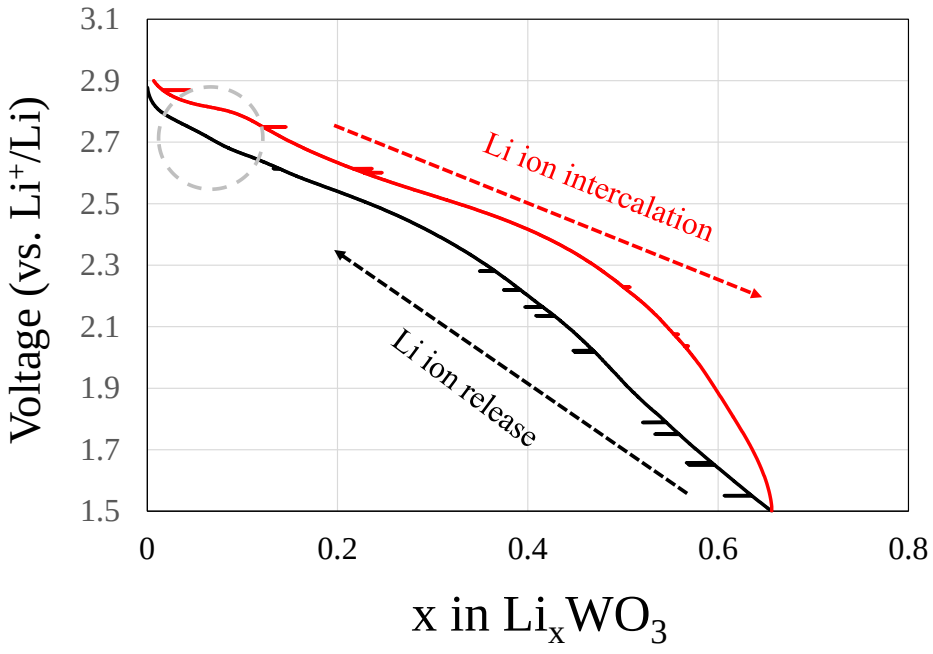
3.1
2.9
2.7
2.5
2.3
2.1
1.9
1.7
1.5
Voltage (vs. Li+/Li)
0
0.2
0.4
0.6
0.8
x in LixWO3
Li ion intercalation
Li ion release

Fig. 5.15. Voltage vs x for samples with no-annealed WO_3 electrode (a), 300 ^oC-annealed (b), and 700 ^oC-annealed (c). The red curve is for the discharge of the cell and the black curve is for the charge of the cell.

5.6 Conclusion

Since the electron conductivity can be improved by annealing in N_2 owing to the generation of oxygen vacancies in crystalline WO_3, the performance of LIBs with N_2-annealed WO_3 electrodes was investigated by consideration of the charge-discharge properties, cyclic voltammetry curves, frequency response, and the charge capacity at different charge rates. It was observed that the charge/discharge speed and reversibility were improved as the N_2 annealing temperature increased. Furthermore, the XRD patterns and Raman spectra revealed that annealing at 300 ^oC in N_2 ambient did not change the monoclinic crystalline structure, whereas annealing at 700 ^oC in N_2 ambient changed the monoclinic structure into a cubiclike structure. These results clearly demonstrated that increasing the electron conductivity of WO_3 electrodes can markedly improve the charge/discharge speed and reversibility. Moreover, oxygen vacancies may cause the crystalline structure to change into the cubiclike structure, which may promote Li ion intercalation. The reason may be that electrons in the 5d orbital generated by oxygen vacancies is considered to relax the lattice distortion due to the interaction between electrons and the lattice. Therefore, to enhance the charge/discharge performance of LIBs, electron conduction should be a focus of research. Additionally, crystalline WO_3 was demonstrated to be a promising material for electrodes since oxygen vacancy generation can be induced by a simple annealing treatment, improving the electron conduction and Li ion transportation.

Reference List

[1] B. Scrosati, ``Battery technology-challenge of portable power,'' *Nature,* vol. 373, pp. 557-558, 1995.

[2] A. R. Armstrong and P. G. Bruce, ``Synthesis of layered $LiMnO_2$ as an electrode for rechargeable lithium batteries,'' *Nature,* vol. 381, pp. 499-500, 1996.

[3] N. Li, C. R. Martin, and B. Scrosati, ``Nanomaterial-based Li-ion battery electrodes,'' *J. Power Sources,* vol. 97, pp. 240-243, 2001.

[4] V. Etacheri, R. Marom, R. Elazari, G. Salitra, and D. Aurbach, ``Challenges in the development of advanced Li-ion batteries: a review,'' *Energy Environ. Sci.*, vol. 4, pp: 3243-3262, 2011.

[5] H. Zhao, Y. Li, Z. Zhu, J. Lin, Z. Tian, and R. Wang, ``Structural and electrochemical characteristics of $Li_{4-x}Al_xTi_5O_{12}$ as anode material for lithium-ion batteries,'' *Electrochim. Acta,* vol. 53, pp. 7079-7083, 2008.

[6] Y. Q. Wang, L. Gu, Y. G. Guo, H. Li, X. Q. He, S. Tsukimoto, Y. Ikuhara, and L. J. Wan, ``Rutile-TiO_2 nanocoating for a high-rate $Li_4Ti_5O_{12}$ anode of a lithium-ion battery,'' *J. Am. Chem. Soc.*, vol. 134, pp. 7874-7879, 2012.

[7] X. Y. Fan, Y. Li, J. J. Wang, L. Gou, P. Zhao, D. L. Li, L. Huang, and S. G. Sun, ``Synthesis and electrochemical performance of porous Li_2FeSiO_4/C cathode material for long-life lithium-ion batteries,'' *J. Alloys Compd.*, vol. 493, pp. 77-80, 2010.

[8] S. H. Lee, H. M. Cheong, C. E. Tracy, A. Mascarenhas, R. Pitts, G. Jorgensen, S. K. Deb, ``Influence of microstructure on the chemical diffusion of lithium ions in amorphous lithiated tungsten oxide films,'' *Electrochim. Acta,* vol. 46, pp. 3415-3419, 2001.

[9] http://www.nisshinkasei.co.jp/english/development/ec_vehicle/index_f.html

[10] G. Hollinger, T. M. Duc and A. Deneuville, ``Charge Transfer in Amorphous Colored

W O 3 Films Observed by X-Ray Photoelectron Spectroscopy," *Phys. Rev. Lett.*, vol. 37, pp. 1564-1567, 1976.

[11] http://www.epectec.com/batteries/charging/

[12] http://en.wikipedia.org/wiki/Cyclic_voltammetry

[13] http://en.wikipedia.org/wiki/Battery_charger

[14] Q. Zhong, J. R. Dahn, K. Colbow, ``Lithium intercalation into WO_3 and the phase diagram of Li_xWO_3," *Phys. Rev. B*, vol. 46, pp. 2554-2560, 1992.

[15] T. Pauporté, M. C. Bernard, Y. Soldo-Olivier and R. Faure, ``Structural Changes in Electrochromic WO_3 Thin Films Induced by the First Electrochemical Cycles," *J. Electrochem. Soc.*, vol. 151, pp. H21-26, 2004.

[16] M. F. Daniel, B. Desbat and J. C. Lassegues, ``Infrared and Raman spectroscopies of rf sputtered tungsten oxide films," *J. Solid State Chem.*, vol. 73, pp. 127-139, 1988.

[17] D. C. Koningsberger, R. Prins, *X-ray Absorption: Principles, Applications, Techniques of EXAFS, SEXAFS, and XANES.* New York: Wiley, 1988.

[18] N. E. Stankova, P. A. Atanasov, T. J. Stanimirova, A. O. Dikovska, R. W. Eason, ``Thin (001) tungsten trioxide films grown by laser deposition," *Appl. Surf. Sci.*, vol. 247, pp. 401-405, 2005.

[19] E. Valova, J. Georgieva, S. Armyanov, S. Sotiropoulos, A. Hubin, K. Baert, M. Raes, ``Morphology, Structure and Photoelectrocatalytic Activity of TiO_2/WO_3 Coatings Obtained by Pulsed Electrodeposition onto Stainless Steel," *J. Electrochem. Soc.*, vol. 157, pp. D309-315, 2010.

[20] H. Yamada, M. Hibino and T. Kudo, ``Li-intercalated ReO_3-type solid solutions in the Nb_2O_5–WO_3 system," *Mater. Res. Bull.*, vol. 34, pp. 955-962, 1999.

Chapter 6 Summary and Conclusions

In this work, we increased the charge/discharge performance of LIBs from the viewpoint of electron conduction in the electrodes. m-WO_3 was chosen for the electrodes in this study. To improve the charge/discharge speeds, the electron transport mechanism of *m*-WO_3 thin films was studied by fitting the resistivity obtained after N_2 annealing at different temperatures by assuming two types of electron conduction mechanism: band conduction and NNH conduction. It was proposed for the first time that two conduction mechanisms simultaneously exist in the electron conduction of *m*-WO_3 thin films.

In chapter 2, the semiconductor properties of WO_3 were illustrated, including bandgap modification due to ion intercalation and its behavior as an n-type semiconductor due to oxygen vacancies. Some typical crystalline structures of WO_3 were introduced, i.e., cubic, tetragonal I, and hexagonal structures. Moreover, the electrochromic characteristic was discussed in a separate subsection, owing to its various applications, such as smart windows, gas sensors, a photocatalyst, the electrodes of LIBs, and so forth. The principles of various applications of WO_3 were also introduced. Owing to its electrochromic characteristic, the application of WO_3 electrodes in LIBs is expected.

In chapter 3, we focused on improving the electron conductivity of m-WO_3 thin films. We successfully improved the electron conduction of WO_3 powder thin films fabricated from nanoparticles. Resistivity measurements were carried out after annealing in N_2 or 5% O_2+95% N_2 ambient. Annealing in N_2 ambient decreases the resistivity. Subsequent annealing in 5% O_2+95% N_2 ambient results in the resistivity returning to its initial value. This was explained by derivation of the activation energy, which suggests that oxygen vacancies stably exist at approximately 0.2 eV below the bottom of the conduction band. Moreover, compared with low-temperature annealing in N_2, high-temperature (from 600 to 750 ^oC) annealing in N_2 had a greater effect on decreasing the resistivity of m-WO_3

thin films.

In chapter 4, the electron transport mechanism of *m*-WO_3 thin films was studied by fitting the resistivity obtained after N_2 annealing at different temperatures by assuming two types of electron conduction mechanism: band conduction and NNH conduction. It was proposed for the first time that two conduction mechanisms simultaneously exist in the electron conduction of *m*-WO_3 thin films. Moreover, after high-temperature annealing in N_2, the NNH conduction mechanism becomes dominant owing to the increased number of oxygen vacancies.

In chapter 5, the performance of LIBs with N_2-annealed WO_3 electrodes was investigated by consideration of the charge-discharge properties, cyclic voltammetry curves, the frequency response, and the charge capacity at different charge rates. It was observed that the charge/discharge speed and reversibility were improved as the N_2 annealing temperature increased. Furthermore, XRD patterns and Raman spectra revealed that annealing at 300 ^oC in N_2 ambient did not change the monoclinic crystalline structure, whereas annealing at 700 ^oC in N_2 ambient changed the monoclinic structure into a cubiclike structure. These results clearly demonstrated that increasing the electron conductivity of WO_3 electrodes can markedly improve the charge/discharge speed and reversibility. Moreover, oxygen vacancies may cause the crystalline structure to change into the cubiclike structure, which may promote Li ion intercalation. Therefore, to enhance the charge/discharge performance of LIBs, electron conduction should be a focus of research. Additionally, crystalline WO_3 was demonstrated to be a promising material for electrodes since oxygen vacancy generation can be induced by a simple annealing treatment, improving the electron conduction and Li ion transportation.

The following are suggested as future work.

1) To improve the performance of LIBs with WO_3, it is necessary to include some conductive additives such as carbon into the WO_3 electrodes, which should be investigated.
2) Carrier density and mobility of m-WO_3 after N_2 annealing need to be evaluated. (Hall Measurement)
3) (From Prof. Natori) The surface of necked WO_3 nanoparticles can be coated with some high-resistivity materials to decrease the total resistivity.
4) Not only the monoclinic structure but also the hexagonal structure of WO_3 which has larger tunnel windows, can also be investigated for its use as electrodes of LIBs.
5) Compared with WO_3, MoO_3 which has layers of distorted MoO_6 octahedra in an orthorhombic crystal, may be easier for Li ion intercalation and should be investigated.

Publications and Presentations

Peer Reviewed International Journals

1. W. Li, A. Sasaki, H. Oozu, K. Aoki, K. Kakushima, Y. Kataoka, A. Nishiyama, N. Sugii, H. Wakabayashi, K. Tsutsui, K. Natori, and H. Iwai. "Improvement of charge/discharge performance for lithium ion batteries with tungsten trioxide electrodes", accepted by Microelectronics Reliability.

2. W. Li, A. Sasaki, H. Oozu, K. Aoki, K. Kakushima, Y. Kataoka, A. Nishiyama, N. Sugii, H. Wakabayashi, K. Tsutsui, K. Natori, and H. Iwai. "Electron Transport Mechanism of Tungsten Trioxide Powder Thin Film Studied by Investigating Effect of Annealing on Resistivity", accepted by Microelectronics Reliability.

International Conferences

1. W. Li, A. Sasaki, H. Oozu, K. Aoki, K. Kakushima, Y. Kataoka, A. Nishiyama, N. Sugii, H. Wakabayashi, K. Tsutsui, K. Natori, H. Iwai. Resistivity dependence of Monoclinic Thin Tungsten Oxide Film on Annealing Processes, WIMNACT-39, Tokyo Institute of Technology, Japan, February 7, 2014.

2. W. Li, K. Nakajima, K. Kakushima, P. Ahmet, K. Tsutsui, A. Nishiyama, N. Sugii, K. Natori, T. Hattori and H. Iwai. Extraction of Interface State Density of 3-dimensional Si channel. IEEE EDS WIMNACT-37, Tokyo Institute of Technology, Japan, February 18, 2013.

3. W. Li, K. Nakajima, C. Dou, K. Kakushima, P. Ahmet, K. Tsutsui, A. Nishiyama, N. Sugii, K. Natori, T. Hattori, and H. Iwai, "Evaluation of Interfacial State Density of MOS Capacitor with Three-Dimensional Channel by Conductance Method", CSTIC 2012, March 18-19, 2012, in Shanghai.

Domestic Conferences

1. W. Li, A. Sasaki, H. Oozu, K. Aoki, K. Kakushima, Y. Kataoka, A. Nishiyama, N. Sugii, H. Wakabayashi, K. Tsutsui, K. Natori, H. Iwai. Resistivity dependence of Monoclinic Thin Tungsten Oxide Film on Annealing Processes, The 61th JSAP

Spring Meeting, the Japan society of Applied Physics, Aoyama Gakuin University, March 17, 2014, No.17p-PG2-17.

2. T. Inamura, W. Li, K. Kakushima, Parhat Ahmet, Y. Kataoka, A. Nishiyama, N. Sugii, K. Tsutsui, K. Natori, T. Hattori, H. Iwai, “Infrared Absorption Characteristic of $FeSi_2$ Formed by Fe/Si Multi-layered Sputter Process”, The 73th JSAP Autumn Meeting, the Japan society of Applied Physics, Ehime University and Matsuyama University, September 13, 2012, No. 13p-F2-8.

Acknowledgements

First of all, I would like to express my sincere gratitude to my supervisor, Prof. Hiroshi Iwai from Tokyo Institute of Technology, for all of his dedicated guidance and attentive support on my studies and life.

I also sincerely acknowledge to my co-supervisor, Associate Prof. Kuniyuki Kakushima who gave me many great ideas for my study and taught me detailed experiment process and knowledge.

I am also deeply indebted to Prof. Yoshinori Kataoka, who patiently guided me to overcome many crucial challenges in my studies and has spent much time reading through each draft and provided me with inspiring advice. Moreover, in the preparation of the thesis, he helped me get a chance of doing experiment in Toshiba Materials Co., Ltd where I learned a lot and got to know many kind and excellent people.

Besides, I sincerely acknowledge the President of Toshiba Materials Co., Ltd, Kumpei Kobayashi, who gave me the chance of learning and doing experiment in Toshiba Materials Co., Ltd. I also owe a special debt of gratitude to Dr. Katsuaki Aoki, Mr. Hajime Takeuchi, Dr. Hideki Ohkawa, Mr. Hideyuki Oozu and Mr. Akito Sasaki from Toshiba Materials Co., Ltd, who taught and helped me a lot with experiment and gave me many valuable advice for this thesis.

Likewise, I would like to thank Prof. Kenji Natori, Prof. Kazuo Tsutsui, Prof. Hiroshi Wakabayashi, Prof. Nobuyuki Sugii, Prof. Akira Nishiyama, and Prof. Parhat Ahmet for their valuable advices during my studying life at Iwai/Kakushima Lab.

I would also like to gratefully appreciate Prof. Zhenan Tang from Dalian University of

Technology, and Prof. Hei Wong from City University of Hong Kong, for evaluating the qualification of this thesis and their valuable advices. Moreover, I deeply appreciate Prof. Zhenan Tang for recommending me to Prof. Hiroshi Iwai for studying in Tokyo Institute of Technology.

I would also like to thank Ms. Akiko Matsumoto and Ms. Masako Nishizawa from Iwai/Kakushima laboratories for their kind support and help with dealing with many documents in my four and a half years' studying life.

I would also like to express my deep gratitude to all of other research staff and student members in Iwai/Kakushima Lab for their help from many aspects.

I also truly appreciate my friends, Ziyao Sun, Wei Qiu, Li Gao, Yueming Zheng and others for their helping with my study and life.

Finally, I would like to express my deep gratitude to my parents and my other family members for their continuous help, love and firm encouragement.